Controls on the sources and distribution of chalcophile and lithophile trace elements in arc magmas

by

Rameses Joseph D'Souza
B.Sc. (Honours), University of Alberta, 2008
M.Sc., University of Alberta, 2012

A Dissertation Submitted in Partial Fulfillment
of the Requirements for the Degree of

DOCTOR OF PHILOSOPHY

in the School of Earth and Ocean Sciences

Supervisory Committee

Controls on the sources and distribution of chalcophile and lithophile trace elements in arc magmas

by

Rameses Joseph D'Souza
B.Sc. (Honours), University of Alberta, 2008
M.Sc., University of Alberta, 2012

Supervisory Committee

Dr. Dante Canil (School of Earth and Ocean Sciences)
Supervisor

Dr. Laurence Coogan (School of Earth and Ocean Sciences)
Departmental Member

Dr. Stephen Johnston (School of Earth and Ocean Sciences)
Departmental Member

Dr. Alexandre Brolo (Department of Chemistry)
Outside Member

Abstract

Supervisory Committee
Dr. Dante Canil (School of Earth and Ocean Sciences)
Supervisor
Dr. Laurence Coogan (School of Earth and Ocean Sciences)
Departmental Member
Dr. Stephen Johnston (School of Earth and Ocean Sciences)
Departmental Member
Dr. Alexandre Brolo (Department of Chemistry)
Outside Member

Volcanic arcs have been the locus of continental growth since at least the Proterozoic eon. In this dissertation, I seek to shine more light on arc processes by inferring the lower crustal mineralogy of an ancient arc by geochemical and structural modelling of its exposed levels. Arcs characteristically have high concentrations of incompatible elements, thus I also experimentally assess the ability of alkaline melts and fluids associated with sediment melting to carry lithophile and chalcophile elements in the sub-arc.

I measured the chemical composition of 18 plutonic samples from the Bonanza island arc, emplaced between 203 and 164 Ma on the Wrangellia terrane on Vancouver Island, British Columbia. Models using trace elements with Nd and Sr isotopes indicate < 10% assimilation of the Wrangellia basement by the Bonanza arc magmas. The Bonanza arc rare earth element geochemistry is best explained as two lineages, each with two fractionation stages implicating < 15% garnet crystallization. My inference of garnet-bearing cumulates in the unexposed lower crust of the Bonanza arc, an unsuspected similarity with the coeval Talkeetna arc (Alaska), is consistent with estimates from geologic mapping and geobarometry indicating that the arc grew to > 23 km total thickness. The age distribution of the Bonanza arc plutons shows a single peak at 171 Ma whereas the volcanic rock age distribution shows two peaks at 171 and 198 Ma, likely due to sampling and/or preservation bias. Numerous mechanisms may produce the E-W separation of young and old volcanism and this does not constrain Jurassic subduction polarity beneath Wrangellia.

Although a small component of arc magmatism, alkaline arc rocks are associated with economic concentrations of chalcophile elements. The effect of varying alkalinity on S Concentration at Sulfide Saturation (SCSS) has not been previously tested. Thus, I conducted experiments on hydrous basaltic andesite melts with systematically varied alkalinity at 1270°C and 1 GPa using piston-cylinder apparatus. At oxygen fugacity two log units below the fayalite magnetite quartz buffer, I find SCSS is correlated with total alkali concentration, perhaps a result of the increased non-bridging oxygen associated with increased alkalinity. A limit to the effect of alkalis on SCSS in hydrous melts is observed at ~7.5 wt.% total alkalis. Using my results and published data, I retrained earlier SCSS models and developed a new empirical model using the optical basicity compositional parameter, predicting SCSS with slightly better accuracy than previous models.

Sediment melts contribute to the trace element signature of arcs and the chalcophile elements, compatible in redox-sensitive sulfide, are of particular interest. I conducted experiments at 3 GPa, 950 – 1050°C on sediment melts, determined fluid concentrations by mass balance and report the first fluid-melt partition coefficients ($D^{fluid/melt}$) for sediment melting. Compared to oxidized, anhydrite-bearing melts, I observe high $D^{fluid/melt}$ for chalcophile elements and low values for Ce in reduced, pyrrhotite-bearing melts. Vanadium and Sc are unaffected by redox. The contrasting fluid-melt behaviour of Ce and Mo that I report indicates that melt, not fluid, is responsible for elevated Mo in the well-studied Lesser Antilles arc.

Table of Contents

List of Tables

List of Figures

Acknowledgments

For any effort I have ever undertaken, I have benefitted greatly from the support of many good people. I am foremost indebted to Dante for introducing me to and instructing me in the dark arts of experimental petrology and for his good humour and patience in the same. Of all the things I have learned from Dante, I am especially grateful for his lesson to push past my 'academic comfort zones'. Next to Dante, I thank my supervisory committee, Stephen, Laurence and Alex, for always always being available to answer my questions and challenge my assumptions. Analytical work by and technical assistance from Jody Spence, Mati Raudsepp, Edith Czech, Andrew Locock, Krystle Moore, Alex Wlasenko, Stas Konorov, Milton Wang and Elaine Humphery is also gratefully acknowledged. Careful monitoring of the my progress (and all the other graduate students!) by Allison Rose was greatly appreciated. Additionally, I thank Kim Smith, Kalisa Valenzuela and Terry Russell for also keeping the gears well-oiled for all the graduate students. Thanks also to David Nelles and his Senior Lab Instructor colleagues, Duncan Johannessen and Sarah Thornton, whose smooth-running courses allowed me to supplement my stiped by TA-ing without also needing to worry about the underlying mechanics of the courses.

Over the last five years, my friends in Victoria and elsewhere have celebrated successes with me and have kept my spirits up during difficult times over food, drink, movies, conversation and comiseration. I apologize for the names that I forget but, Shawna L., Eric V., Alisha, Genevieve, Mina, Rebecca, Sven, Steve, Ben (the English one), John, Angus, Kurt, Mei Mei and Lindsey. In particular, I thank Eric B., Dana, Noland, Ana, Faye, Shawna W., Darin, Wendy, Olivia, Darsi and Raymond for graciously opening their homes to me during my travels for analytical work. I am also extremely grateful to Ben (the American one), with whom I started my Ph.D. and soon after became fast friends, sharing a strange sense of humour and a love for scotch and stairwells. Everyone should be as lucky to know so many wonderful people and call them friends.

Everything in the last five years would have been immeasurably less colourful without the love and support of my wonderful fiancée, Fiona. Her kindness, patience, delicious food and belief in me tapped the deepest and most reliable sources of strength I have ever known and I am incredibly grateful. Fiona, her family and William T. Chapelcat have been little islands of welcome craziness amid storms of uninvited madness.

Lastly, this and all the preceding work and play I have been lucky to have had would have been impossible without Dad, Mum and Sarah. Their love and encouragement, with their examples of dedication and perseverance, kept me bouyed in the difficult times and all but ensured my success. For all of this and so much more, thank you.

For Mum and Dad.

Their encouragement, first, to bring home all the rocks I fancied and, years later, to study them to my hearts content, is why you are reading this.

Chapter 1.
Introduction

1.1 Background

Earth is unique among the terrestrial planets of the Solar system in having, among other things, active plate tectonics in the present day and a chemically evolved continental crust (Taylor, 1989). The continental crust, although only ~0.4% of Earth's mass, contains ~30% of the bulk abundance of incompatible elements (e.g. Cs, Rb, K, U, Th; Taylor and Maclennan, 1995), making it an important part of the planet's geochemical budget. The bulk continental crust is broadly andesitic in composition and bears striking resemblance to andesitic rocks erupted at volcanic arcs (e.g. Taylor, 1977; Taylor and McLennan, 1995; Rudnick, 1995; Rudnick and Gao, 2003). On the basis of this geochemical similarity, it has long been postulated that Earth's continents formed at volcanic arcs, thus understanding the processes occurring at these convergent margins is key to understanding the formation and evolution of the continental crust.

Volcanic arcs, formed where tectonic plates converge, are among the most spectacular surface expressions of plate tectonics, exemplified by continental arc volcanoes like Mt. St. Helens and Mt. Baker, and island arcs like the Izu Bonin volcanic chain. These volcanoes are fed by melts from the mantle wedge between subducting oceanic lithosphere and over-riding continental or oceanic plates (Figure 1.1). These melts may result from fluid fluxed melting of the sub-arc mantle (e.g. Green, 1980), by melting of the sedimentary veneer of subducting crust (e.g. Plank and Langmuir, 1998), possibly aided by rising as buoyant diapirs into the hot mantle (Marsh, 1979; Gerya *et al.*, 2006; Marschall and Schumacher, 2012), or some combination of these processes. Rocks produced at volcanic arcs are enriched relative to mid-ocean ridge basalt (MORB) in

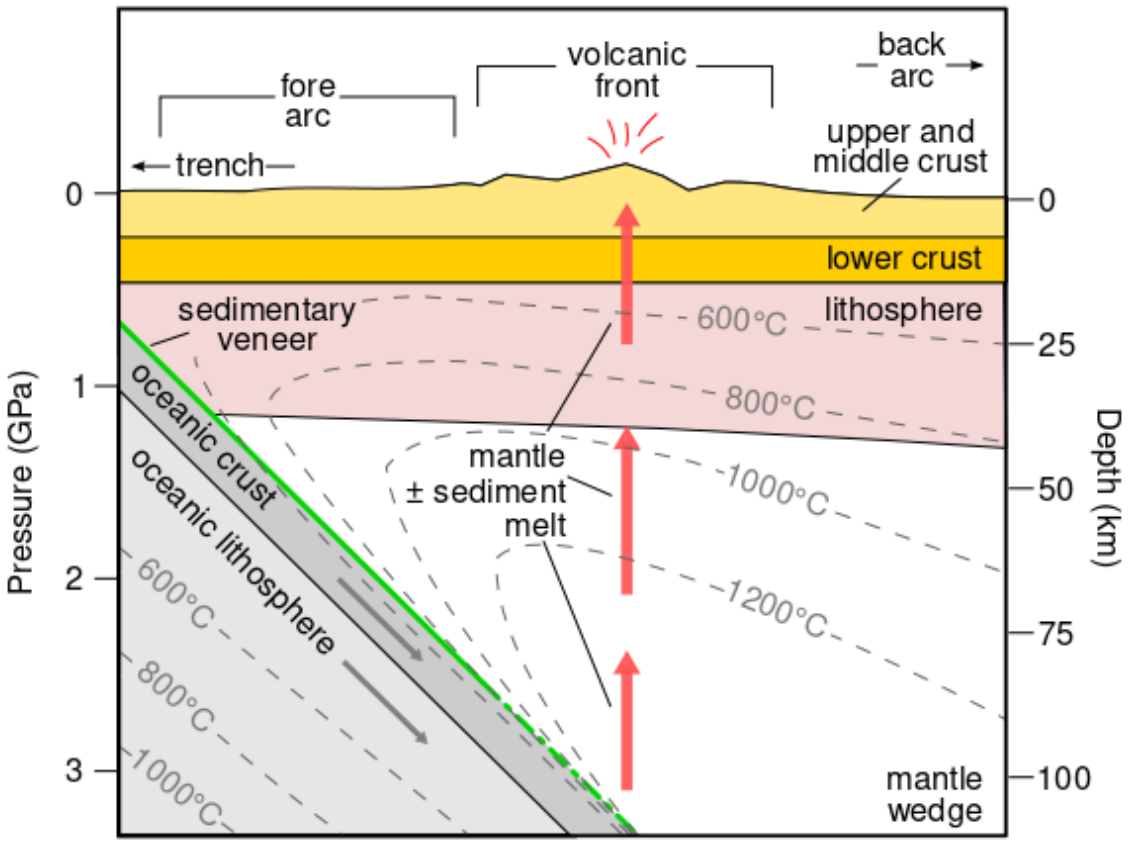

Figure 1.1: A schematic cross-section of an island arc. The subducted sedimentary veneer is shown here to persist to a depth of approximately 100 km where it undergoes partial melting. Sediment melts mix with mantle melts produced by dehydration reactions occuring in the subducting slab and these rise through the mantle wedge and over-riding lithosphere towards the upper crust where they erupt at the volcanic fromt.

large ion lithophile elements (LILE, e.g. Rb, Cs, K, Ba) and light rare earth elements. Porphyry Cu deposits are also associated with arcs and have very high concentrations of chalcophile elements (e.g. S, Cu, Mo, As, Pb; Sillitoe, 2010). The enrichment in LILE in arcs are accompanied by depletion in high field strength elements (HFSE, e.g. Nb, Ta) compared to mid-ocean-ridge basalt, resulting in the high LILE/HFSE 'arc signature'. It is generally accepted that fluids released by dehydration of hydrous phases in the subducting slab (e.g. chlorite and serpentine; Schmidt and Poli, 1998) carry LILE into the arc mantle (Green, 1980; Green and Adam, 2003), whereas the HFSE are retained in phases like rutile in the slab (Stadler *et al.*, 1998) and thus relatively depleted in arc rocks.

Although only the volcanic edifice of presently active arcs are easily accessible, the processes occurring at depth that govern the geochemistry of arcs can be determined by examining ancient arcs whose deep levels have been tectonically uplifted to the present day surface. In such so-called 'inverse studies', insights into the deep processes of arcs, such as fractionation of minerals, are obtained by comparing the chemistry of the upper stratigraphic arc levels to the mineralogy and chemistry of lower crustal rocks. For example, ancient arcs like tthe Kohistan and Talkeetna arcs in Pakistan and Alaska, respectively (Jagoutz *et al.*, 2007; DeBari and Coleman, 1989), have a remarkable completeness of exposure, from upper- and mid-crustal volcanic and plutonic rocks to the garnet-bearing cumulate rocks in the lower crust. It is significant that the Talkeetna and Kohistan arcs have a garnet-bearing lower crust as these rocks can be negatively buoyant relative to the mantle, resulting in delamination of the lower crust thereby shifting the bulk composition of the arc from basaltic to andesitic, i.e. similar to continental crust

(e.g. Kay and Mahlburg-Kay, 1991). Further, as garnet is only stable in crust thicker than 24 km (Müntener and Ulmer , 2006), its presence also provides an independent constraint on the minimum thickness of these arcs against which structural reconstructions may be compared.

Of the volatile component in arc volcanic eruptions, S is the third most abundant element (Wallace and Edmonds, 2011) and other chalcophile elements, like Cu and Mo, are found in high concentrations in sulfide minerals in porphyry Cu deposits (PCD) associated with mature, thick arcs (e.g. Sillitoe, 2010). Thus the arc setting is an important part of the geological cycling of S and other chalcophile elements. Through experiments (i.e. a 'forward approach'), the solubility of S at geologically relevant reduced conditions, where sulfide is the stable mineral the so-called S concentration at sulfide saturation (SCSS) of a silicate melt is known to be strongly controlled by temperature, pressure and melt composition, in particular the Fe and SiO_2 content. Although there have been few SCSSS experimenotal investigations on hydrous arc magma compositions, these show a positive correlation of SCSS and H_2O (e.g. Fortin *et al.*, 2015). Low pressure experiments and natural fluid inclusion studies show that aqueous fluids are an effective carrier of Cu, Mo and other chalcophile elements and that PCD are likely produced by chalcophile element precipitation from such fluids.

1.2 Outstanding questions

Although we have learned much about subduction zone processes from forward and inverse studies, many questions remain. For example, the Talkeetna and Kohistan arcs are difficult compare to other ancient arcs which are not as completely exposed. For example, only the upper and middle crustal levels of the Jurassic Bonanza arc on

Vancouver Island, Canada, is exposed and the lower crustal composition is enigmatic, making comparisons with the coeval Talkeetna arc difficult (DeBari *et al.*, 1999). Furthermore, the Bonanza arc was also emplaced on pre-exisiting non-oceanic crust and it is possible that the primary geochemistry of the Bonanza arc is masked by assimilation of older rocks. These features of the Bonanza arc, and other arcs like it, beg questions regarding the extent of assimilation of older material, the mineralogical composition of the lower arc crust and the total thickness of the arc and its substrate.

Arc magmas are known to evolve to increasingly alkaline composition as arcs mature and thicken (Green, 1980). Increasing alkalinity increases the number of non-bridging oxygen (NBO) atoms in the silicate melt structure. As S replaces NBO in a silicate melt (Fincham and Richardson, 1954), SCSS is expected to increase with melt alkalinity which implies that alkaline magmas from mature arcs are able to carry higher concentrations of S. Such a link might explain in part the association of PCD with thick arcs and also with alkaline magmatism (e.g. Sillitoe, 2010; Logan and Mihalynuk, 2014). The link between alkalinity and SCSS has not previously been directly tested however.

There is much published experimental work pertaining to PCD formation in the upper crust that shows that chalcophile elements are highly mobile in aqueous fluids, although the ultimate source of these chalcophile elements is ambiguous. The sedimentary veneer overlying a subducting slab can be a potent source of some chalcophile elements (e.g. Plank and Langmuir, 1993, 1998). Evidence from arc geochemistry (Labanieh *et al.*, 2012) and exhumed subduction-related rocks (Penniston-Dorland *et al.*, 2015) indicates subducted sediments can reach super-solidus temperatures at depths of melt generation (i.e. ~100 – 150 km). Although melts cannot carry high concentrations of chalcophile

elements (ppm levels), fluids associated with sediment melting may play a significant role (e.g. Freymuth *et al.*, 2016). However, no previous work has attempted to quantify the fluid-melt partitioning of chalcophile elements at the high pressure conditions relevant to sediment melting beneath arcs.

1.3 Research approaches

In Chapter 2, I have determined the extent of assimilation of pre-existing crust by Bonanza arc magmas, by analyzing and modeling the variation in Sr and Nd radiogenic isotopes of Bonanza arc samples. Following this, I assessed the likely fractionating mineral assemblages that could produce the Rare Earth Element (REE) geochemistry observed in the Bonanza arc rocks and show that garnet, though not observed at the surface, must have been a fractionating phase in the lower crust of the Bonanza arc. Finally, I used the mapped extents of the various crustal units of the Bonanza arc exposed on Saanich Peninsula, Vancouver Island, to estimate the true thickness of the Bonanza arc as a test of my conclusions from the REE modeling. The data and interpretations presented in this chapter indicate previously unknown similarities between the Bonanza arc and the better-studied Talkeetna arc in Alaska.

Chapter 3 is an experimental study of how SCSS changes as a function of melt alkalinity in arc-like hydrous basaltic andesites. In detail, I conducted experiments at 1 GPa (i.e. ~30 km depth) and 1270°C using a piston cylinder apparatus and five synthetic starting materials ranging in total alkali content from 2 – 8 wt.%, and produced silicate melts in equilibrium with sulfide droplets. My results show that SCSS is proportional to total alkali content and, importantly, suggests a limit to increasing SCSS solely by increasing total alkali content. I use my experimental results to assess how well

previously published empirical SCSS models (Liu *et al.*, 2007; Li and Ripley, 2009; Fortin *et al.*, 2015) perform with changing alkalinity. I find that updating the previous models with my experimental data improves their performance in predicting SCSS with alkalinity. I also develop a new SCSS model of my own using optical basicity (e.g. Mills, 1993) as a compositional parameter and show that this model produces a better fit to published SCSS experiments.

Chapter 4 is an experimental investigation of the ability of fluids to move chalcophile and lithophile elements at the conditions of sediment melting beneath arcs. I examine the partitioning of lithophile (V, Sc and Ce) and chalcophile (S, Mo, As, Sb and Pb) elements between aqueous fluids and sediment melts at 3 GPa and 950 – 1050°C using a piston cylinder apparatus. In addition to quenched silicate melt, silicate minerals and fluid bubbles, my experiments contain pyrrhotite and anhydrite as the stable S-bearing mineral at reduced and oxidized conditions, respectively. The major and trace element composition of the melt phase was measured directly by electron probe and laser ablation inductively coupled plasma mass spectroscopy and the fluid composition was determined by mass balance. Using these results, I calculate the first fluid-melt partition coefficients for S, Sc, V, Ce, Mo, As, Sb and Pb in oxidized and reduced conditions and pressures and temperatures relating to sediment melting. My results show that redox conditions dramatically change the fluid-melt partitioning of the chalcophile elements and of Ce as well.

1.4 Dissertation outline

This dissertation is presented as five chapters. Chapter 1 (i.e. this chapter) provides a unifying framework for the dissertation and serves as a brief introduction to the specific

research questions I have studied and my findings. Chapters 2, 3 and 4 are each a complete and self-contained paper for which I am the first author and Dante Canil, my supervisor, is a co-author. Chapter 2 has been published in the Geological Society of America Bulletin (D'Souza *et al.*, 2016) and Robert A. Creaser is an additional co-author, having guided me in the collection of radiogenic isotope data used in that study. At the time of this writing, Chapters 3 and 4 have been submitted for peer-review in American Mineralogist and Earth and Planetary Science Letters respectively. The concluding chapter of this dissertation, Chapter 5, is a summary of the findings of the preceding three chapters and outlines how these studies contribute to our understanding of the processes operating in volcanics arcs and the underlying mantle. Chapter 5 and the dissertation concludes with some suggestions for future research in these regards.

Chapter 2.
Assimilation, differentiation and thickening during formation of arc crust in space and time: the Jurassic Bonanza arc, Vancouver Island, Canada

2.1 Abstract

Continental arcs and island arcs, eventually accreted to continental margins, are thought to have been the locus of continental growth since at least the Proterozoic eon. The Jurassic Bonanza arc, part of the Wrangellia terrane on Vancouver Island, British Columbia, exposes the stratigraphy of an island arc emplaced between 203 and 164 Ma on a thick pre-existing substrate of non-continental origin. I measured the bulk major and trace element geochemistry, Rb-Sr and Sm-Nd isotope compositions of 18 plutonic samples to establish if differentiation involved contamination of the Bonanza arc magmas by the pre-Jurassic basement rocks. The $^{87}Sr/^{88}Sr$ and $^{143}Nd/^{144}Nd$ isotope ratios of the plutonic rocks at 180 Ma vary from 0.70253 – 0.7066 and 0.512594 – 0.512717, respectively. Assimilation-Fractional Crystallization modelling using trace element concentration and Nd and Sr isotope ratios indicate that contamination by a Devonian island arc in the Wrangellia basement is less than 10%. Rare earth element modelling indicates that the observed geochemistry of Bonanza arc rocks represents two lineages, each defined by two-stages of fractionation that implicate removal of garnet, varying in modal proportion up to 15%. Garnet-bearing cumulate rocks have not been reported from the Bonanza arc, but their inference is consistent with my crustal thickness estimates from geological mapping and geobarometry indicating that the arc grew to at least 23 km total thickness. The inference of garnet-bearing cumulate rocks in the Bonanaza arc is a previously unsuspected similarity with the coeval Talkeetna arc (Alaska), where garnet-bearing cumulate rocks have been described. Geochronological data from the Bonanza

arc shows a continuum in plutonic ages from 164 to 203 Ma whereas the volcanic rocks show a bimodal age distribution over the same span of time with modes at 171 and 198 Ma. I argue that the bimodal volcanic age distribution is likely due to sampling or preservation bias. East-west separation of regions of young and old volcanism could be produced by roll-back of a west-dipping slab, fore-arc erosion by an east-dipping slab, or juxtaposition of two arcs along arc-parallel strike-slip faults.

2.2 Introduction

The continental crust is thought to be broadly andesitic in composition and its lower density compared to the underlying mantle has resulted in its preservation over geologic time (Taylor, 1977; Rudnick, 1995; Rudnick and Gao, 2014). Today, andesites that are similar in composition to the bulk continental crust are formed in convergent margin settings (Arculus and Johnson, 1978) leading to the hypothesis that continental crust is being produced at island arcs and continental arcs (Condie, 1989; Rudnick, 1995). As oceanic plates subduct, island arcs formed thereupon are accreted to the margins of overriding continents (e.g. Condie, 1990). Such tectonic accretion has exposed the complete stratigraphy of some ancient arcs allowing their bulk chemistry to be assessed – for example, the Talkeetna arc in Alaska (DeBari and Sleep, 1991) and the Kohistan arc in Pakistan (Jagoutz and Schmidt, 2012). On the basis of these mass-balanced average compositions it is generally accepted that the bulk chemistry of arcs, and therefore their parental melt, is basaltic (DeBari and Sleep, 1991) and that arcs are refined to the andesitic character of the continental crust by some subsequent process. Various hypotheses have been presented to produce andesitic crust at convergent margins, including assimilation by the primary arc magma of pre-existing continental crust (e.g.

Hildreth and Moorbath, 1988; Annen *et al.*, 2006), melting of the subducting slab (Defant and Drummond, 1990; Kelemen *et al.*, 2014), andesite magma formation by mantle melting fluxed by subduction-related fluids (Rapp *et al.*, 1999; Grove *et al.*, 2002), garnet fractionation (Macpherson, 2008) or granite formation by amphibole biotite gabbro fractionation from medium to high-K basalt (Sisson *et al.*, 2005). Density sorting by relamination of subducted sediments at the base of the continental crust (Hacker *et al.*, 2011) and delamination or erosion of dense mafic lower crust (Bird, 1979; von Huene and Scholl, 1991; Kay and Mahlburg-Kay, 1991) can further refine the bulk composition of arcs and is thought to be why the Kohistan arc has an andesitic bulk composition (Jagoutz and Schmidt, 2012). Delamination of the dense lower crust may also result in the formation of the Continental Moho (Jagoutz and Behn, 2013).

As an arc thickens with time, post-segregation magma differentiation may proceed at progressively deeper levels. The effect of higher-pressure fractionation is observed in arc volcanic rocks as a progressive decrease in Yb, Fe and Cu content with increasing crustal thickness (Jagoutz, 2010; Chiaradia, 2013). Jagoutz (2010) attributes Yb depletion to the stabilization of garnet, in which Yb is highly compatible, in the fractionating assemblage as the crust thickens. Chiaradia (2013) attributes the decrease in Fe and Cu to the early crystallization of magnetite in magmas under higher pressure resulting in the crystallization of sulfides (Jenner *et al.*, 2010), thus decreasing the amount of Fe and Cu in the liquid.

A thickening arc may also provide greater opportunity for assimilation of pre-existing crust by the arc magmas at virtually all levels of the arc. The signature for assimilation using radiogenic isotopes is quite notable in continental arcs, but lesser so in oceanic arcs

because pre-existing, isotopically evolved crustal material is typically absent or less voluminous in oceanic crust (Hildreth and Moorbath, 1988). The Jurassic Bonanza arc on Vancouver Island is unique in that it is traditionally interpreted as an island arc, yet formed upon a Devonian–Triassic arc-oceanic plateau-carbonate succession – in other words a pre-existing crust that was formed in the oceanic realm. The Bonanza arc thus provides a snapshot of the evolution of an island arc being built on thick non-continental crust. In the present study I test whether chemical changes observed in the Bonanza arc rocks can be attributed to changing fractionating conditions in the arc. In particular, the combined thickness of the Bonanza arc and its substrate may have exceeded 24 km over the ~45 Myr history of the arc allowing the stabilization of garnet as a fractionating phase in the lower crust (Müntener and Ulmer, 2006) and thus affecting the chemistry of the magmas that ascended to higher levels. I first test if assimilation of older crustal material occurred and affected the trace element chemistry of the Bonanza arc rocks and then compare the effect of different modelled fractionating assemblages on the liquid REE concentration. Finally, I examine the spatial distribution and timing of magmatism in the Bonanza arc to determine how the arc might have evolved with time.

2.3 Regional geology

The Bonanza arc was emplaced between 203 and 164 Ma, as an island arc on a substrate comprising the Devonian Sicker arc, the carbonates of the Buttle Lake Group, the Triassic Karmutsen plateau basalt, Quatsino carbonates and the late Triassic clastic Parson Bay formation (Figure 2.1a, b). Deltaic and marine conglomerates, sandstones, siltstone and shale of the Cretaceous Nanaimo Group (Muller, 1977) overlie the Bonanza arc rocks. The Bonanza arc is coveal with the Jurassic Talkeetna arc in Alaska (DeBari

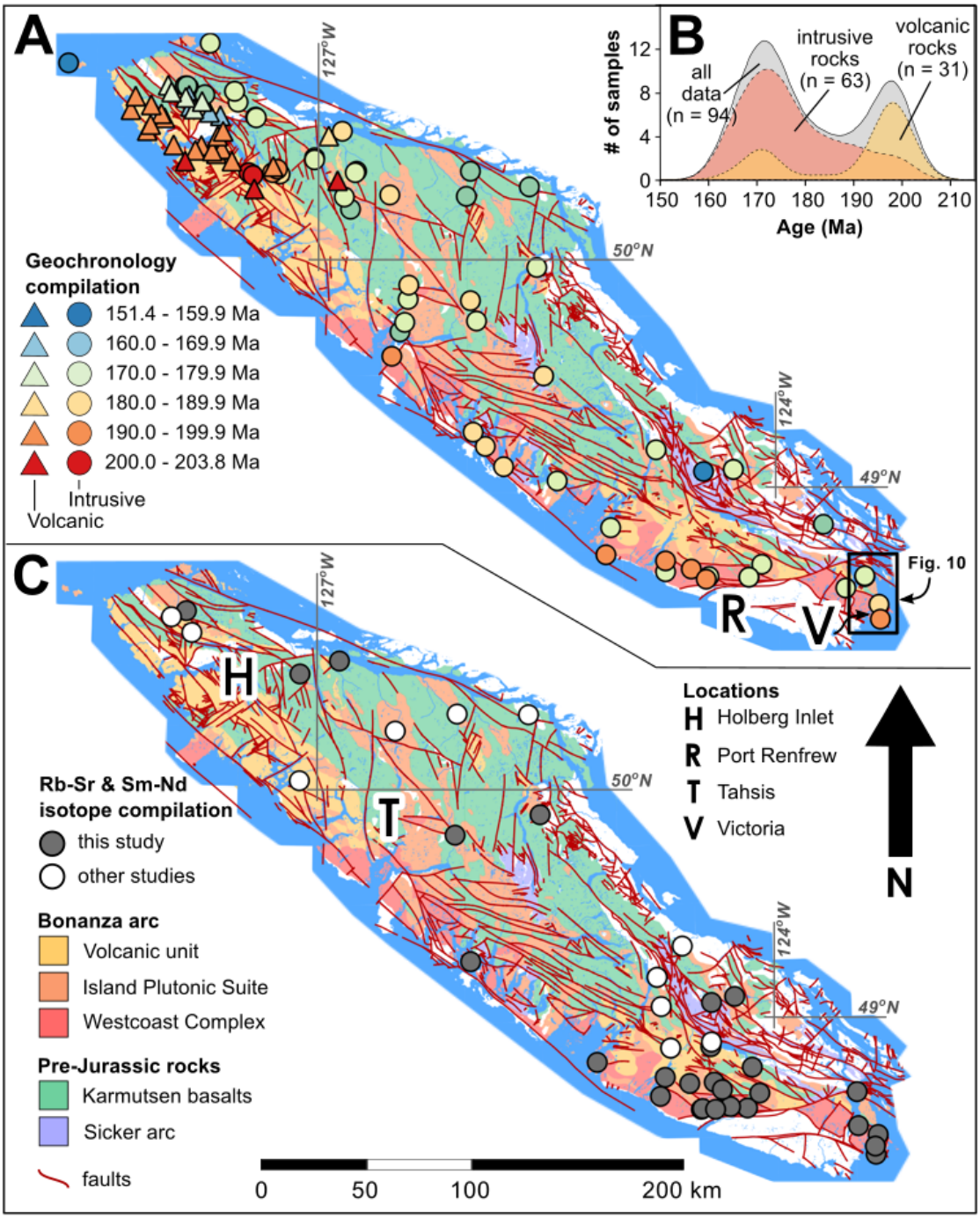

Figure 2.1: a) Geological map of Vancouver Island, showing the units of the Jurassic Bonanza arc and the pre-Jurassic crust and the locations and ages of the intrusive and volcanic Bonanza arc rocks that have been dated in other studies (zircon U-Pb and hornblende Ar-Ar). The black rectangle shows the location of Figure 2.10. b) The distribution of Bonanza arc ages plotted as a Kernel Density Estimate (Vermeesch, 2012). c) The locations of Bonanza arc samples with measured Rb-Sr and Sm-Nd isotopic ratios from this study and others.

et al., 1999) but there are some important distinctions. In contrast to the Bonanza arc, the basement of the Talkeetna arc is exposed and the latter arc may have developed directly on oceanic crust (DeBari and Sleep, 1991). Additionally, garnet-bearing cumulate rocks are present in the Talkeetna arc section but not in the Bonanza arc (DeBari *et al.*, 1999).

The Bonanza arc has traditionally been divided into a volcanic unit and two plutonic units, namely the Island Plutonic Suite and Westcoast Complex (Figure 2.1; Muller, 1977). The volcanic unit comprises flows, breccias and tuffs of basalt, andesite, dacite and rhyolite. The Island Plutonic Suite is made up of plutons of quartz diorite, granodiorite, quartz monzonite and tonalite, which are in sharp contact with the Bonanza volcanic unit and the older Karmutsen Formation. Geobarometry indicates a restricted and generally uniform depth of equilibration of 2 – 10 km for the Island Plutonic Suite (Canil *et al.*, 2010). The Westcoast Complex is composed of hornblendites and gabbroic to granodioritic rocks found in contact with rocks of the Devonian Sicker arc (DeBari *et al.*, 1999). The Westcoast Complex shows equilibration depths of 10 – 17 km using Al-in-hornblende geobarometry, but those results have high uncertainty (Canil *et al.*, 2010). Amphibole-bearing ultramafic cumulate rocks occur as schlieren and layers in intermediate plutonic units of the Bonanza arc near Port Renfrew and Tahsis (Figure 2.1 - Larocque, 2008; Fecova, 2009; Larocque and Canil, 2010). Al-in-hornblende barometry (Larocque and Canil, 2010) indicates that the ultramafic rocks from the Port Renfrew area equilibrated at depths of 15 – 25 km, again with high uncertainty.

The Island Plutonic Suite has traditionally been described as being unfoliated and more felsic than the Westcoast Complex (Muller, 1977). However, this distinction has proven difficult to apply in the field and can be imprecise as both units can overlap considerably

in bulk chemistry (Canil *et al.*, 2013). Hereafter, I avoid confusion and refer to samples of the Island Plutonic Suite and Westcoast Complex collectively as the Bonanza arc intrusive rocks.

2.4 Methods

I analyzed a suite of 18 Bonanza arc intrusive rocks sampled across Vancouver Island (Figure 2.1). The samples I analyzed had been collected in previous sampling campaigns carried out by D. Canil and J. Larocque. Detailed petrography of these samples is provided in Larocque (2008). After trimming off weathered surfaces with a diamond saw, samples were crushed into cm-sized fragments in a steel jaw crusher and ground to a fine powder in an agate ball mill. Major and trace element abundances (Table 2.1) were determined using Inductively Coupled Plasma Optical Emission Spectrometry (ICP-OES) and Inductively Coupled Plasma Mass Spectrometry (ICP-MS), respectively, at Activation Laboratories Ltd. (Ancaster, Ontario, Canada). Analytical results for certified reference materials were within 3% of the certified values for all elements, except V, Cu, Ce, Pr, Ho, Er, Tm and Nb (within 8%). The Rb-Sr and Sm-Nd isotopic ratios of the 18 samples and two additional samples (JL06-054 and DC06-047 from Larocque and Canil, 2010; Figure 2.1c) were measured at the Radiogenic Isotope Facility at the University of Alberta, Edmonton, Canada (Table 2.2). Aliquots of powdered samples were dissolved and spiked, followed by chromatographic separation of Rb, Sr, Sm and Nd using ion exchange columns. The isotopic ratios of Sr, Sm and Nd in each sample was determined by multi collector ICP-MS. Rubidium isotopic composition was determined using Thermal Ionization Mass Spectrometry. Specific details of Rb, Sr, Sm and Nd separation and analytical procedures can be found in Creaser *et al.* (1997, 2004).

Sample	07JST 1-1-1	07JST 13-1-1	07JST 27-2-1	ARGO	BAMF	DC06-061	DC06-62	DC07-02	DC09-01	DC10-01	JL06-034	JL06-065	JL06-082	MVD809-25	DCMD04	MVDB 09-11	JL06-114	DCMV09	JL06-027†
Rock Type	Granodiorite	Tonalite	Granodiorite	Granodiorite	Granodiorite	Granodiorite	Granodiorite	Granodiorite	Diorite	Granodiorite	Granite	Granite	Granodiorite	Diorite	Diorite	Granodiorite	Gabbro	Diorite	Basalt
Map Unit*	IPS	IPS	IPS	IPS	IPS	IPS	IPS	IPS	IPS	IPS	IPS	IPS	IPS	WCC	WCC	WCC	WCC	WCC	Volcanic
Latitude (°N)	50.53699	50.48156	50.73843	49.88626	48.82746	49.07460	49.09704	49.79812	48.67548	49.26186	48.70159	48.75966	48.79618	48.44179	48.49157	48.40733	48.61893	48.53057	48.68136
Longitude (°W)	126.84115	127.10198	127.87168	125.50384	125.14727	124.40486	124.25343	126.06555	123.48395	125.96385	124.34745	124.70980	124.14860	123.37797	123.35596	123.37517	124.39348	123.48030	124.23685
Major elements (wt.%) - ICP-OES																			
SiO_2	64.47	65.96	64.39	66.65	72.96	67.76	56.00	70.38	65.08	71.11	73.79	69.56	59.50	51.06	52.83	58.81	46.72	49.10	44.53
TiO_2	0.53	0.51	0.62	0.47	0.22	0.33	0.74	0.29	0.45	0.25	0.09	0.52	0.70	1.30	0.78	0.80	0.23	1.12	0.70
Al_2O_3	15.77	15.55	15.29	15.67	12.99	14.66	17.24	14.47	14.87	13.84	13.12	14.14	16.13	17.43	17.73	15.81	25.45	18.90	14.81
FeO†	4.44	4.56	5.43	4.01	2.02	3.59	7.08	2.65	4.54	2.19	1.62	2.92	6.15	8.60	7.61	6.24	3.40	9.43	10.80
MnO	0.08	0.12	0.11	0.05	0.06	0.10	0.14	0.08	0.09	0.03	0.04	0.08	0.12	0.19	0.17	0.12	0.07	0.20	0.19
MgO	1.83	1.67	2.45	1.77	0.69	1.19	3.28	0.84	2.15	0.63	0.14	0.81	3.55	4.00	4.25	3.33	4.78	4.56	12.19
CaO	4.39	4.72	5.57	5.21	0.87	3.59	6.62	2.75	4.48	1.16	0.48	1.28	6.86	7.54	6.89	4.78	15.27	9.76	10.21
Na_2O	4.14	3.74	3.13	3.67	3.95	3.52	3.24	3.95	3.55	4.32	3.88	4.77	2.91	3.91	4.13	3.70	1.66	3.21	1.24
K_2O	2.19	1.64	2.11	2.09	3.26	2.36	2.15	2.28	1.02	3.35	4.61	3.43	0.79	1.46	2.05	2.25	0.20	0.44	0.48
P_2O_5	0.22	0.16	0.12	0.12	0.07	0.10	0.19	0.09	0.12	0.10	0.03	0.11	0.18	0.40	0.16	0.21	0.03	0.26	0.15
LOI	1.19	1.71	1.00	0.80	1.14	1.15	1.40	1.23	1.92	1.07	0.82	0.99	2.93	2.23	2.39	2.28	2.23	2.31	3.57
Total	99.74	100.80	100.80	101.00	98.44	98.94	99.47	99.31	99.38	98.29	98.82	98.93	100.50	99.69	99.85	99.02	100.40	100.30	100.10
Trace elements (ppm) - ICP-MS																			
Sc	8	8	19	13	4	8	23	6	14	5	3	8	22	28	22	20	18	32	47
V	89	82	152	115	27	74	210	45	115	27	9	36	193	243	201	177	74	301	246
Ba	707	441	657	875	849	995	781	913	788	1108	929	707	284	448	744	695	71	315	210
Sr	448	306	261	387	171	279	449	329	419	141	117	168	432	483	615	485	526	615	275
Y	14	15	26	18	17	12	25	13	14	19	29	36	21	28	14	23	5	17	15
Zr	150	117	165	142	97	99	126	80	96	109	136	233	95	99	47	60	10	24	24
Cr	< 20	< 20	< 20	< 20	< 20	< 20	< 20	< 20	< 20	< 20	< 20	< 20	20	60	< 20	< 20	470	30	157
Co	8	9	14	8	3	7	20	4	11	3	1	3	18	23	18	21	17	28	54
Ni	< 20	< 20	< 20	< 20	< 20	< 20	< 20	< 20	< 20	< 20	< 20	< 20	< 20	30	< 20	< 20	60	< 20	79
Cu	110	< 10	20	< 10	< 10	< 10	50	< 10	< 10	90	< 10	< 10	< 10	10	40	30	20	20	76
Zn	< 30	40	50	< 30	30	50	60	30	40	< 30	40	40	40	100	70	60	< 30	90	-
Ga	16	15	15	16	13	15	18	13	14	14	14	15	16	20	17	16	15	19	12
Rb	77	36	50	31	68	60	41	46	22	74	114	87	17	46	66	72	5	4	6
Nb	11	5	4	3	4	5	6	4	4	7	7	8	6	4	3	4	< 1	3	1
Mo	12	< 2	< 2	< 2	< 2	< 2	< 2	< 2	< 2	< 2	< 2	3	< 2	2	< 2	< 2	< 2	< 2	-
Cs	1.1	< 0.5	1.3	< 0.5	0.5	0.6	0.8	< 0.5	0.7	1.0	0.6	0.7	0.7	1.8	0.6	1.1	< 0.5	< 0.5	-
La	13.0	13.1	16.1	12.8	16.8	15.9	12.5	16.8	14.2	32.4	25.2	22.2	10.3	12.5	11.2	12.8	1.4	7.8	4.0
Ce	28.5	26.5	35.4	26.7	33.3	29.2	28.4	31.6	27.6	62.5	50.4	50.7	34.3	29.4	22.9	28.6	3.4	17.8	9.8
Pr	3.3	3.1	4.5	3.4	3.6	3.1	3.7	3.3	3.0	6.9	5.7	6.2	4.2	4.0	2.9	3.6	0.5	2.6	1.4
Nd	11.9	11.0	17.1	12.9	11.4	10.3	15.5	10.7	10.2	23.1	20.2	23.5	15.3	17.2	11.5	14.5	2.2	11.3	7.6
Sm	2.5	2.5	4.0	3.0	2.3	2.1	4.0	2.2	2.3	4.0	4.3	5.2	3.7	4.5	2.8	3.5	0.6	3.1	2.2
Eu	1.0	0.9	0.9	0.8	0.5	0.7	1.2	0.6	0.7	0.6	0.5	1.4	1.1	1.6	1.2	1.0	0.4	1.3	0.8
Gd	2.5	2.5	4.3	3.1	2.2	1.7	4.2	1.9	2.3	3.4	4.0	5.9	4.0	5.1	2.8	3.9	0.8	3.5	2.4
Tb	0.4	0.4	0.7	0.5	0.4	0.3	0.7	0.3	0.4	0.6	0.7	1.0	0.7	0.9	0.5	0.7	0.1	0.6	0.4
Dy	2.3	2.7	4.0	3.1	2.6	2.1	4.5	1.9	2.3	3.5	4.8	6.4	4.0	5.3	2.8	4.2	0.8	3.7	2.5
Ho	0.5	0.5	0.9	0.6	0.6	0.4	0.9	0.4	0.5	0.7	1.0	1.3	0.8	1.1	0.5	0.9	0.2	0.7	0.5
Er	1.4	1.6	2.8	1.9	1.8	1.2	2.8	1.2	1.4	2.0	3.0	3.9	2.3	3.1	1.6	2.6	0.5	2.1	1.5
Tm	0.2	0.3	0.4	0.3	0.3	0.2	0.4	0.2	0.2	0.3	0.5	0.6	0.4	0.5	0.2	0.4	0.1	0.3	0.2
Yb	1.5	1.7	3.0	2.1	2.1	1.5	3.0	1.4	1.6	2.0	3.2	4.3	2.4	3.2	1.7	2.6	0.4	2.0	1.4
Lu	0.3	0.3	0.5	0.4	0.4	0.3	0.5	0.3	0.3	0.4	0.6	0.7	0.4	0.5	0.3	0.4	0.1	0.3	0.2
Hf	3.4	2.8	4.4	3.9	2.7	2.7	3.3	2.3	2.3	4.0	4.3	5.7	2.5	2.5	1.5	1.9	0.3	0.8	0.8
Ta	0.8	0.3	0.3	0.3	0.4	0.4	0.4	0.3	0.2	0.2	0.4	0.5	0.4	2.0	0.1	0.2	< 0.1	0.1	0.1
Th	4.9	2.7	4.3	2.7	5.8	4.2	2.3	3.3	3.7	10.3	8.5	5.0	2.9	1.7	2.5	4.0	0.1	0.3	0.4
U	2.2	1.0	2.3	1.4	3.1	1.8	1.1	1.2	1.2	4.0	2.8	2.5	1.1	1.0	1.2	1.5	0.1	0.1	0.2

Note: * IPS = Island Plutonic Suite; WCC = Westcoast Crystalline Complex
† Analysis from Larocque (2008)

Table 2.1: Bulk rock major (wt.%) and trace element (ppm) concentrations

Sample	$^{87}Rb/^{86}Sr$	$^{87}Sr/^{86}Sr_0$	2 SE	$^{87}Sr/^{86}Sr_{180\ Ma}$	$^{147}Sm/^{144}Nd$	$^{143}Nd/^{144}Nd_0$	2 SE	$^{143}Nd/^{144}Nd_{180Ma}$	ϵNd_{180Ma}
07JST 1-1-1	0.5407	0.70508	0.00003	0.70369	0.1265	0.512794	0.000010	0.512645	4.7
07JST 13-1-1	0.3010	0.70477	0.00004	0.70400	0.1362	0.512872	0.000012	0.512712	6.0
07JST 27-2-1	0.5187	0.70486	0.00002	0.70353	0.1465	0.512828	0.000009	0.512655	4.9
ARGO	0.2153	0.70457	0.00002	0.70402	0.1395	0.512881	0.000006	0.512717	6.1
BAMF	1.0932	0.70672	0.00002	0.70392	0.1299	0.512813	0.000010	0.512660	4.9
DC06-61	0.5946	0.70548	0.00002	0.70396	0.1212	0.512764	0.000008	0.512622	4.2
DC06-62	0.2506	0.70460	0.00002	0.70396	0.1557	0.512837	0.000007	0.512654	4.8
DC07-02	0.3799	0.70757	0.00003	0.70660	0.1048	0.512775	0.000005	0.512651	4.8
DC09-01	0.1493	0.70448	0.00002	0.70410	0.1270	0.512744	0.000006	0.512594	3.7
DC10-01	1.5110	0.70716	0.00002	0.70329	0.1115	0.512796	0.000006	0.512665	5.0
DCMD04	0.3298	0.70428	0.00002	0.70343	0.1460	0.512807	0.000007	0.512635	4.5
DCMV09	0.0146	0.70390	0.00001	0.70386	0.1622	0.512861	0.000006	0.512670	5.2
JL06-034	2.7671	0.70962	0.00002	0.70253	0.1282	0.512781	0.000007	0.512630	4.4
JL06-065	1.4631	0.70770	0.00002	0.70396	0.1363	0.512853	0.000006	0.512692	5.6
JL06-082	0.1745	0.70444	0.00002	0.70399	0.1414	0.512762	0.000006	0.512595	3.7
JL06-114	0.0250	0.70365	0.00002	0.70358	0.1758	0.512894	0.000012	0.512687	5.5
MVDB09-11	0.4289	0.70480	0.00002	0.70371	0.1500	0.512892	0.000009	0.512716	6.0
MVDB09-25	0.2623	0.70430	0.00002	0.70363	0.1604	0.512894	0.000007	0.512705	5.8
DC06-047*	0.2577	0.70491	0.00001	0.70425	0.1660	0.512898	0.000006	0.512702	5.8
JL06-054*	4.2833	0.71386	0.00002	0.70289	0.1532	0.512807	0.000006	0.512626	4.3

$^{87}Rb/^{86}Sr$ and $^{147}Sm/^{144}Nd$ error is 2%

* whole rock chemistry reported in Larocque (2008)

Table 2.2: Rb-Sr and Sm-Nd isotopic composition of Bonanza arc rocks

Whole rock chemical and isotopic analyses from this study were combined with data from all previous work (Larocque, 2008; Larocque and Canil, 2010; Fecova, 2009; Paulson, 2010; DeBari *et al.*, 1999; Andrew *et al.*, 1991; Isachsen, 1987; Samson *et al.*, 1990). The geochronological database that I use was compiled from all available zircon U-Pb and igneous hornblende Ar-Ar ages (Isachsen, 1987; DeBari *et al.* 1999; Breitsprecher and Mortensen, 2004; Fecova, 2009; Nixon, 2011a-e; Canil *et al.*, 2012).

2.5 Results

The concentration of SiO_2 in the Bonanza arc samples analyzed in the present study (Table 2.1) varies from 46.7 to 73.8 wt.% and is negatively correlated with FeO^T, MgO and CaO (Figure 2.2) but is positively correlated with Na_2O and K_2O. All newly analyzed samples in this study are within the range of variation of Bonanza arc intrusive and volcanic rocks analyzed in previous work (Figure 2.2). Across all the Bonanza arc rocks, P_2O_5, Al_2O_3 and TiO_2 show an inflection from positive to negative correlation at ~50 wt. % SiO_2 (Figure 2.2). Compared to the intrusive rocks, the volcanic samples show generally lower SiO_2 concentration (< 60 wt.%). The Bonanza arc samples show similar ranges of major element concentrations as the Talkeetna and Kohistan arc rocks (Figure 2.2).

All samples, except JL06-114, are similarly enriched in the large ion lithophile elements (Rb, Ba, K, Pb and Sr) relative to MORB and show sharply negative Nb, Ta and Ti anomalies (Figure 2.3a). Chondrite-normalized (Figure 2.3b) REE patterns for the samples in this study all show light REE (La to Sm) enrichment relative to the middle and heavy REE (Eu to Lu). The intrusive rocks, except JL06-114, overlap the volcanic rocks

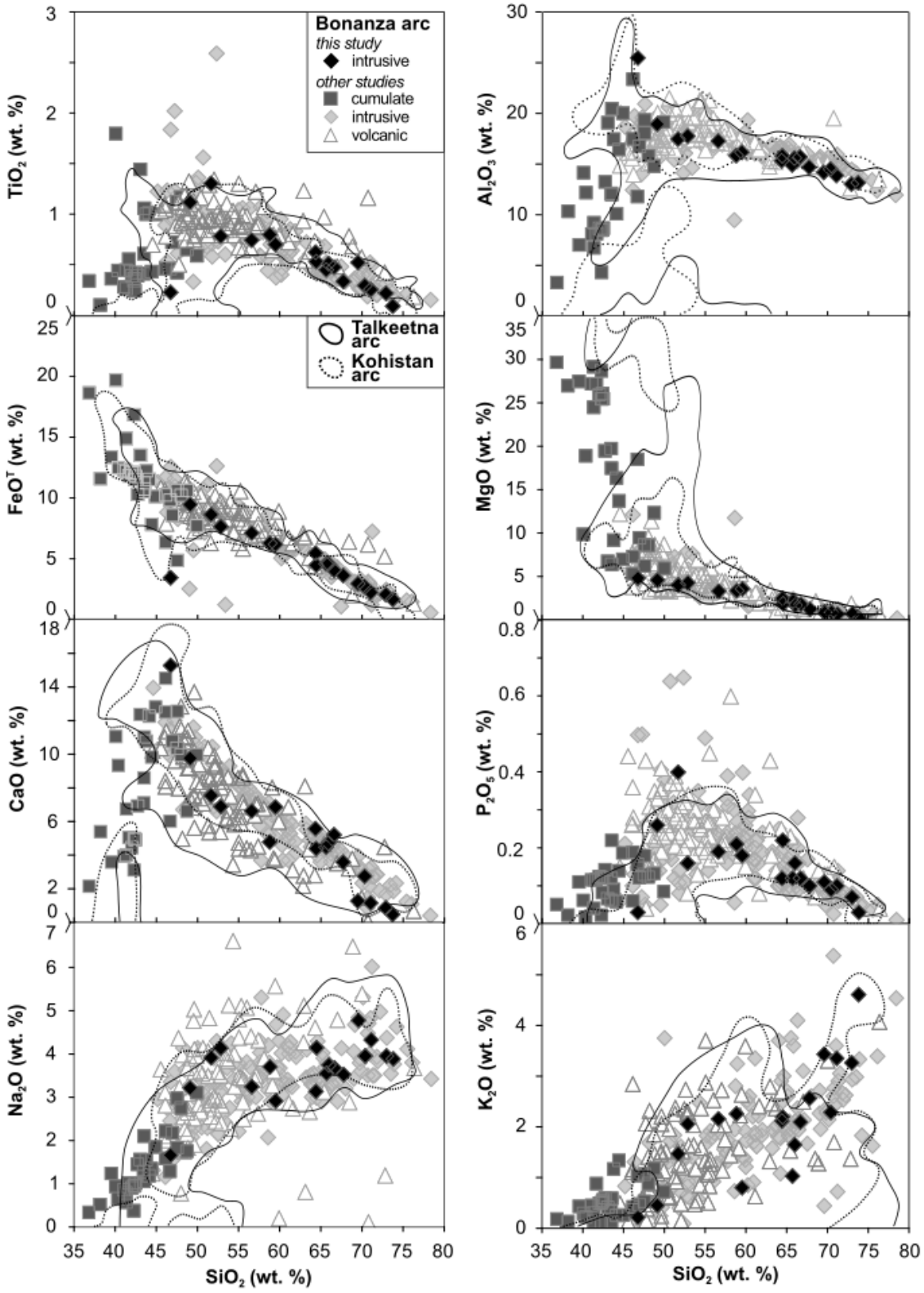

Figure 2.2: Silica variation diagrams showing the variation of major elements in Bonanza arc samples analyzed in this study and previous work. Also shown are fields for the Talkeetna and Kohistan arc data (Kelemen *et al.*, 2014; Jagoutz and Schmidt, 2012).

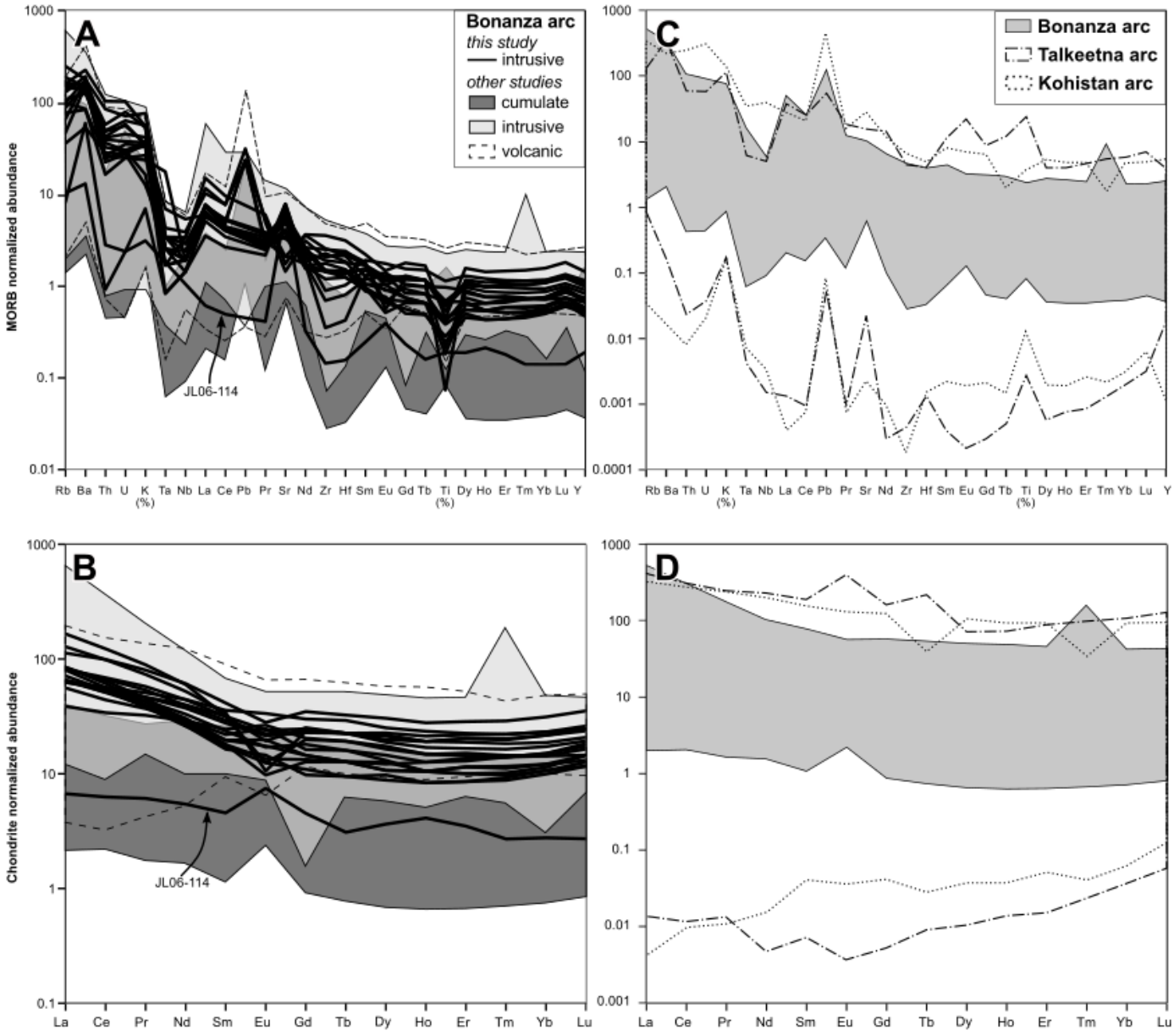

Figure 2.3: a) N-MORB normalized (Sun and McDonough, 1989) trace element profiles for samples analyzed in the present study (thick black lines) and those from the literature, grouped as volcanic, intrusive or cumulate rocks. b) Chondrite normalized (McDonough and Sun, 1995) REE profiles for Bonanza arc samples, as in panel a. c) Fields for the N-MORB normalized trace element profiles and d) chondrite normalized REE profiles for the Talkeetna and Kohistan arcs (Kelemen *et al.*, 2014; Jagoutz and Schmidt, 2012) and all Bonanza arc data, including samples analyzed in the present study.

in all trace element abundances (Figure 2.3). Sample JL06-114 is a layered gabbro (Larocque, 2008) and has major and trace element concentrations, similar to the cumulate rocks from Port Renfrew (Figure 2.2; Larocque and Canil, 2010). Compared to rocks from the Talkeetna and Kohistan arcs, the Bonanza arc rocks show restricted range of trace element abundances (Figure 2.3c, d).

The samples I analyzed (Figure 2.1c) show a wide range in present-day Sr isotope ratios (Table 2.2): $^{87}Rb/^{86}Sr$ from 0.0146 to 4.2833, and present day $^{87}Sr/^{88}Sr$ from 0.70365 to 0.71386. The Sr isotope ratios of samples in this study are within the range of those reported in previous work (Isachsen, 1987; Samson *et al.*; 1990; Andrew *et al.*, 1991) except for JL06-034 and JL06-054, which are granites with higher Sr isotope ratios. Present day $^{147}Sm/^{144}Nd$ varies from 0.1048 to 0.1758 and present day $^{143}Nd/^{144}Nd$ varies from 0.512744 to 0.512898 in the samples I analyzed, within the range reported in previous studies.

My compilation of geochronological data shows that the Bonanza arc intrusive rocks, sampled across Vancouver Island, have ages between 164 and 203 Ma (Figure 2.1b). The ages for volcanic rocks, have an overall range similar to that of the intrusive rocks but show a distinctly bimodal age distribution with peaks at 171 and 198 Ma, although these samples mostly come from samples collected on northern Vancouver Island.

2.6 Discussion

The effect of crustal thickness on the chemistry of arc magmas has a long history of study. In a classic paper, Miyashiro (1974) observed that as arc thickness increases, island arc volcanic rock series shift from tholeiitic to calc-alkaline. In a compilation of data from > 50 arc volcanoes, Mantle and Collins (2008) observed that increasing trace

element ratios such as Ce/Y, La/Yb and Zr/Y in erupted volcanic rocks as depth to the Moho increases for those arcs. Jagoutz (2010) compiled data from 12 arcs and highlighted a decrease in Yb concentration in arc rocks as crustal thickness increased. He postulated that this trend was due to the fractionation of garnet, a phase in which Yb is highly compatible, and was causally related to arc thickness, as garnet is only stable on the liquidus of arc magmas at depths greater than 24 km (0.8 GPa). Contrary to Jagoutz (2010), Mantle and Collins (2008) indicated that the heavy REE concentration, using Y as a proxy, did not decrease with arc thickness. Chiaradia (2013) compiled data from 23 Quaternary volcanic arcs and observed that the Fe and Cu content of arc volcanic series are on average lower in thick arcs than in thin arcs and attributed this to the early fractionation of magnetite and sulfides beneath thick arcs.

2.6.1 Assimilation of pre-existing crust in Wrangellia

During their ascent through the crust, the Bonanza arc magmas may have assimilated pre-existing crust of the Wrangellia terrane, thus obscuring the chemical signature of primary processes (e.g. fractional crystallization) that controlled the chemistry of magmas in the arc. To assess the extent of assimilation that the Bonanza arc magmas experienced, I examine the $^{87}Sr/^{86}Sr_{180\ Ma}$ and $\varepsilon Nd_{180\ Ma}$ of the samples analyzed in this study (Table 2.2) and reported in the literature. The effect of fluid alteration on Rb and Sr by post-emplacement metamorphism is expected to be minor as < 10% secondary minerals by mode are observed in the Bonanza arc rocks (Larocque and Canil, 2010) and this is supported by the correlation of Rb with other incompatible but immobile elements, Nb, Th and La (Figure A-1). I also attempted to minimize the geochemical effect of any

weathering by removing weathered surfaces and fractures from samples with a diamond saw prior to crushing and pulverizing the samples for analysis.

Assimilation of older, more evolved crustal material by a mantle-derived magma increases $^{87}Sr/^{86}Sr_{initial}$, lowers $\varepsilon Nd_{initial}$ and increases the concentration of Sr and Nd, both incompatible elements, in the melt. The combined effect of increasing concentration and changing isotopic ratios caused by assimilation produces a positive correlation between $^{87}Sr/^{86}Sr_{initial}$ and Sr concentration, and a negative correlation between $\varepsilon Nd_{initial}$ and Nd concentration. The Bonanza arc data show no correlation between isotopic ratios of Sr and Nd as element concentration increases (Figure 2.4). I argue that this indicates that there has been little assimilation of older crustal material by Bonanza arc magmas.

To more quantitatively assess the degree of assimilation experienced by the Bonanza arc magmas, I performed assimilation-fractional crystallization (AFC) calculations (DePaolo, 1981). I use a primary, uncontaminated melt with Nd and Sr concentration and isotopic ratios similar to basalt extracted from the Depleted Mantle at 180 Ma (Workman and Hart, 2005; White and Klein, 2014). I used two different contaminants in the AFC model calculations (Figure 2.4): the average of all the Devonian Sicker arc data (grey circle, solid lines) and the most isotopically evolved Sicker arc sample (black circle, dashed lines). The latter provides the greatest isotopic difference between melt and contaminant thereby indicating the minimum degree of contamination. As liquid compositions will change with contamination, I avoid uncertainties arising from resulting variations in mineral-liquid partition coefficients (D) by displaying the results of the AFC models (Figure 2.4) for a range of D values from very incompatible (D = 0.05) to neutral (D = 1.00). Although important to assess, I do not consider a Karmutsen Formation

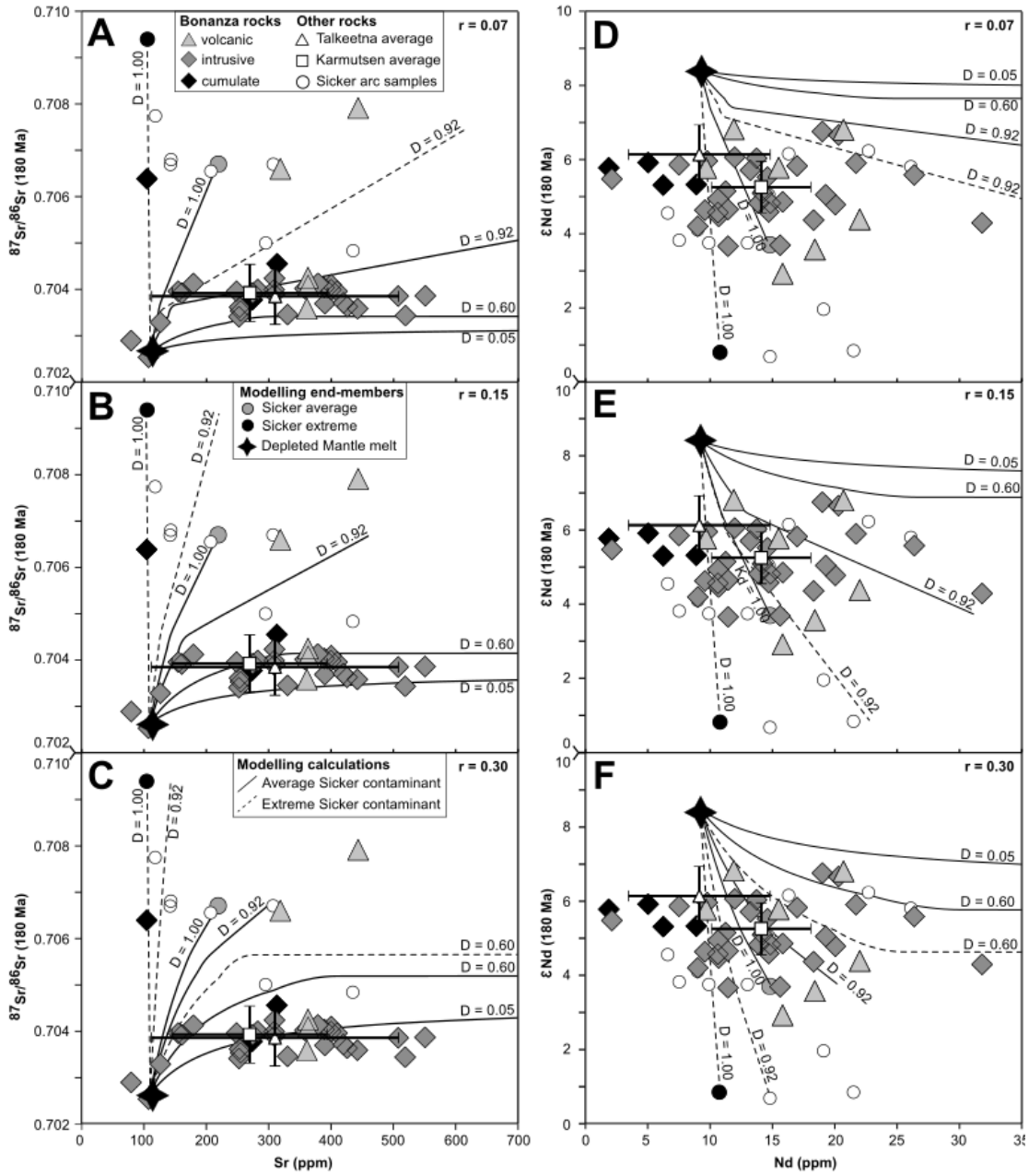

Figure 2.4: Assimilation-fractional crystallization (AFC) models for a melt from the Depleted Mantle and two possible contaminants: the average of the available Sicker arc data (solid lines) and an extreme sample from the Sicker arc (dashed lines). Three melt-contaminant ratios (r) are presented for Sr and Nd AFC models: a, d) r = 0.07; b, e) r = 0.15; c, f) r = 0.30. Curves have been calculated for different values of partition coefficient (D) for Sr and Nd, ranging from very incompatible (D = 0.05) to neutral (D = 1). At low D values, curves for the two contaminants are very similar and only the solid curve has been shown for clarity. The legend for all panels is split between panels a, b and c.

contaminant in the AFC models as those rocks have similar Nd and Sr concentration and isotopic ratios as the Bonanza arc samples (Figure 2.4) and AFC calculations would not yield a detectable signal.

AFC calculations using the average Sicker arc contaminant indicate that a contaminant-melt ratio between 0.07 and 0.15 is sufficient to explain all the Sr variation that I observe in the Bonanza arc (solid lines; Figure 2.4a–c). A model using the most isotopically evolved Sicker arc sample (dashed lines; Figure 2.4a–c) yields a maximum contaminant-melt ratio of 0.07. The AFC calculation results for Nd (Figure 2.4d–f) are equivocal in the case of both average and extreme Sicker arc contaminants, indicating contaminant-melt ratios between 0.07 and 0.30.

Eight Bonanza arc rocks that plot to the left of the D = 1.00 curve using the extreme Sicker arc contaminant in Figures 2.4d–f have lower Nd concentration than expected from the AFC model. Five of these samples are mafic/ultramafic cumulates and low Nd concentration is expected for such rocks. Although the precise reason that the remaining three samples (two granodiorites, one monzodiorite) have low Nd concentrations is unclear, it is possible that those magmas had accumulated early-formed phases with low Nd concentration.

On the basis of my AFC models I argue that Bonanza arc magmas have undergone minimal assimilation (contaminant-melt ratio < 0.10) of Devonian Sicker arc material. Assimilation of Karmutsen Formation rocks by Bonanza arc magmas would not be detectable by the Rb-Sr and Sm-Nd isotopic systems due to the similarity in isotopic ratios between these suites (Figure 2.4). However the similarity of the major and trace element geochemistry, Nd and Sr isotopic ratios between the Bonanza arc and the

uncontaminated Talkeetna arc (Figures 2.2, 2.3 and 2.4), emplaced directly on the oceanic lithosphere (DeBari and Sleep, 1991), suggests that contamination by any pre-existing material, including the Karmutsen Formation, must have been minimal.

2.6.2 Amphibole or garnet fractionation?

The Bonanza arc was active for ~40 Myr (Figure 2.1b), during which time the arc may have thickened and the pressure of magmatic differentiation could have increased to above 0.8 GPa (24 km), where garnet becomes a stable liquidus phase in hydrous basaltic systems relevant for arc magmas (Müntener and Ulmer, 2006). Garnet strongly partitions the HREE (Table 2.3) and fractionation of large proportions of garnet will result in decreasing concentration of these elements in the remaining liquid as magma evolution progresses. Accordingly, Jagoutz (2010) ascribed Yb depletion in felsic rocks from arcs > 24 km thick to garnet fractionation in the lower crust of those arcs.

I observe two sample populations on the basis of Yb and SiO_2 concentrations in the Bonanza arc rocks (Figure 2.5): one population increases in Yb concentration with increasing SiO_2, whereas the other has low Yb concentration at high SiO_2 content, here referred to as the 'normal Yb' and 'low Yb' groups, respectively. These Yb groups are most evident in the intrusive rock suite and less clearly observed in the Bonanza volcanic suite which have generally $SiO_2 < 60$wt.% (Figure 2.5). The range of Yb and SiO_2 variation in the Talkeetna and Kohistan arcs (Figure 2.5; Kelemen *et al.*, 2014; Jagoutz and Schmidt, 2012) show a positive correlation of Yb with SiO_2 that changes to a negative correlation at $SiO_2 > 65$ wt.%. The Talkeetna and Kohistan arc sections include garnet-bearing cumulate rocks (DeBari and Coleman 1989; Hacker *et al.*, 2008; Jagoutz *et al.*, 2007) corroborating the assertion made by Jagoutz (2010) that rocks with low Yb

Mineral (abbreviation)	Liquid composition	D_{La}	D_{Dy}	D_{Yb}	D_{Dy}/D_{Yb}	reference
olivine (ol)	basalt	0.0001	0.00205	0.05	0.04	1
hornblende (hbl)	basalt	0.1675	1.055	0.6833	1.54	2
	andesite	0.12	1.77	1.15	1.54	3
plagioclase (pl)	basalt	0.04215	0.004529	0.003085	1.47	4
	andesite	0.1472	0.03076	0.01834	1.68	5
orthopyroxene (opx)	basalt	0.000791	0.02837	0.08368	0.34	6
	andesite	0.007424	0.07980	0.21708	0.37	7
clinopyroxene (cpx)	basalt	0.016	0.21	0.23	0.91	8
	andesite	0.40	1.15	0.90	1.28	9
garnet (gt)	basalt	0.0034	1.43	3.55	0.40	8
	andesite	0.07	9.50	23.5	0.40	10
titanite (tt)	andesite	2.76	24.72	10.05	2.46	11
apatite (ap)	andesite	11.40	12.00	5.95	2.02	12

References:

1 - Adam and Green (2006) - run 77; D_{Dy} interpolated from D_{Tb} and D_{Ho}

2 - Tiepolo et al. (2007) - average of #12, 42, 53, 60

3 - Tiepolo et al. (2007) - #45

4 - Bédard (2007) - SiO_2 = 45 wt.%, T = 1000C

5 - Bédard (2007) - SiO_2 = 61 wt.%, T = 1000C

6 - Bédard (2006) - MgO = 13 wt.%

7 - Bédard (2006) - MgO = 3.5 wt.%

8 - Suzuki et al. (2012) - run S1678

9 - Nicholls and Harris (1980) - runs 4448, 4510, 4511, 4512; D_{Dy} interpolated from D_{Sm} and D_{Ho}

10 - D_{La} from Irving and Frey (1978) - "Breziny"; D_{Dy} and D_{Yb} from Nicholls and Harris (1980) - run 4253

11 - Prowatke and Klemme (2006) - run ASI250; D_{Dy} and D_{Yb} determined by interpolation

12 - Prowatke and Klemme (2005) - run 61B; D_{Dy} and D_{Yb} determined by interpolation

Table 2.3: Mineral-liquid partition coefficients used in models

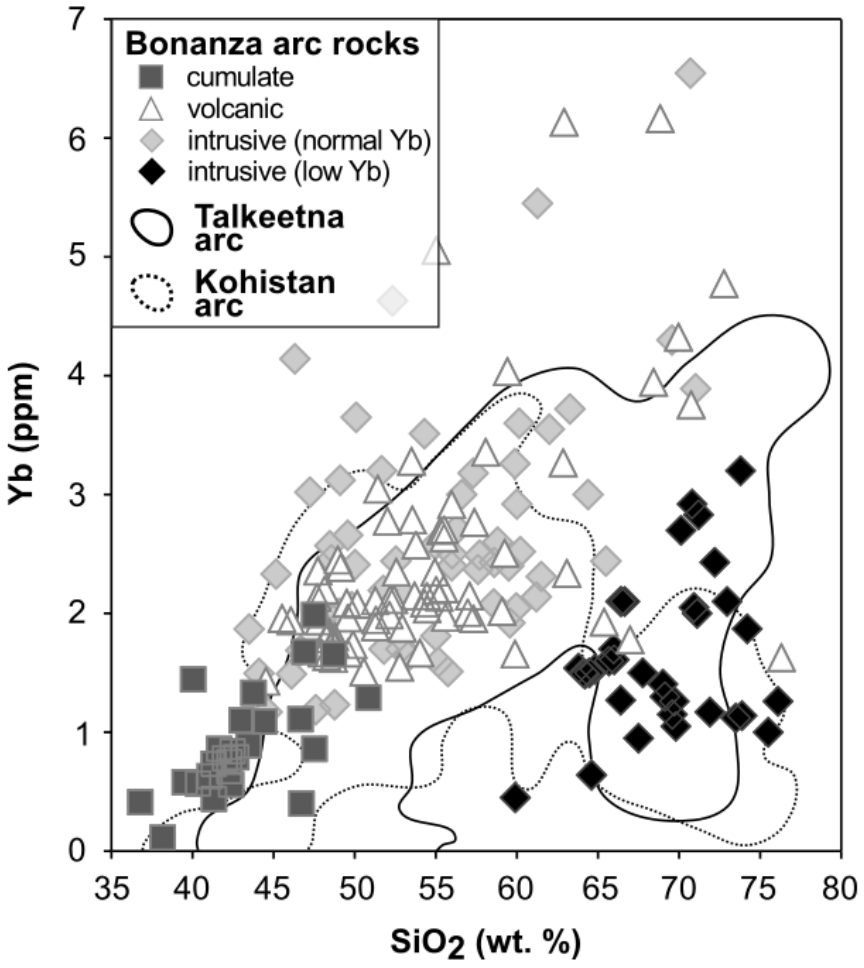

Figure 2.5: Ytterbium concentration as a function of SiO_2 in the Bonanza arc rocks. On the basis of this plot, the intrusive suite is divided into 'low Yb' and 'normal Yb' groups. Also shown are fields for the Talkeetna and Kohistan arc data (Kelemen *et al.*, 2014; Jagoutz and Schmidt, 2012).

and high SiO_2 record the effect of fractionating garnet during magma evolution. Thus, it is possible that felsic arc rocks with low Yb can be used to infer garnet fractionation and a minimum arc thickness of 24 km. No garnet-bearing cumulate rocks have been reported from the Bonanza arc, however amphibole is a commonly observed cumulate phase and is implicated in the evolution of the Bonanza arc magmas (Larocque and Canil, 2010).

Ytterbium partitions into amphibole increasingly strongly (i.e. D_{Yb} increases) as a liquid evolves to higher SiO_2 content (Figure 2.6), implying that amphibole fractionation alone can conceivably produce low to intermediate silica liquids enriched in Yb and in felsic liquids depleted in Yb. In order to determine whether amphibole or garnet fractionation is responsible for the 'low Yb' Bonanza arc rocks, I examine Dy and Yb variation as these elements partition differently depending on whether amphibole or garnet is fractionating. In basaltic to andesitic liquids, D_{Yb} for garnet varies from 3.55 to 23.5 and D_{Yb} for hornblende varies from 0.68 to 1.15 (Table 2.3). Over the same range of liquid compositions, D_{Dy} for garnet changes from 1.43 to 9.50 and D_{Dy} for amphibole increases from 1.06 to 1.77. Regardless of liquid composition, D_{Dy}/D_{Yb} is 0.40 for garnet and 1.54 for amphibole (Figure 2.6).

Dysprosium is strongly positively correlated with Yb in the Bonanza arc rocks (Figure 2.7a). The volcanic rocks and the 'normal Yb' intrusive rocks lie along regression lines with slopes of ~1.6 and the 'low Yb' intrusive rocks lie on a shallower slope of 1.45 (Figure 2.7a). The similarity in Dy/Yb slope of the Bonanza arc sample array to the D_{Dy}/D_{Yb} of amphibole (~1.5) implies that amphibole strongly controlled Dy and Yb variation in these rocks. The small differences between the slopes and amphibole D_{Dy}/D_{Yb} likely indicate the effect of co-crystallizing phases – for example olivine (D_{Dy}/D_{Yb} = 0.04;

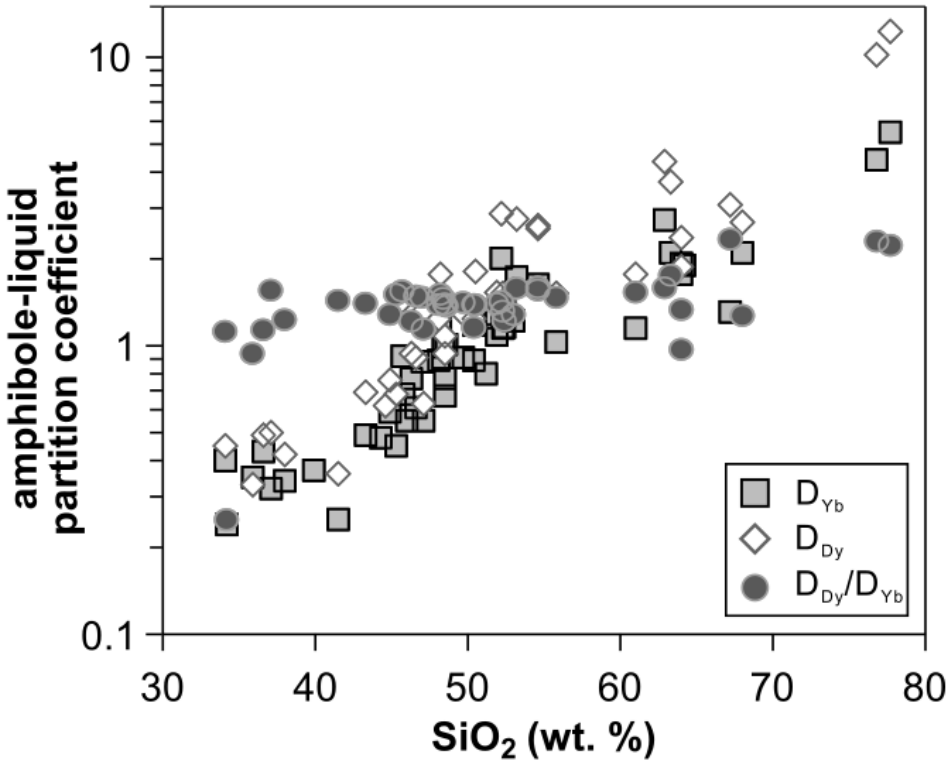

Figure 2.6: Amphibole-liquid partition coefficients for Dy and Yb (D_{Dy}, D_{Yb}) and D_{Dy}/D_{Yb} as a function of SiO_2 in the liquid. Data from Tiepolo *et al.*, (2007).

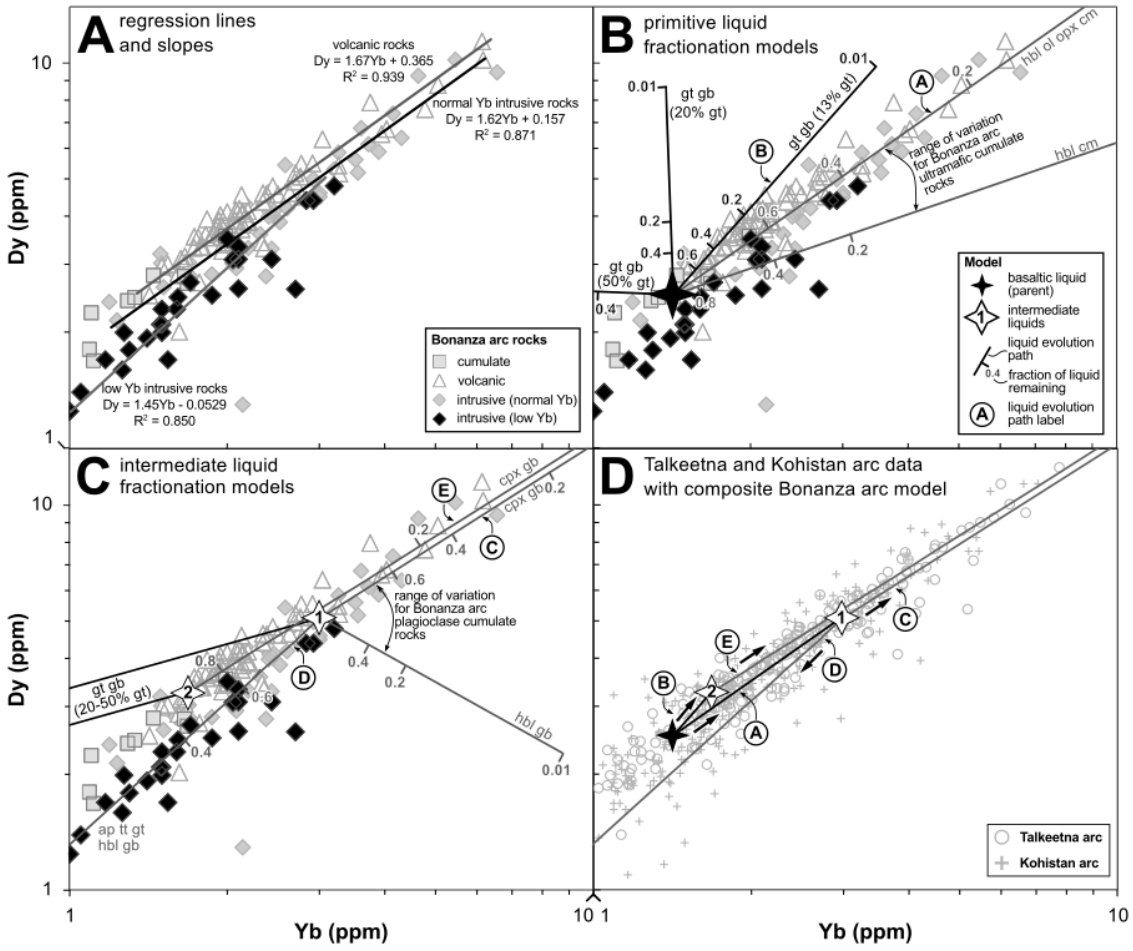

Figure 2.7: Dy and Yb variation in the Bonanza arc rocks. a) Regression lines and their equations fitted through the volcanic, 'normal Yb' and 'low Yb' intrusive rock groups. b) Liquid evolution models for fractionation of different mineral assemblages from a basaltic parent melt. c) Liquid evolution models for fractionation of different mineral assemblages from an intermediate liquid. At low degrees of fractionation, there is little to no separation between the liquids of garnet gabbros with 20 – 50% garnet. d) Data for the Talkeetna and Kohistan arcs (Kelemen *et al.*, 2014; Jagoutz and Schmidt, 2012) and a composite of liquid evolution paths A – E from panels b and c, with arrows to indicate direction of liquid evolution. Partition coefficients used in the models are provided in Table 2.3 and phase proportions for each assemblage and the compositions of the parent liquid and two intermediate liquids are provided in Table 2.4. Legend is split across panels a, b and d. Abbreviations: ap = apatite, cm = cumulate, cpx = clinopyroxene, gb = gabbro, gt = garnet, hbl = hornblende, ol = olivine, opx = orthopyroxene, tt = titanite.

Adam and Green, 2006), orthopyroxene (D_{Dy}/D_{Yb} = 0.3; Bédard, 2006) and garnet (D_{Dy}/D_{Yb} = 0.4).

To quantitatively determine the cause of the observed Dy and Yb variation, I have modelled the Rayleigh fractionation of amphibole- and garnet-bearing assemblages from a primitive parent liquid (Figure 2.7b), followed by fractionation of gabbroic assemblages from intermediate liquids (Figure 2.7c). I assume a parent liquid composition (Table 2.4) similar to a primitive basalt sample from the Bonanza arc (sample JL06-027, Mg# = 0.67; Table 2.2; Larocque, 2008). Partition coefficients and cumulate phase proportions appropriate for basaltic and andesitic liquids are provided in Tables 2.3 and 2.4. I selected the most suitable experimentally determined values of D_{Dy} and D_{Yb} for clinopyroxene, garnet and olivine from the literature and parameterizations of D for plagioclase, orthopyroxene, titanite and apatite (Bédard, 2006; 2007; Prowatke and Klemme, 2006, 2007). As no suitable experimental determinations were available for D_{La} in garnet in andesitic liquids I used a phenocryst-matrix determination (Irving and Frey, 1978). The modes of the amphibole-bearing cumulate assemblages used in the models (Table 2.4) are based on those observed in Bonanza arc cumulate rocks (Larocque and Canil, 2010). Modes for the garnet-bearing cumulate assemblage are based on mass balance calculations using silica variation diagrams for CaO and Al_2O_3 for the Bonanza arc rocks (i.e. ~13% garnet; Figure 2.2) and similar assemblages from the Talkeetna and Kohistan arcs (20 – 50 % garnet; DeBari and Coleman, 1989; Jagoutz, 2010).

The variation in Dy and Yb concentration of the ‘normal Yb’ intrusive rocks is best fit by removal of a hornblende-olivine orthopyroxenite assemblage (Path A on Figure 2.7b) from the parent basalt. Fractionation of a garnet gabbro with 13% garnet from the parent

Liquid composition	Composition (ppm)			Notes
	La	Dy	Yb	
Basaltic liquid (parent)	4.01	2.50	1.42	Sample JL06-027 (Larocque, 2008), analysis in provided in Table 2
Intermediate liquid 1	9.69	5.09	3.00	liquid at F = 0.4 from removal of hbl opx cumulate from parent
Intermediate liquid 2	9.21	3.28	1.70	liquid at F = 0.4 from removal of gt gb (13% gt) from parent

Phase proportions in fractionating assemblages*									
Name	Liquid composition	ol	hbl	pl	opx	cpx	gt	tt	ap
hbl cumulate	basalt	13%	73%		11%				
hbl ol opx cumulate	basalt	21%	20%	10%	45%				
gt gabbro (13% gt)	basalt		47%	30%		10%	13%		
gt gabbro (20% gt)	basalt/andesite		40%	30%		10%	20%		
gt gabbro (50% gt)	basalt/andesite		20%	20%		10%	50%		
cpx gabbro	andesite			50%	10%	38%			
hbl gabbro	andesite		64%	30%		3%			
hbl gabbro + 10% ap	andesite		54%	30%		3%			10%
hbl gabbro + 10% tt	andesite		54%	30%		3%		10%	
ap tt gt hbl gabbro	andesite		50%	40%		5%	3%	1%	1%
*proportion of oxide minerals not included									

Table 2.4: Parameters used in modelling calculations

basalt produces a liquid with increasing Yb and Dy (Path B on Figure 2.7b) that fits the variation of the Bonanza arc volcanic rocks at low degrees of fractionation (i.e. fraction of liquid remaining, F > 0.4). Removal of garnet gabbros similar to those observed in the Talkeetna and Kohistan arcs (20 – 50% garnet) produces liquids that evolve to higher Dy and lower Yb on paths that are subhorziontal to subvertical.

To account for shifts in element partitioning with changing liquid composition, I have modelled a second fractionation stage involving the removal of plagioclase- and garnet-bearing cumulate assemblages from intermediate liquids on Paths A and B (Table 2.4, Figure 2.7c). Plagioclase cumulate assemblages are based on observed modes in similar rocks from the Bonanza arc, whereas garnet gabbros have similar modal mineralogies as in the primitive liquid models. Mass balance calculations suggest around 1% each of titanite and apatite are responsible for the inflections in the TiO_2 and P_2O_5 silica variation diagrams (Figure 2.2). These trace phases are important because their high D_{REE} can substantially impact the trace element budget of a liquid: $D_{Dy} = 25$ and $D_{Yb} = 10$ for titanite; $D_{Dy} = 12$ and $D_{Yb} = 6$ for apatite (Prowatke and Klemme, 2005, 2006). Although fractionation of magnetite and/or ilmenite is another possible cause for the inflection in the TiO_2–SiO_2 variation diagram (Figure 2.2), I do not consider Fe-Ti oxides in my models as they are of low abundance in the Bonanza arc rocks (< 3%; Larocque and Canil, 2010) and, given the very low D_{REE} of these oxides (Nielsen *et al.*, 1992), have negligible effect on Dy and Yb concentrations in the fractionating assemblages I consider.

The intermediate liquid composition used to model the further evolution of the Bonanza arc intrusive rocks (‘Intermediate liquid 1’, Table 2.4, Figure 2.7c) is similar to

the liquid produced at 60% fractionation of a hornblende-olivine orthopyroxenite from the basaltic parental liquid (F = 0.4 on Path A, Figure 2.7b). The range of Dy and Yb in the 'normal Yb' intrusions is modelled well as the liquid produced by removal of a clinopyroxene-rich gabbro (Table 2.4) from 'Intermediate Liquid 1' (Path C, Figure 2.7c). Removal of an apatite-titanite-garnet-hornblende gabbro assemblage (Table 2.4) from 'Intermediate Liquid 1' produces liquids similar in composition to the 'low Yb' samples (Path D on Figure 2.7c). The Bonanza arc volcanic rock compositions are described by the removal of a gabbro with 13% garnet from a basaltic parent liquid (Path B, Figure 2.7b) followed, at F = 0.4 ('Intermediate liquid 2', Table 2.4), by removal of a clinopyroxene-rich gabbro from the resulting intermediate liquid (Path E, Figure 2.7c). Removal of garnet gabbro with 20 – 50% garnet from Intermediate Liquids 1 and 2 (Figure 2.7c) causes the resulting liquids to evolve to lower Yb and Dy along shallow positive slopes that do not describe the composition of the 'low Yb' intrusive rocks.

With consideration of La, the volcanic rocks and the intrusive rocks show strikingly different trends (Figure 2.8a, b) compared to their subparallel trends in Figure 2.7. Originating from a cluster centered around $(Dy/Yb)_N = 1.2$ and $(La/Dy)_N = 1.7$, the intrusive rocks describe a negative trend to high $(Dy/Yb)_N$, whereas the volcanic rocks form a positive trend to high $(Dy/Yb)_N$. The results of models incorporating La, extremely incompatible in garnet ($D_{La} = 0.0034 – 0.07$) and only moderately incompatible in amphibole ($D_{La} = 0.12 – 0.1675$; Table 2.4) are shown in Figure 2.8. The distribution of the 'normal Yb' and 'low Yb' intrusive suites in Figure 2.8a is generally described by the fractionation trends produced by removal of a hornblende-olivine orthopyroxenite from the parent basaltic liquid followed by removal of apatite-titanite-garnet-hornblende

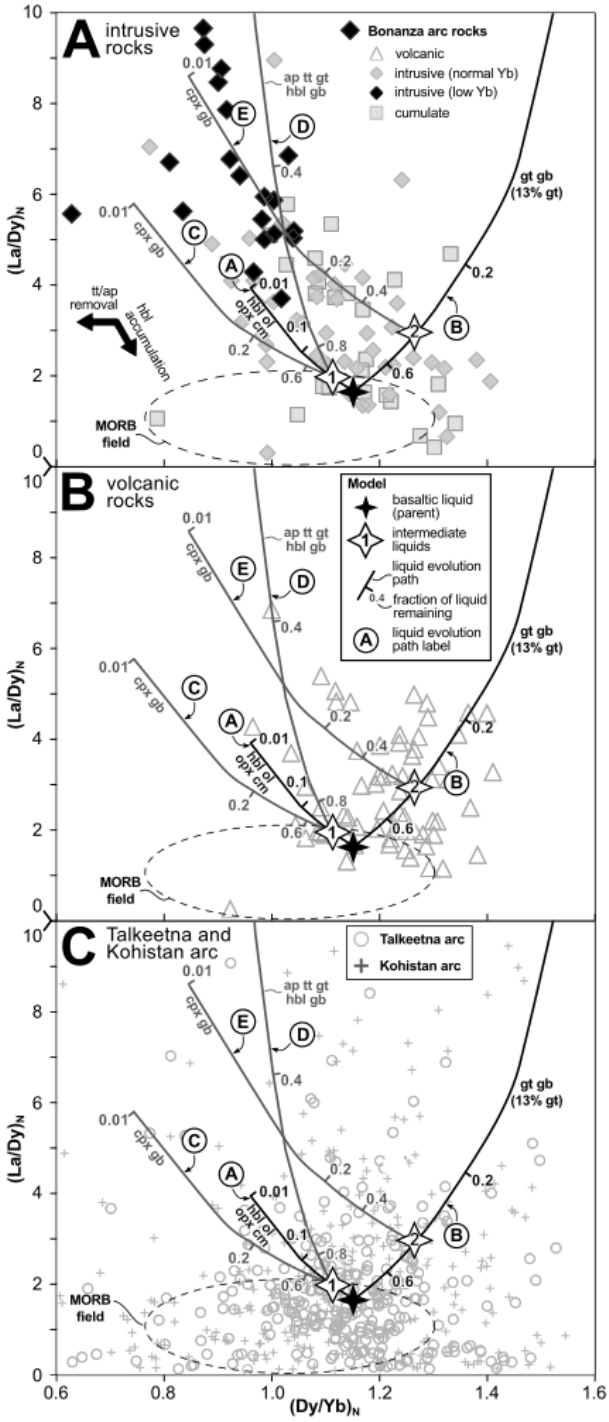

Figure 2.8: Chondrite-normalized (McDonough and Sun, 1995) La/Dy and Dy/Yb variation of the Bonanza arc rocks for a) the intrusive rocks, b) the volcanic rocks and c) the Talkeetna and Kohistan arc rocks (Kelemen *et al.*, 2014; Jagoutz and Schmidt, 2012). The results of selected fractionation models are shown. Abbreviations as per Figure 2.7.

gabbro (Path A and D, Figure 2.8a) from ‘Intermediate liquid 1’ (Table 2.4), as was discussed above in relation to Figure 2.7b and c. The removal of a clinopyroxene-rich gabbro from ‘Intermediate Liquid 1’ produces liquids that are slightly lower in $(Dy/Yb)_N$ than the main array formed by the intrusive suite (Path C, Figure 2.8a). Although some of the low $(Dy/Yb)_N$ volcanic rocks are fit by the same models as the intrusive rocks (Figure 2.8b), the high $(Dy/Yb)_N$ ratios of other volcanic samples necessitates a different fractionating assemblage. I find that removal of a garnet gabbro assemblage with 13% garnet from a basaltic parent liquid followed by removal of a clinopyroxene gabbro assemblage from ‘Intermediate liquid 2’ (Table 2.4; Paths B and E, Figure 2.8) describes the distribution of the majority of the Bonanza arc volcanic data in Figure 2.8b.

Although their La, Dy and Yb variation require garnet fractionation, the Bonanza arc volcanic rocks do not show the Yb depletion at high SiO_2 (Figure 2.5) associated with garnet fractionation (e.g. Jagoutz, 2010). I argue that this is due to the relatively small proportion of garnet (1 – 13%) that is removed, combined with the low partition coefficients for Yb in the other fractionating phases (plagioclase, clinopyroxene and amphibole; Table 2.3), resulting in a low bulk partition coefficient of Yb in the fractionating assemblage.

The models I present indicate that fractionation of hornblende-olivine orthopyroxenite from a primitive liquid followed by the fractionation of clinopyroxene gabbro and apatite-titanite-garnet-hornblende gabbro from a resulting intermediate liquid (Paths A, C and D in Figure 2.7 and 2.8) can reproduce the La, Dy and Yb variation of the Bonanza arc intrusive rocks, including the felsic ‘low Yb’ intrusive suite. The volcanic rocks of the Bonanza arc indicate fractionation of ~13% garnet from a primitive liquid followed by

fractionation of clinopyroxene gabbro from an intermediate liquid (Paths B and E in Figure 2.7 and 2.8). The poor fit between the models and the data in Figure 2.8 may be due to several simplifications inherent in modelling magma evolution as a pure liquid produced by only two discrete stages of Rayleigh fractional crystallization. For example, amphibole accumulation observed in some Bonanza arc volcanic rocks (Nixon *et al.*, 2011a, b) implies that they are not pure liquids. Such accumulation moves the whole rock composition to lower $(La/Dy)_N$ but higher $(Dy/Yb)_N$, shown schematically on Figure 2.8a, due to the higher D_{Dy} compared to D_{La} and D_{Yb} of amphibole (Table 2.3). Futhermore, the high D_{Dy} and D_{Yb} of apatite and titanite (Table 2.3) mean that small variations in the amount of these minerals in the fractionating assemblage can affect the liquid composition considerably. For example, increasing the amount of titanite or apatite fractionating would shift the liquid evolutions lines to lower $(Dy/Yb)_N$ while only slightly increasing $(La/Yb)_N$, as shown schematically in Figure 2.8a.

The imperfect fit between the models and data could also be due to the choice of partition coefficients, although I attempted to minimize this effect by using comprehensive parameterizations and suitable experimental determinations of this parameter. The continuous change in liquid composition during evolution means that no single value for partition coefficient can perfectly model the evolution of liquid composition and some mismatch between predictions and observations is inevitable. The distribution of Bonanza arc rock analyses in Figures 2.7 and 2.8 could also be produced by fractionation of similar assemblages from different parent liquid compositions. The likely range of starting compositions are shown on Figure 2.8, similar to MORB (Jenner and O'Neill, 2012).

Another process by which low Yb, high SiO_2 rocks may be formed is partial melting of amphibolite to leave a garnet-bearing residue at the base of the crust (Zhang *et al.*, 2013). This process presupposes a crust that is thick enough that garnet is stable (> 24 km depth; Müntener and Ulmer, 2006; Zhang *et al.*, 2013) and is consistent with my assertion that the Bonanza arc was thick enough to allow garnet to be a stable phase in the lower crust.

2.6.2.1 Alternate modelling approaches

Other approaches are able to overcome the aforementioned shortcomings of modelling using partition coefficients. For example, subtractive modelling, based on the incremental removal of chemical compositions of observed cumulate rocks from that of a parental liquid causing the remaining liquid to evolve away from the cumulate composition, was used to determine the petrogenesis of the Kohistan arc (Jagoutz, 2010). Larocque and Canil (2010) also used a subtractive model to describe the major element composition of the Bonanza arc rocks in terms of the removal of olivine, amphibole and/or clinopyroxene from a primitive parental liquid.

Using the method described by Jagoutz (2010), I modelled the removal of an olivine-bearing cumulate assemblage followed by the removal of a plagioclase-bearing assemblage, each modelled as the average of similar assemblages observed in the Bonanza arc, from the same basaltic parent liquid used in the above models (sample JL06-027; Larocque, 2008). This model (Figure 2.9) predicts the increasing Yb concentrations of the Bonanza arc rocks up to 60 – 65 wt.% SiO_2. However, the compositions of observed cumulate rocks in the Bonanza arc are insufficient to reproduce the 'low Yb' samples (Figure 2.9). A cumulate rock composition with high Yb and low SiO_2 is required, but no such cumulate rocks are observed in the Bonanza arc suite.

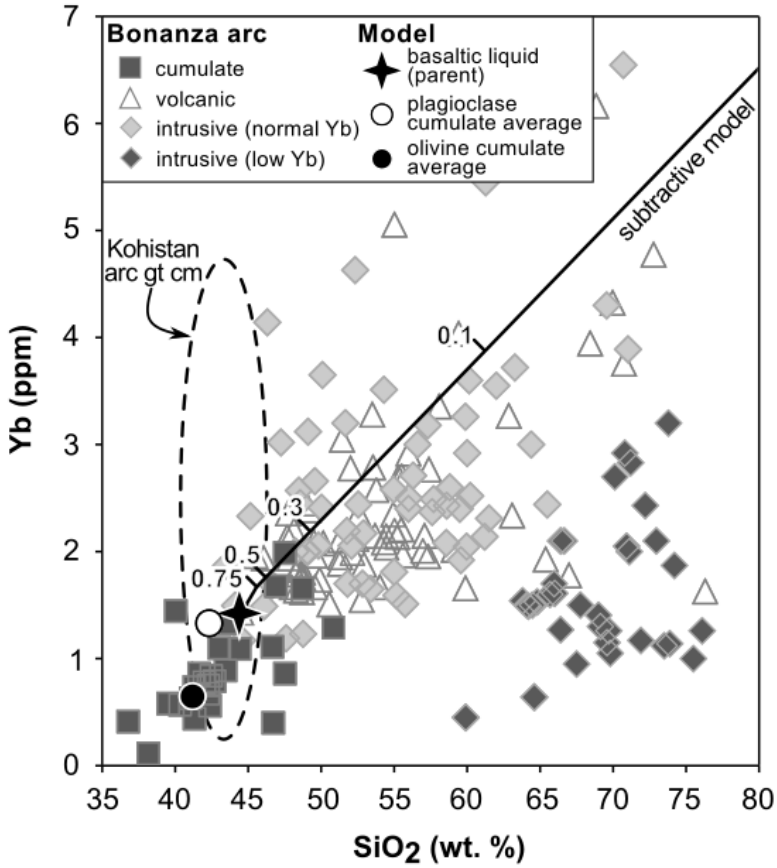

Figure 2.9: Plot showing the subtractive fractionation model of the Yb-SiO_2 variation in a liquid produced by removal of 25% of the average Bonanza arc olivine cumulate rock (Yb = 0.6 ppm, SiO_2 = 41.2 wt.%) followed by removal of the average primitive Bonanza arc plagioclase cumulate (Yb = 1.3 ppm, SiO_2 = 43.2 wt.%). The range of compositions of garnet-bearing mafic rocks from the Kohistan arc (Jagoutz and Schmidt, 2012) is also shown. Abbreviations as per Figure 2.7.

A cumulate assemblage containing garnet, hornblende and trace phases like titanite and apatite would have high Yb and relatively low SiO_2 concentration, potentially similar to the garnet-bearing ultramafic rocks of the Kohistan arc (Figure 2.9; Jagoutz and Schmidt, 2012). Fractionation of such an assemblage from the modelled liquid would efficiently drive the remaining liquid to low Yb and high SiO_2 compositions, similar to the spread of data in Figure 2.9. The requisite garnet-bearing assemblages are not observed in the Bonanza arc, but are similar to those used in REE models presented above (Figure 2.7 and 2.8). The absence of a garnet-bearing cumulate assemblage in the Bonanza arc section may be due to its high density compared with the sub-arc mantle, resulting in the foundering of these rocks (Kay and Mahlburg-Kay, 1991; Jagoutz and Schmidt, 2012).

2.6.2.2 Comparison to other arcs

The chemical composition of Bonanza arc rocks overlaps that of rocks from the Talkeetna and Kohistan arcs in major element concentration (Figure 2.2) and trace element abundance (Figure 2.3). The Talkeetna and Kohistan arc data show much greater range and scatter in $(La/Dy)_N$ and $(Dy/Yb)_N$ than do the Bonanza arc data (Figure 2.8c). I have not attempted to fit my models to the Talkeetna and Kohistan arc data but the data for those arcs are not incompatible with my models (Figures 2.7d, 2.8c). Although not shown here, the hornblende gabbro fractionation model that Jagoutz (2010) presents for the Kohistan arc is similar in trajectory to my hornblende olivine orthopyroxenite model (Path A; Figure 2.7, 2.8). Similar to my conculsions, Jagoutz (2010) also noted the importance of a garnet-bearing fractionating assemblage in the petrogenesis of low Yb Kohistan arc granitoids, however no data were available to compare that garnet fractionation model to ours. The array of very low $(La/Dy)_N$ samples, with variable

$(Dy/Yb)_N$, from the Talkeetna and Kohistan arc (Figure 2.8c) has no equivalent in the Bonanza arc and likely represents the garnet-bearing cumulate rocks known from the former arcs (DeBari and Coleman, 1989; Jagoutz, 2010) but not in the Bonanza arc. The inference of garnet-bearing cumulate rocks in the petrogenesis of the Bonanza arc is significant as it provides a previously unknown similarity with the coeval Talkeetna arc (DeBari *et al.*, 1999).

2.6.3 Constraints on the thickness of the Bonanza arc

My fractionation models imply that garnet was a fractionating phase in the Bonanza arc and implies that the lower crust extended to depths at which garnet was stable. The crust on which the Bonanza arc was emplaced consists of at least 3 km of Devonian Sicker arc rocks (Muller *et al.* 1977) overlain by 6 km of Triassic Karmutsen basalts, inferred to have an equally thick gabbroic complement, possibly residing in the lower crust of Wrangellia (Greene *et al.*, 2009). Thus, the total thickness of the substrate on which the Bonanza arc formed was at least 15 km. The true thickness of the pre-Bonanza arc crust is likely to be greater than 15 km, a value that is calculated on the basis of suface exposures only, thus providing a 'worst case' total thickness in the calculations that follow. Because garnet is only stable at greater than 24 km depth (i.e. 0.8 GPa; Müntener and Ulmer, 2006), the possibility of garnet fractionation in controlling the evolution of the Bonanza arc magmas as modelled above depends critically on whether the combined thickness of the Bonanza arc and the pre-Jurassic crust reached or exceeded this thickness over the period in which the Bonanza arc was active.

A previous estimate of the total thickness of the Bonanza arc and its substrate of ~ 24 km was based primarily on hornblende thermobarometry of felsic intrusive rocks and less

so on barometry of the mafic and ultramafic plutonic rocks in the Bonanza arc section (Canil *et al.*, 2010). Here I attempt to make simple, first-order estimates of the total thickness of the Bonanza arc and pre-Jurassic crust using constraints from geological mapping combined with amphibole thermobarometry. Figure 2.10 shows the widths of all the Bonanza arc units along a line perpendicular to the NW-SE strike of the Bonanza arc on Saanich Peninsula, southern Vancouver Island. This region was chosen for this exercise because it is relatively free of faulting that might otherwise distort the thicknesses of these units (Figures 2.1, 2.10). Using Al-in-hornblende geobarometry, Canil *et al.* (2010) determined that the Island Plutonic Suite was 5 – 8 km thick. Assuming this thickness range is accurate, the dip required to produce the observed outcrop length of the Island Plutonic Suite exposed on Saanich Peninsula (~11 km; Figure 2.10) varies from 28 – 48°, which overlaps the range of dips for foliations (35 – 65°) of intrusive rocks observed in the field (Larocque and Canil, 2010). Assuming dips of 28 – 48° for Bonanza intrusive (i.e. the Island Plutonic Suite and the Westcoast Crystalline Complex) and volcanic units, the observed outcrop lengths (Figure 2.10) prescribe a total true thicknesses of 11 – 18.4 km for the arc. Applying an alternate amphibole barometer (Ridolfi *et al.*, 2009) to the data of Canil *et al.* (2010) gives a maximum thickness of only 3.5 km for the Island Plutonic Suite, requiring a dip of only 20° to explain the measured outcrop lengths in Figure 2.10, and resulting in an total true thickness of the Bonanza arc of only 8 km.

Using my lowest estimate of the thickness of the Bonanza arc (8 km), the minimum combined thickness of the Bonanza arc and pre-existing crust is 23 km. The base of the crust in this case is slightly shallower than the minimum required for garnet to be a stable

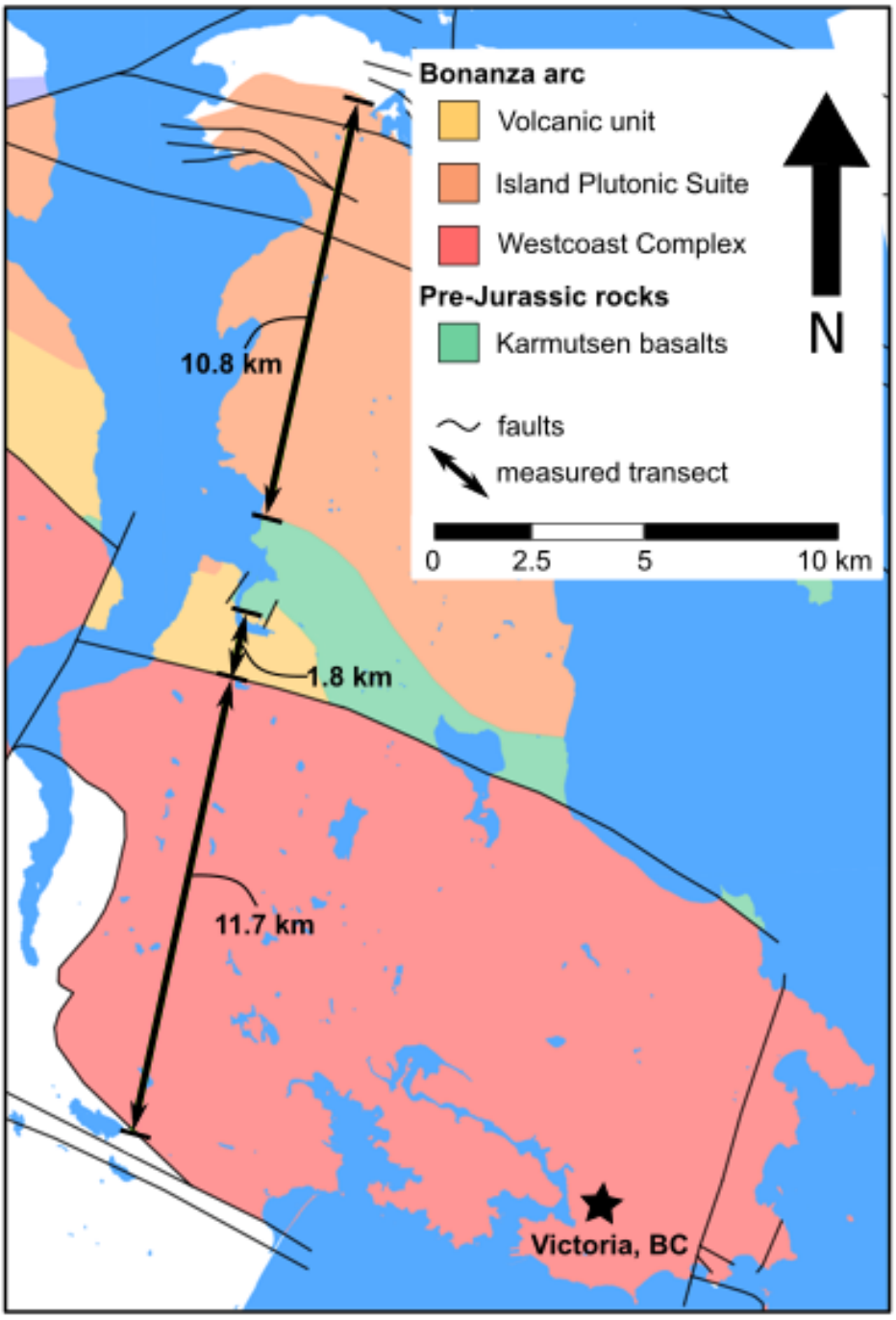

Figure 2.10: Mapped lengths of the Bonanza arc units perpendicular to the NW-SE regional strike of the Bonanaza arc, along a relatively unfaulted section on southern Vancouver Island.

liquidus phase in arc magmas (Müntener and Ulmer, 2006). My maximum likely thickness estimate for the Bonanza arc (~18 km) combined with the pre-existing crust gives a total thickness of approximately 33 kilometers and implies that the base of the crust was within the stability zone of garnet. This maximum estimate is similar to the seismically determined depth to the present-day Moho beneath Vancouver Island (35 km; Clowes *et al.*, 1987).

There are large differences in the results of the amphibole barometers used by Canil *et al.* (2010) and Ridolfi *et al.* (2009). As noted by Canil *et al.* (2010) the pressures they report for some samples are maxima due to the plagioclase composition (> An_{35}) and the absence of K-feldspar in some samples (Anderson and Smith, 1995). Ridolfi *et al.* (2009) similarly caution that errors for their pressure estimates may be as high as 25% for magnesiohorneblende and tschermakitic pargasite, the most common amphiboles in the Bonanza arc intrusive rocks (Larocque, 2008). The mismatch between these pressure estimates underscores the importance of using geobarometers that are suitable for the species of amphibole and the coexisting mineral assemblage present in a sample.

2.6.4 Timing and spatial distribution of magmatism in the Bonanza arc

The intrusive Bonanaza arc rocks, sampled from exposures across Vancouver Island, show a continuous range of ages from 163 to 200 Ma, with a peak at 172 Ma (Figure 2.1b). The distinctly bimodal volcanic age distribution may indicate that volcanism occurred as two separate pulses within one arc, at 198 and 171 Ma, with an intervening quiescent period of ~10 Myr. Another interpretation, linking the distinct spatial separation of regions exposing young and old volcanic rocks on northern Vancouver Island (Figure 2.1a), is that what is presently called the Bonanza arc was actually two

geographically separate arcs that were active within ~10 Myr of one another. In this interpretation, the two separate arcs are juxtaposed in the present day by movement along arc-parallel strike slip faults.

The intrusive rock age distribution (n = 63, peak at 172 Ma) is skewed toward younger ages, as expected from the greater preservation potential for younger rocks compared to older ones. Contrary to the expectation that older rocks are less likely to be preserved than younger ones, the volcanic rock age distribution (n = 31) shows that older ages are better represented than younger ages in my compilation (Figure 2.1b). Thus, I argue that the bimodal age distribution of the Bonanza arc volcanic rocks is not a true representation of their ages and is an artefact of intensive sampling of those rocks in a limited geographic region compared to the geographically comprehensive sampling of intrusive rocks (Figure 2.1a). I also cannot rule out preservation bias in producing the bimodal volcanic age distribution as the trace of the Holberg Fault, running through Holberg Inlet (Figure 2.1a), bisects the main region of measured volcanic ages.

The geographic distribution of the ages of Bonanza arc volcanic rocks on northern Vancouver Island is sharply divided with young (i.e. ~171 Ma) and old (i.e. ~198 Ma) ages northeast and southwest, respectively, of the trace of the Holberg Fault. The observed eastward-younging of the rocks can be produced by: 1) subduction in the west (present coordinates) of an east-dipping slab combined with forearc erosion; or 2) subduction in the east of a west-dipping slab that is 'rolling-back' (e.g. Gvitrzman and Nur, 1999). I am unable to distinguish between the possibilities of slab rollback or forearc erosion as Jurassic forearc assemblages, which would constrain subduction polarity have not been found on Vancouver Island (Canil *et al.*, 2012). On the other hand, little is

known about the timing and sense of displacement along the steeply dipping Holberg Fault (Nixon *et al.*, 2011a, b) but it may be a major strike-slip structure that juxtaposed younger and older arc segments, thus increasing the width of the present exposure of the Bonanza arc. A test of that idea, and how the Holberg Fault links with other major structures that dissect the Bonanza arc, (Figure 2.1) requires further investigation.

2.7 Conclusions

I have determined that < 10% assimilation of only pre-exisiting rocks from the Sicker arc is required to explain the variations observed in Sr and Nd isotopes in rocks of the Bonanza arc. Although comparisons of Bonanza arc geochemistry with that of the uncontaminated Talkeetna arc are favourable, I am unable to conclusively rule out contamination of the former by the isotopically similar Karmutsen Formation. The intrusive rocks of the Bonanza arc have high $(La/Dy)_N$ and low $(Dy/Yb)_N$, whereas both ratios are high in the volcanic rocks. Thus, two separate fractionation models are required to predict the REE chemistry of the Bonanza arc rocks: one model (garnet gabbro fractionation followed by clinopyroxene gabbro fractionation) describes the chemistry of the majority of volcanic rocks and some intrusive rocks; another model (hornblende-olivine orthopyroxenite fractionation, followed by apatite-titanite-garnet-hornblende gabbro fractionation) describes the chemistry of the majority of intrusive rocks and some volcanic rocks. Both lineages implicate garnet as a fractionating phase, which is significant as garnet-bearing cumulate rocks have not been described in the Bonanza arc and are a previously unknown similarity with the coeval Talkeetna arc. My estimates for the thickness of the Bonanza arc and the pre-existing crust indicate that the base of the crust was likely deeper than the 24 km (0.8 GPa) minimum limit for garnet stability,

thereby supporting the garnet fractionation models I have presented. Garnet-bearing rocks are not described in the Bonanza arc and may have been lost by foundering into the comparatively buoyant underlying mantle (e.g. Kay and Mahlburg-Kay, 1991) or that these rocks are simply beneath the present day depth of erosion.

The Bonanza arc volcanic rocks show a bimodal age distribution likely due to sampling bias and show an abrupt change to younger ages to the north of the Holberg Fault, on northern Vancouver Island. This spatial distribution is either due to movement of the magmatic front with time by fore-arc erosion or slab rollback during subduction, or the juxtaposition of separate arcs by strike-slip motion on the Holberg Fault. My geochronological compilation indicates that the Bonanza arc was active from 203 to 164 Ma during which time the arc may have thickened enough that the composition of later magmas was affected by garnet fractionation whereas earlier magmas were not. The conclusive test of such spatio-temporal magmatic evolution depends critically on the comparison of geochemical and geochronological data, however the number of samples for which both data are presently available is too meager to draw such conclusions. Expanding this dataset could provide unique insights into the evolution of a thickening arc and presents a potentially fruitful avenue for future work.

Chapter 3.
Effect of alkalinity on S solubility in basaltic andesite melts at 1270ºC and 1 GPa.

3.1 Abstract

I have tested the role of alkalis on S Concentration at Sulfide Saturation (SCSS) measured in hydrous basaltic andesite melts at 1270ºC and 1 GPa using piston-cylinder apparatus. At an oxygen fugacity approximately two log units below the fayalite magnetite quartz buffer, I find that SCSS is correlated with total alkali concentration, perhaps as a result of the increased non-bridging oxygen resulting from melt depolymerization. A possible limit to the enhancing effect of alkalis on SCSS in hydrous melts is observed at ~7.5 wt.% total alkali concentration. Using my results and published data, I have retrained earlier SCSS models and find that the updated models provide a better fit to test data. I have also developed a new empirical model using theoretical optical basicity as a compositional parameter that predicts SCSS with slightly better accuracy compared to previously published models:

$$\ln\left(SCSS_{ppm}\right) = 16.34 - \frac{5785}{T} - 339.4\frac{P}{T} + 10.85\ln\left(\Lambda\right) + 3.750\,X_{FeO} + 6.704\,X_{H_2O}$$

with temperature (T) in Kelvin, pressure (P) in GPa, the optical basicity (Λ) and mole fractions of Fe_2O_3 (calculated from Kress and Carmichael, 1991) and H_2O in the melt.

3.2 Introduction

Sulfur in melts plays an important role in the geosphere by the formation of sulfide minerals or immiscible sulfide melts (e.g. Naldrett, 1969) that partition chalcophile elements (e.g. Cu, Pb, Zn) between Earth's crust and mantle. The release of S into the atmosphere by degassing magmas is also thought to have an impact on global climate (e.g. Scaillet and Macdonald, 2006; McLinden *et al.*, 2016). Furthermore, the solution

and exsolution of S from melts is important during the formation of magmatic and hydrothermal ore deposits (Sillitoe, 2010). Sulfur is also extensively utilized in industrial processes as sulfate in glass fining and as sulfide in glass colouring (e.g. Falcone *et al.*, 2011) and is an important consideration in nuclear waste disposal (e.g. Lenoir *et al.*, 2009).

The geochemical behaviour of S in melts has a long history of study starting with Fincham and Richardson (1954) who used simple systems at 100 kPa to show that at log $f_{O2} < \sim 5.5$, S^{2-} displaces O^{2-} anions in silicate and aluminate melts by the reaction:

$$S^{2-}_{(\text{silicate melt})} + \tfrac{1}{2}O_{2\,(\text{gas})} \leftrightarrow O^{2-}_{(\text{silicate melt})} + \tfrac{1}{2}S_{2\,(\text{gas})} \quad [3.1]$$

Haughton *et al.* (1974) discovered that S Concentration at Sulfide Saturation (SCSS) is strongly correlated with Fe concentration and temperature in natural melts, described by Liu *et al.* (2007) with the reaction:

$$FeS_{(\text{sulfide})} + FeO_{(\text{silicate melt})} + O^{2-}_{(\text{silicate melt})} \leftrightarrow S^{2-}_{(\text{silicate melt})} + 2FeO_{(\text{sulfide})} \quad [3.2]$$

Several other experimental studies also show that SCSS is sensitive to temperature, pressure and melt composition (e.g. Shima and Naldrett, 1975; Danckwerth *et al.*, 1979; Wendlandt, 1982; Bradbury, 1983; Buchanan *et al.* 1983; Carroll and Rutherford, 1985, 1987, 1988; Mavrogenes and O'Neill, 1999; Holzheid and Grove, 2002; O'Neill and Mavrogenes, 2002; Clemente *et al.*, 2004; Jugo *et al.*, 2005a; Scaillet and Pichavant, 2005; Tsujimura and Kitakaze, 2005; Scaillet and Macdonald, 2006; Liu *et al.*, 2007; Jugo, 2009; Ariskin *et al.*, 2013; Fortin *et al.*, 2015). These studies have found a negative correlation of SCSS with SiO_2 and a U-shaped dependance on melt FeO content with a minimum at ~1 – 8 wt.% FeO (O'Neill and Mavrogenes, 2002; Tsujimura and Kitakaze, 2005; Wykes *et al.*, 2015). Most experiments report that SCSS is negatively correlated

with pressure, with a few notable exceptions (Mysen and Popp, 1980; Carroll and Rutherford, 1985; Luhr,1990).

Dissolution of S in silicate melts occurs by the substitution of S^{2-} for non-bridging oxygen (NBO) in the melt via reaction [3.1]. It therefore follows that increasing the proportion of network-modifying cations (Fe^{2+}, Ca^{2+}, Mg^{2+}, Na^{+} and K^{+}), thus increasing NBO/T - the amount of NBO relative to tetrahedral oxygen (T) - at constant T, P and melt FeO, will also increase the SCSS of a melt. The alkali elements Na and K form network modifying cations of particular interest as they are known to affect several physical and chemical properties of melts. For example, alkali cations decrease the viscosity of melts by reducing the degree of melt polymerization (e.g. Isard, 1969; Day, 1976) and increase the NBO/T of a melt (Isard, 1969; Mysen *et al.*, 1985) thereby increasing the solubility of S^{2-} through reaction [3.1]. The Fe^{3+}/Fe^{2+} transition is also known to occur at lower f_{O2} in alkali-rich compositions (e.g. Paul and Douglas, 1965; Gwinn and Hess, 1989; Cicconi *et al.*, 2015). Small changes in Fe^{3+}/Fe^{2+} greatly affect the S^{6+}/S^{2-} of a melt (Jenner *et al.*, 2010) due to the stoichiometry of the equilibrium between Fe^{2+} – Fe^{3+} and S^{2-} – S^{6+} redox couples in the melt:

$$SO_4^{2-} + 8Fe^{2+}O \leftrightarrow S^{2-} + 8Fe^{3+}O_{1.5} \quad [3.3]$$

Because S^{6+} is up to 100 times more soluble in a melt than S^{2-} (e.g. Carroll and Rutherford, 1985, 1987; Jugo *et al.*, 2005b), the higher Fe^{3+}/Fe^{2+} of an alkaline melt will increase SCSS by increasing S^{6+}/S^{2-}.

Alkali-rich magma series are found in all tectonic settings (e.g. Gupta, 2015). Although these rocks are a minor constituent of volcanic arcs, they are uniquely associated with porphyry Cu deposits of economic interest (e.g. Müller and Groves, 1993; Mcinnes and

Cameron, 1994; Lang *et al.*, 1995; Sillitoe, 2010; Logan and Mihalynuk, 2014), suggesting a link between alkalinity and the SCSS or transport of S and chalcophile elements. A compilation of volcanic rocks (n > 42,000; Sarbas and Nohl, 2008) from arcs worldwide reveals extensive variation in total alkali concentration (1.5 – 10 wt.%) in basaltic andesites to basaltic trachyandesites (Figure 3.1a) varying from the low-K to shoshonite series (Figure 3.1b). There are striking positive correlations of S and alkalinity in arc melt inclusions (Ducea *et al.*, 1994), with up to 0.3 wt.% S in the oxidized alkalic melt inclusions of the Roman Province (Metrich and Clocchiatti, 1996). Scaillet and Macdonald (2006) showed a strong positive correlation of SCSS with alkalinity in hydrous rhyolite melts, however no work has yet tested the effect in less evolved magmas.

The objective of the present study is to systematically study the effect of alkali concentration in basaltic andesite compositions, ultimately to assess the potential role of alkali-rich magmas in transporting S in the arc setting. Because SiO_2 is the chief network former in natural magmas and is known to strongly impact SCSS, I restricted my study to compositions with ~51 wt.% SiO_2 where there is a relative paucity of experimentation on SCSS at high alkali concentration (Figure 3.1). Similarly, I restrict my study to starting materials with intermediate FeO^{tot} (6 – 8 wt.%), near the minimum in the U-shaped dependence of SCSS on FeO (O'Neill and Mavrogenes, 2002).

3.3 Methods

3.3.1 Starting materials

I synthesized ~10 g each of five basaltic andesite (~51 wt.% SiO_2; 6 – 8 wt.% FeO^{tot}) starting materials with varying total alkali concentration (Figure 3.1, Table 3.1). The

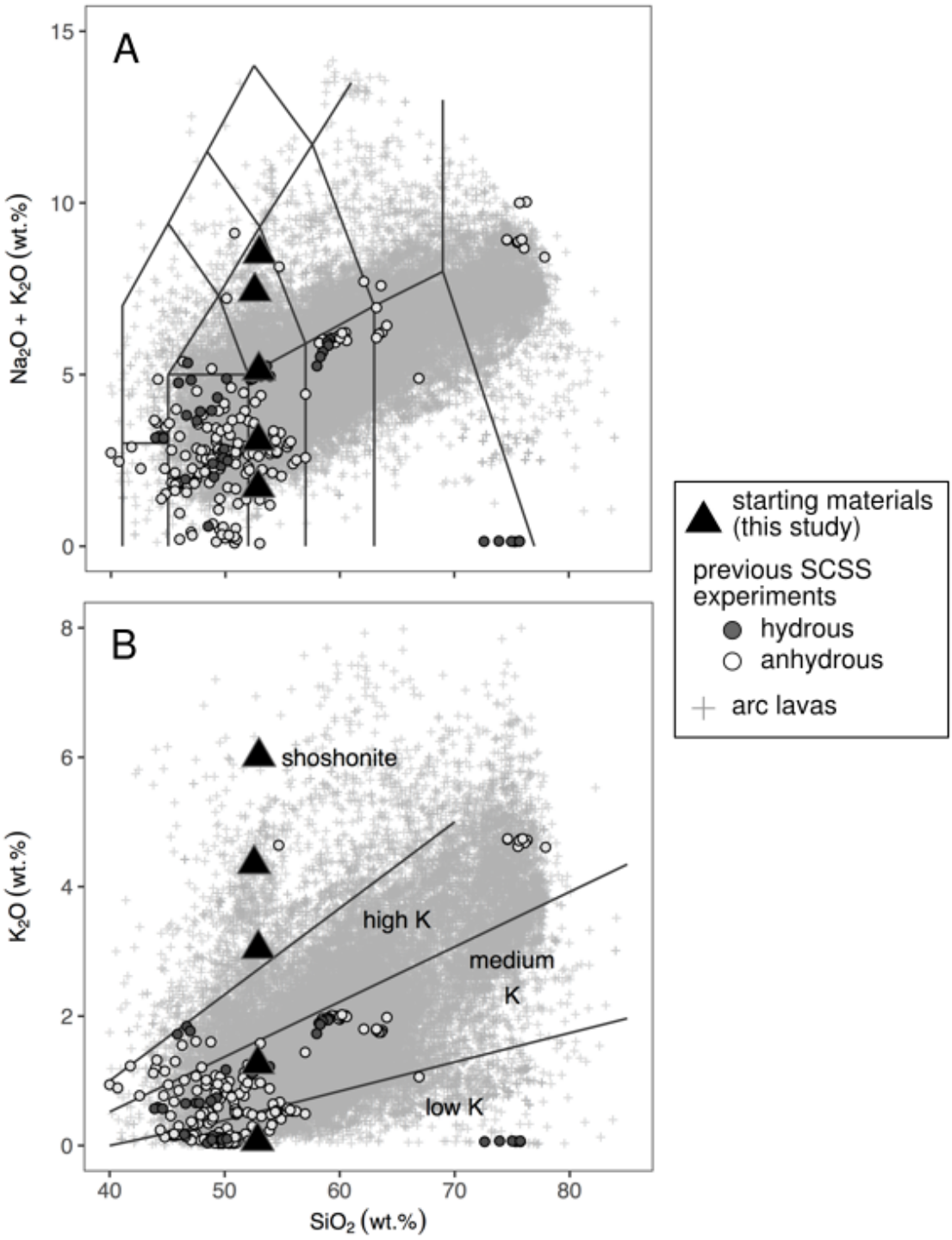

Figure 3.1: a) Total Alkali-Silica diagram (LeMaitre, 2002) and b) Potassium classification diagram (LeBas *et al.*, 1986) showing the starting materials from the present study and the distribution of SCSS experiments from the literature that I used in this study (see text for details) in the context of arc lavas from around the world. Arc data from GEOROC (http://georoc.mpch-mainz.gwdg.de/georoc/; Sarbas and Nohl, 2008).

	RD0K	RD1K*	RD3K**	RD4K	RD6K
SiO_2	51.23	51.24	51.25	51.37	51.27
TiO_2	0.51	0.61	0.77	1.03	1.02
Al_2O_3	18.73	18.23	17.47	16.22	16.20
FeO^{tot}	7.38	7.06	6.58	6.84	5.78
MgO	4.60	4.30	3.84	3.59	3.08
CaO	11.27	10.87	10.25	9.25	9.23
Na_2O	1.54	1.74	2.05	3.08	2.56
K_2O	0.00	1.23	3.08	4.11	6.15
H_2O	3.50	3.50	3.49	3.50	3.49
S	1.02	1.01	1.00	1.00	0.99

* RD1K is a 4:1 mixture (by weight) of RD0K and RD6K

** RD3K is a 1:1 mixture (by weight) of RD0K and RD6K

Table 3.1: Starting material compositions

concentration of Na_2O and K_2O in the starting materials varies from 1.5 – 3.6 wt.% and 0 – 6.2 wt.%, respectively, to capture the range of alkali concentrations in natural arc basaltic andesites (Figure 3.1). Other major element concentrations in my starting materials are similarly within the range of natural arc volcanic rocks containing ~51 wt.% SiO_2 (Table 3.1). To synthesize each starting material, reagent grade oxides (SiO_2, TiO_2, Al_2O_3, Fe_2O_3 and MgO) and carbonates ($CaCO_3$, Na_2CO_3 and K_2CO_3) were weighed out, mixed by shaking for 15 minutes, loaded into platinum crucibles, decarbonated and then fused at 1400ºC for 12 hours, quenched to a glass, extracted and ground to a powder. The glass powder was then fused for a further 12 hours and re-ground to ensure complete vitrification and homogeneity. Sodium may be volatile at 1400ºC but there appears to have been little loss of Na during these fusion steps as shown by my EPMA results (Section 3.3.3, Table 3.3). Water and S concentrations of 3.5 and 1 wt.%, respectively, were added by weighing in $Al(OH)_3$ and $FeSO_4$ to the glass powder, which also added Al and Fe to obtain the intended composition, with further grinding for 5 minutes under ethanol in an agate mortar and pestle. In addition to ensuring complete homogenization of the starting materal, addid S as $FeSO_4$ instead of sulfide ensured that any sulfide observed in the experiments were not simply unreacted sulfide from the starting material. The powders were then stored at 80ºC before use. For three experiments (marked in Table 3.2), I decreased the H_2O content in the starting material by heating for 2 hours at 400ºC to convert gibbsite ($Al(OH)_3$ – 35 wt.% H_2O) to boehmite (AlOOH – 15 wt.% H_2O) prior to loading into capsules (Zhu *et al.*, 2010).

Run #	duration (h)	starting material	phases present
P466	1	RD6K	liq, sulf
P468	1	RD0K	liq, sulf, px
P470	4	RD0K	liq, sulf
P471	4	RD0K*	liq, sulf, px
P472	4	RD6K*	liq, sulf
P474	4	RD6K	liq, sulf
P478	4	RD4K*	liq, sulf
P476	4	RD4K	liq, sulf
P479	4	RD3K	liq, sulf, Pt wire
P480	4	RD1K	liq, sulf, Pt wire

Abbreviations: liq = liquid; sulf = sulfide droplet; px = pyroxene

* dehydrated prior to capsule loading

Table 3.2: Starting materials and experiment durations used in experiments.

Run	lab	SM	t (h)	SiO_2	TiO_2	Al_2O_3	FeO^{tot}	MgO	CaO	Na_2O	K_2O	S (ppm)	Sum	difference from 100%	H_2O^{**}	Fe_2O_3/FeO^a	Λ^b
P466	UBC	RD6K	1	52.38 (0.95)	1.12 (0.03)	15.96 (0.60)	4.54 (0.15)	3.08 (0.06)	9.54 (0.20)	2.72 (0.12)	6.53 (0.15)	1225 (66)	96.02 (1.17)	3.98	2.84 (0.38)	0.046	0.581
P466	UA	RD6K	1	53.37 (0.58)	1.09 (0.04)	16.42 (0.64)	4.43 (0.11)	3.14 (0.08)	9.51 (0.12)	2.52 (0.07)	6.24 (0.07)	1214 (73)	96.85 (0.89)	3.15	2.84 (0.38)	0.044	0.578
P468	UBC	RD0K	1	54.50 (1.61)	0.61 (0.06)	17.60 (0.38)	6.30 (0.46)	4.67 (0.27)	11.6 (0.38)	1.68 (0.16)	0.08 (0.03)	660 (93)	97.11 (1.79)	2.89	1.19 (0.16)	0.034	0.573
P468	UA	RD0K	1	55.27 (1.52)	0.60 (0.05)	18.32 (0.26)	6.05 (0.19)	4.75 (0.34)	11.46 (0.42)	1.6 (0.18)	0.07 (0.02)	714 (78)	98.19 (1.65)	1.81	1.19 (0.16)	0.033	0.572
P470	UA	RD0K	4	52.82 (0.59)	0.58 (0.04)	19.48 (0.22)	5.47 (0.10)	4.95 (0.07)	12.05 (0.09)	1.64 (0.02)	0.07 (0.01)	705 (19)	97.13 (0.65)	2.87	2.43 (0.32)	0.034	0.571
P471	UA	RD0K*	4	55.98 (1.26)	0.59 (0.03)	17.28 (0.54)	5.71 (0.81)	5.03 (0.22)	11.5 (0.16)	1.72 (0.09)	0.08 (0.01)	637 (47)	97.96 (1.62)	2.04	1.38 (0.19)	0.034	0.570
P472	UA	RD6K*	4	53.49 (0.48)	1.12 (0.03)	16.65 (0.14)	4.44 (0.08)	3.31 (0.02)	9.83 (0.15)	2.70 (0.03)	6.25 (0.07)	842 (109)	97.88 (0.54)	2.12	1.31 (0.17)	0.046	0.585
P474	UA	RD6K	4	52.98 (0.70)	1.15 (0.03)	16.41 (0.06)	4.11 (0.04)	3.36 (0.03)	10.16 (0.09)	2.51 (0.03)	6.01 (0.09)	1184 (56)	96.82 (0.71)	3.18	2.58 (0.35)	0.045	0.580
P476	UBC	RD4K	4	53.05 (0.75)	1.12 (0.08)	15.55 (0.33)	5.12 (0.40)	3.75 (0.11)	9.95 (0.17)	3.07 (0.11)	4.34 (0.14)	1537 (45)	96.1 (0.96)	3.9	3.14 (0.42)	0.043	0.577
P476	UA	RD4K	4	54.08 (0.43)	1.11 (0.04)	16.30 (0.07)	4.95 (0.15)	3.81 (0.09)	9.88 (0.16)	2.98 (0.02)	4.22 (0.09)	1434 (45)	97.48 (0.51)	2.52	3.14 (0.42)	0.042	0.575
P478	UA	RD4K*	4	53.42 (0.19)	1.11 (0.05)	17.32 (0.11)	5.08 (0.03)	3.76 (0.06)	10.00 (0.06)	3.17 (0.04)	4.26 (0.07)	1025 (44)	98.22 (0.25)	1.78	1.28 (0.17)	0.043	0.584
P479	UBC	RD3K	4	54.70 (0.83)	0.90 (0.08)	18.02 (0.25)	1.85 (0.33)	4.18 (0.21)	11.33 (0.30)	2.28 (0.11)	3.35 (0.13)	1211 (113)	96.73 (1.01)	3.27	-	0.042	0.568
P480	UBC	RD1K	4	54.66 (0.56)	0.73 (0.04)	18.69 (0.23)	2.27 (0.26)	4.70 (0.09)	12.05 (0.21)	1.95 (0.14)	1.40 (0.06)	828 (27)	96.53 (0.72)	3.47	-	0.038	0.564
VG-2 analyses (n = 18)				49.68 (0.52)	1.86 (0.12)	13.35 (0.43)	11.67 (0.55)	6.9 (0.22)	10.84 (0.27)	2.59 (0.22)	0.21 (0.04)	1521 (81)					
VG-2 reference values[c]				50.81	1.85	14.06	11.82	6.95	11.12	2.62	0.19	1397 (172)					

*starting material dehydrated prior to use

** measured by Raman

[a] calculated as per Kress and Carmichael (1991)

[b] calculated as per Mills (1993) and Duffy (1996); see text and Supplementary table 3 for details

[c] Smithsonian microbeam standard NMNH 111240-52 recommended values; S concentration is the average of all reported analyses

Table 3.3: Composition of glasses, major elements in wt.%, S in ppm

3.3.2 Experimental procedure

Because S is highly reactive, the choice of capsule material is critical. The conditions of the experiments (1 GPa, 1270ºC) precluded the use of Au (Akella and Kennedy, 1971). Platinum is unsatisfactory due to severe Fe loss from the silicate melt to the capsule material, thus changing the melt composition and affecting SCSS. I found that $Au_{75}Pd_{25}$ capsules failed in experiments that ran longer than four hours due to the formation of PdS alloy, which melts at 600ºC thereby rupturing the capsule. I therefore used graphite capsules with a ~2 mm inner diameter, loaded with starting material and sealed with snugly fitting graphite lids. The graphite capsules were placed into ~6 mm long Pt capsules (3 mm outer diameter) which were sealed by welding.

Sealed Pt capsules were held in the centre of a 30 mm long graphite furnace on MgO spacers. The junction of a WRe_5-WRe_{26} ('Type C') thermocouple was positioned on a MgO disc ~0.5 mm above the Pt capsule, with the thermocouple otherwise protected by four-bore tubing made of high purity alumina. The capsule and graphite heater were placed within a 12.7 mm (outer diameter) $BaCO_3$ pressure assembly, wrapped in thin Pb foil to reduce friction with the pressure vessel. Experiments were performed at 1270ºC and 1 GPa in an end-loaded piston cylinder apparatus with temperature controlled by a programmable Eurotherm PID controller which maintained experiment temperature to within 2ºC. Pressure was manually controlled to within 0.02 GPa over the duration of each experiment. Friction correction on the $BaCO_3$ cells was determined to be less than 2% based on the melting point of Au at 1 GPa (Akella and Kennedy, 1971). A small 150 μm thick Pt wire was placed with the starting materials in two experiments (P479 and P480) to estimate the f_{O2} using the solubility of Fe in Pt (Médard *et al.*, 2008).

For each experiment, the sample was pressurized to 0.5 GPa at ambient temperature and left for one hour. Temperature was then raised to 600ºC at 40ºC/min and held for 6 minutes at 0.5 GPa, after which the temperature was raised to 1270ºC at 120ºC/min. Pressure was gradually increased during the second temperature ramp, reaching 1 GPa less than one minute after reaching temperature. Experiments were ended by shutting off power to the furnace, quenching the melt at an initial rate of ~2500ºC/minute and coming to room temperature in approximately 90 seconds. Capsules were extracted from the pressure assembly, mounted in 2.5 cm epoxy mounts and polished to expose the capsule and the glass with sulfide droplets in longitudinal section (Figure A-2).

3.3.3 Electron Probe Micro-Analysis (EPMA)

Chemical compositions of the experimental products were determined by EPMA at the University of British Columbia (UBC; Cameca SX-50) and the University of Alberta (UA; Cameca SX-100). At UBC, major elements in glass were analyzed using a beam diameter of 10 μm, beam current of 20 nA, accelerating voltage of 15 kV, with peak and background count times of 20 and 10 seconds, respectively. The S concentration in glass was determined using the same conditions but using 100 nA beam current with peak and background counting times of 240 and 120 seconds, respectively. The following standards were used: albite, Na (measured first); spinel, Al; diopside, Mg, Ca and Si; orthoclase, K; rutile, Ti; synthetic fayalite, Fe; pyrite, S. On the UA instrument, major elements in glass were analyzed using a beam diameter of 10 μm, beam current of 70 nA, accelerating voltage of 15 kV, with peak and background count times of 30 seconds (120 seconds for S). The UA instrument used the following standards: albite, Na; labradorite, Al; diopside, Mg, Ca and Si; sanidine, K; rutile, Ti; marcasite, Fe and S. For each

instrument, 10 – 15 points were selected on each glass, away from sulfide droplets. Sulfide droplets were not analyzed as they were often too small, or those that were large enough to analyze tended to polish poorly, resulting in rough surfaces and craters that prevented quality analysis. To ensure internal consistency, three glasses were analyzed with both the UBC and UA instruments. These duplicate analyses (listed in Table 3.3) are within error of each other for major elements and S, except for P478, where there is a ~7% discrepancy between the UA and UBC analyses which I consider to be minor. Multiple analyses of the VG-2 Juan de Fuca MORB glass standard (Smithsonian microbeam standard NMNH 111240-52) over several sessions gives an average of 1521 ± 82 ppm, within the range of recommended values for this material (1397 ± 172 ppm; Table 3.3), demonstrating the accuracy of the S analyses. Platinum wires were analyzed in experiments P479 and P480 at UBC using a beam diameter of 5 μm, a beam current of 100 nA, accelerating voltage of 15 kV with peak count times of 60 seconds for Fe and 30 seconds for Pt, with background count time of half the peak count time for these elements. The following standards were used for the metal analyses: pyrite, Fe; elemental metal, Pt.

3.3.4 Estimating the effect of alkali loss during EPMA

Exposure to a high current, small diameter electron beam during EPMA of hydrous silica-rich glasses (Morgan and London, 1996, 2005) can lead to significant under-reporting of the alkali elements, particularly Na, due to their migration away from the beam. This phenomenon results in artificially low alkali concentration and correspondingly low analytical totals and it is important to assess the extent to which my analyses are affected by alkali migration during beam exposure. Time dependent intensity

(TDI) corrections for Na, K, Si, Al and S were carried out for analyses done at UA using the Probe for EPMA Xtreme Edition software (Table A-1). TDI corrected concentrations of these elements are within error of the uncorrected values for all experiments except for Na_2O in P476 where the TDI corrected concentration is outside error of the uncorrected value. The difference between the TDI corrected and uncorrected Na_2O concentration of P476 is ~7% and is considered minor (Morgan and London 2005). Although TDI correction was not carried out at the UBC lab, the good agreement in analytical results from glasses analyzed at UA and UBC indicates that alkali loss is also not significant in the UBC analyses. In the discussion that follows, I use only the uncorrected alkali concentrations from the UA and UBC instruments.

3.3.5 H_2O measurement by Raman spectroscopy

Water content in experimental glasses may be estimated in a few different ways. Although H_2O content cannot be directly measured by EPMA, the difference of the sum of analyzed elements from 100 may be taken an indirect measure of the H_2O content of a glass. This 'by difference' method, however, is prone to errors associated with alkali loss during beam exposure, particularly for glasses with > 70 wt.% SiO_2 (Morgan and London, 1996, 2005). As discussed above, applying TDI corrections to my analyses shows little to no difference from uncorrected results for my glasses indicating that the analyses are not affected by alkali loss. Nevertheless, the 'by difference' method is still not ideal as it is only an indirect measure of H_2O.

Micro-FTIR spectroscopy is a direct means of measuring H_2O in glass but is sensitive to the presence of opaque phases, such as the sulfide droplets in my experiments. A recently developed means of directly measuring H_2O in glasses relates the area of the OH

stretching band at ~3550 cm^{-1} (A_w) in the Raman spectra to the glass H_2O content (Behrens *et al.*, 2006). Le Losq *et al.* (2012) show that normalizing A_w to the area of the Raman peaks relating to the glass silicate structure, from 100 – 1200 cm^{-1} (A_s), obviates compositionally dependent modification of the OH stretching band, thereby negating the need for compositionally matched calibration standards (e.g. Behrens *et al.*, 2006). The relationship between A_w/A_s and glass H_2O concentration demonstrated by Le Losq *et al.* (2012) is highly linear (to within 0.2 wt.%, 2σ). This method of H_2O measurement, calibrated for instrument differences (e.g. spectrometer CCD, grating etc.), was used by Fortin *et al.* (2015) in determining the H_2O concentration of glasses in their SCSS experiments.

I obtained Raman spectra of the glasses using a Renishaw inVia confocal Raman microscope at the University of Victoria using a 532 nm laser, 1200 line/mm grating and its 50x objective lens. At the start of each analytical session the spectrometer was calibrated on the ~520 cm^{-1} peak of a Si wafer. The position of the atmospheric N_2 Raman peak at ~2330 cm^{-1} served as another indicator of spectrometer calibration over the course of each analytical session. Spectra were obtained from 100 to 4000 cm^{-1} with an acquisition time of 60 seconds. The laser was focused on the sample surface and set to 10% power to avoid damaging the glasses. Three acquisitions were accumulated for each glass to maximize the signal-to-noise ratio in the resulting spectrum. The raw Raman spectra were corrected for temperature and frequency-dependent scattering as per Long (1977) and to improve baseline correction prior to peak fitting (Behrens *et al.*, 2006; Le Losq *et al.*, 2012). A linear baseline from ~3000 cm^{-1} to ~3800 cm^{-1} was subtracted from the spectra and four Gaussian peaks were fit to the OH band at ~3550 cm^{-1} for each glass.

In 100 – 1200 cm^{-1} region, the baseline subtracted was defined as a cubic spline anchored on the spectrum at ~200 cm^{-1}, ~640 cm^{-1}, ~800 cm^{-1} and ~1220 cm^{-1} as per Le Losq *et al.* (2012), and Gaussian peaks were fit to the resulting baseline-corrected spectra (Figure A-3). Baseline subtraction, peak fitting and area calculation were done using fityk (version 1.3.1). Because I did not have a range of glasses with independently known H_2O content with which to calibrate the slope of the A_w/A_s vs. H_2O relationship for the instrument I used, I initially applied the Le Losq *et al.* (2012) calibration. Measured in this way, the H_2O content of a MORB glass with known H_2O content (ALV1833-1, 2.14 wt.% H_2O determined using FTIR by Stolper and Newman, 1994) is 3.6 ± 0.2 wt.% H_2O. This overestimate of 59% relative to the known H_2O content of ALV1833-1 is unsurprising as the Le Losq *et al.* (2012) calibration is specific to the Raman instrument those authors used. I therefore corrected H_2O concentrations obtained from the Le Losq *et al.* (2012) calibration by a factor of 0.59 and tested the accuracy of this correction by measuring an andesite glass with H_2O content known by FTIR (Run 84, 3.80 ± 0.32 wt.% H_2O Mandeville *et al.*, 2002,). The corrected analysis of the Run 84 glass is 4.59 ± 0.62 wt% H_2O, within error of the FTIR H_2O concentration, indicating that this correction method is appropriate. Because the A_w/A_s relationship with H_2O content is independent of bulk composition (Le Losq *et al.*, 2012), the use of a MORB glass to determine the correction factor of the Le Losq *et al.* (2012) method for the instrument I used does not pose a problem for the varying alkali content of basaltic andesite glasses that I measure in this study.

The H_2O concentrations for the glasses in this study are listed in Table 3.3. Glass in experiment P470 was measured in multiple sessions, giving an average A_w/A_s of 5.7 ±

0.6, and H_2O concentration of 2.43 ± 0.32 wt.% as an indicator of precision. The H_2O concentrations determined by Raman spectroscopy are within 0.5 wt.% of the 'by difference' method (Figure 3.2). I was unable to analyze the glasses in experiments P479 and P480 due to excessive fluorescence. Although I recognize that it is not ideal, in the absence of any other means of determining H_2O concentration in P479 and P480, I use the 'by difference' method for those glasses.

3.4 Results

Experiments in graphite capsules consisted of glass, and 0.5 – 10 μm spherical sulfide droplets (Figure A-2). No bubbles are observed. Some experiments with RD0K starting material show a few pyroxene crystals (< 1 % by mode) in addition to glass and sulfide droplets (Table 3.2).

Experiments on the RD6K starting material run for 1 and 4 hours (P466 and P474, respectively) have similar S contents within error (Table 3.3), implying that 1 hour is sufficient time for complete diffusion of S within the melt. The majority of sulfide-saturated experiments in the present study were run for four hours (Table 3.2). The increased experiment duration tended to produce larger sulfide melt droplets, making it easier to analyze the glasses as they had larger sulfide-free portions. Sulfur concentration shows low 2σ variability in all glasses, < 10% and < 13% at high and low S concentrations respectively (Table 3.3), indicating homogeneity throughout the melt over the duration of the experiments.

The f_{O2} of two experiments in graphite capsules (P479, P480) was estimated using the solubility of Fe in Pt wire loops loaded in the charges (Médard *et al.*, 2008). I measured the Fe content of the Pt wire along three lines from the centre of the wire to ~3 – 5 μm

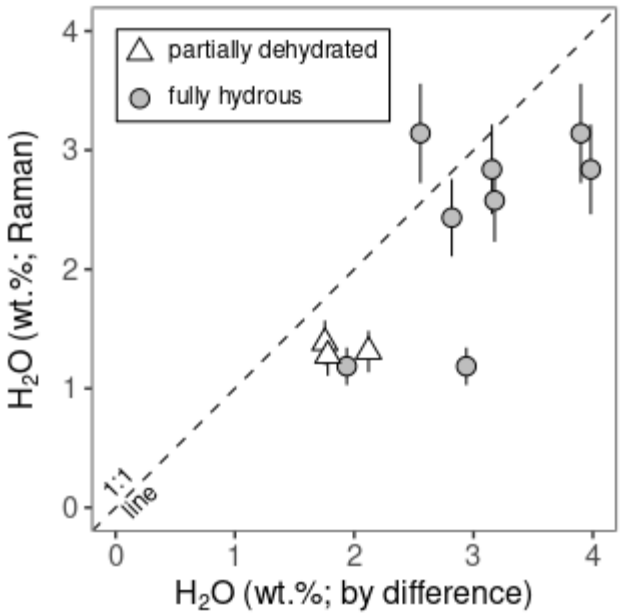

Figure 3.2: Comparison of H_2O measured directly by Raman spectroscopy and indirectly by EPMA (by difference method). Error bars are 2σ.

from the edge, using five to six spots per line (Table A-2). In each profile the concentration of Fe in the Pt wire varies from near zero at the centre to ~9 – 10 wt.% near the edge, indicating that the wire is not completely homogenized in these experiments. I used the maximum Fe contents measured at the wire edge to estimate the f_{O2} using the oxybarometer of Médard *et al.* (2008). For P480, the highest Fe concentration at the rim of the Pt wire (9.6 wt.%), corresponds to log f_{O2} = -8.7 (i.e. ΔFMQ = -1.9). For P479, the Fe concentration in the Pt wire (8.7 wt% Fe) corresponds to log f_{O2} = -8.1 (i.e. ΔFMQ = -1.3). Both of these results are within analytical uncertainty (~0.5 log units) of the CCO buffer (log f_{O2} = -8.7; ΔFMQ = -1.9), the expected maximum f_{O2} in graphite capsules (Médard *et al.*, 2008). In the calculations that follow I assume that f_{O2} of the experiments is equal to the CCO buffer at 1 GPa and 1270°C (i.e. log f_{O2} = -8.7).

Most glasses show FeO^{tot} concentrations of 4 – 6 wt.%, which is ~1.8 wt.% less FeO^{tot} compared to the starting materials. I attribute this Fe loss to the formation of sulfide in the experiments. Two glasses (P479 and P480, marked in Figures 3.3, 3.4) have ~2 wt.% FeO^{tot}, reflecting a loss of up to 4.5 – 5 wt.% FeO^{tot} relative to their starting materials. This level of Fe loss from the melt is due to the dissolution of Fe into the Pt wire placed in these charges to monitor f_{O2} as well as Fe partitioned into sulfide.

The major element composition of the glasses varies chiefly in the concentration of Al_2O_3, Na_2O and K_2O (Table 3.3). The SCSS of the glasses increases with Na_2O, K_2O and alkali/alumina ratio, and peaks at ~1500 ppm at K_2O = 4.4 wt.% (Figure 3.3). The low FeO^{tot} melts in P479 and P480 produce intermediate SCSS contents, on a trend from the lowest SCSS at low alkalinity (0% K_2O, 1.6% Na_2O) to high SCSS at 4.3 wt.% K_2O and 3.1 wt.% Na_2O.

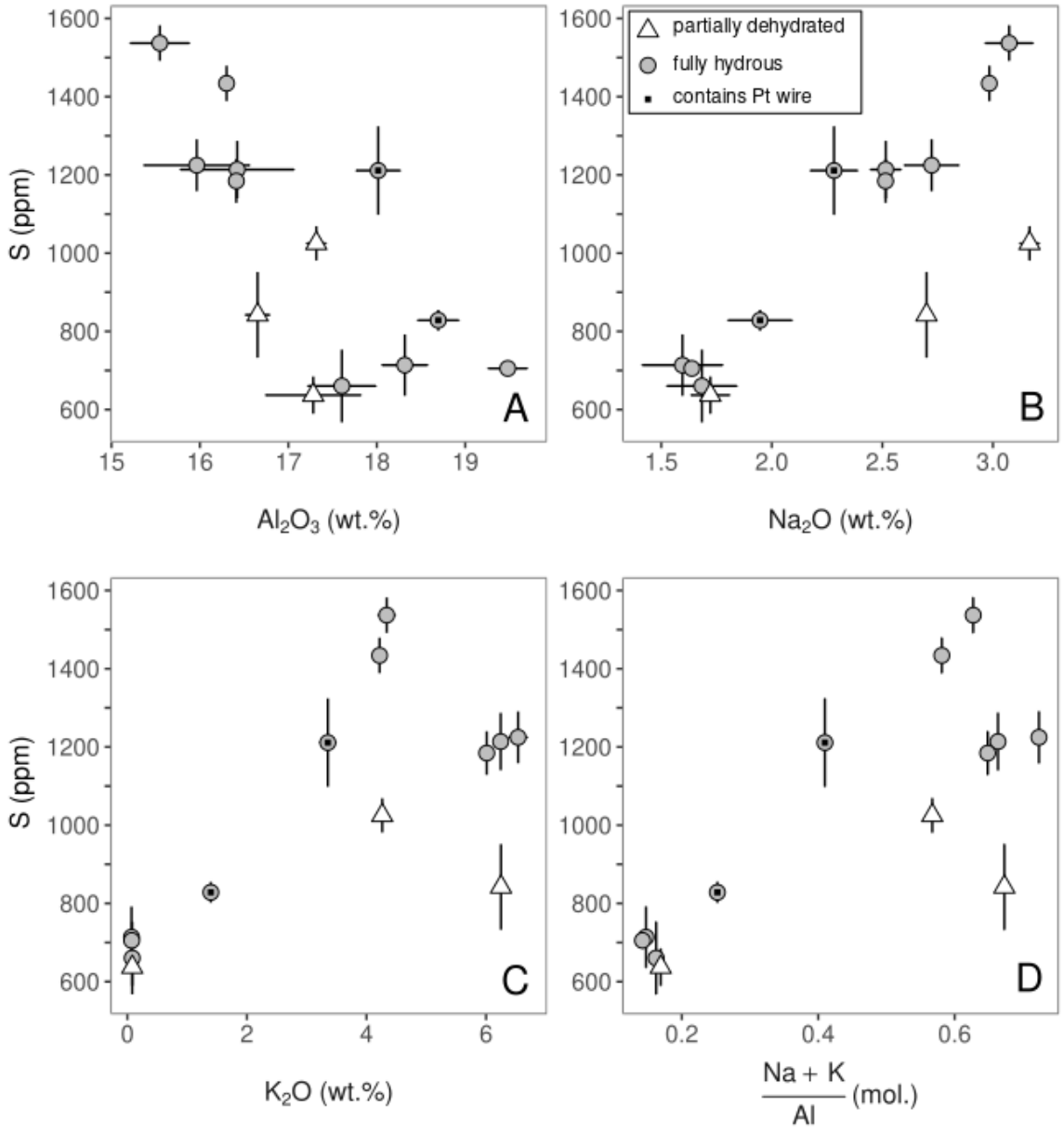

Figure 3.3: Bivariate diagrams showing S concentration in sulfide saturated glasses plotted against the concentration of a) Al_2O_3; b) Na_2O; c) K_2O; d) molar (Na + K)/Al. Error bars are 2σ. Experiments that contained Pt wire are marked with a small black square (see text for details).

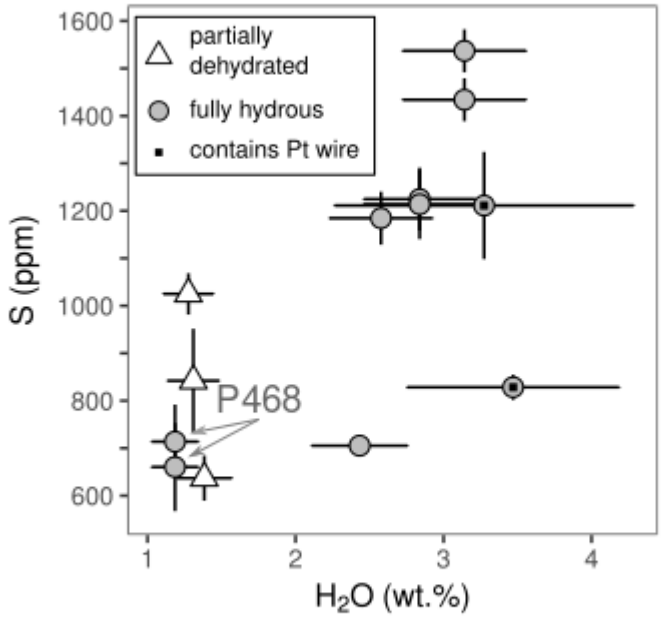

Figure 3.4: The variation of SCSS with H_2O in my experiments, showing that there is little difference between H_2O contents of my experiments, except when starting materials are partially dehydrated prior to capsule loading. Error bars are 2σ. The fully hydrous experiment P468 has low H_2O likely due to H_2O loss while welding the Pt capsules. Experiments that contained Pt wire are marked with a small black square (see text for details).

The concentration of H_2O in glasses from experiments for which starting materials were fully hydrated are similar within error (2.4 – 3.1 wt.%; Figure 3.4), except for P468 which shows 1.2 wt.% H_2O. Experiments for which the starting materials were partially dehydrated all have H_2O concentrations of ~1.3 wt.%. Experiments with different fully hydrous starting materials (P474, P466, P476, P470) show higher SCSS (by hundreds of ppm) than their partially dehydrated counterparts (P472, P478, P471) despite otherwise similar major element composition (Table 3.3). Experiment P468, which was not dehydrated, shows similar H_2O content as those glasses whose starting materials were partially dehydrated. A possible reason for this is that the experimental charge lost water during welding of the Pt capsule.

3.5. Discussion

3.5.1 Effect of alkalis and H_2O on SCSS

Of the fully hydrous experiments, P470 (RD0K starting material, ~1.7 wt.% total alkalis) shows the lowest S concentration, 705 ppm, whereas experiments P466 and P474 (RD6K, ~8.7 wt.% total alkalis) contain ~1200 ppm S and P476 (RD4K, ~7.4 wt.% total alkalis) contains ~1500 ppm S. The major element chemistry of P470, P466, P474 and P476 are similar, except for TiO_2 which is ~0.5 wt.% higher in P466, P474 and P476 (Table 3.3). Mysen *et al.* (1982) note that increasing TiO_2 decreases the NBO/T of a melt, and should decrease the SCSS by limiting the NBO that S can replace via reaction [3.1]. Thus, in the experiments using the RD0K, RD4K and RD6K starting materials, I can attribute increasing SCSS to increasing alkalinity, despite any deleterious effect of slightly higher TiO_2 in the high alkalinity experiments. An increase in SCSS with high alkali concentration is also observed in the glasses from lower H_2O starting materials

(Figures 3.3, 3.4). I observe that SCSS is higher by ~10% at low total alkali content, increasing to ~50% at high total alkali content (Figure 3.3b-d) in experiments using fully hydrated starting materials compared to those using lower H_2O in the same starting material.

In detail, my data shows that a maximum SCSS is observed at moderate alkalinity. Experiment P476 (7.4 wt.% total alkalis) shows 200 – 300 ppm more S than the highest alkalinity experiments P466 and P474 (~8.5 wt.% total alkalis). Experiment P478 (7.3 wt. % total alkalis) shows 180 ppm more S than P472 (8.9 wt.% total alkalis). There is a up to 1 wt.% increase in FeO content in the RD4K experiments compared to those in RD6K and, although SCSS is strongly affected by FeO^{tot} (Mavrogenes and O'Neill, 2002; Wykes *et al.*, 2015), the range of FeO^{tot} in the experiments discussed above (4.1 – 5.1 wt. % FeO^{tot}) lies in the relatively flat bottom of the U-shaped SCSS vs. FeO relationship. Thus, the observed change in FeO^{tot} is not expected to greatly impact SCSS. My observation that the highest alkalinity experiments have lower SCSS than moderate alkalinity ones implies that there exists a limit to the increase in SCSS solely as a function of alkalinity. That this limit also appears in the experiments using starting materials with differing H_2O contents increases my confidence that this apparent limit a real feature and not the result of a single aberrant experiment.

The alkalis are known to shift the Fe^{3+}/Fe^{2+} of melts at a given f_{O2} (Paul and Douglas, 1965; Gwinn and Hess, 1989; Cicconi *et al.*, 2015). At first glance, an increase in Fe^{3+}/Fe^{2+} by alkali addition may decrease the amount of S dissolved in a melt by Fe-S complexation which favours Fe^{2+}. This possibility is negated, however, by the stoichiometry of the reaction between the Fe and S redox couples in the melt (reaction

[3.3] above; Jenner *et al.*, 2010) indicating that increasing Fe^{3+}/Fe^{2+} will strongly increase the S^{6+}/S^{2-} of a melt and, as S^{6+} is more soluble in melts (e.g. Jugo *et al.*, 2005b), will increase the S concentration of a melt. Thus increasing Fe^{3+}/Fe^{2} with alkalinity will increase SCSS. It is possible that such a limit with increasing alkalinity may be imposed by changes in the melt environment of S. Such hypotheses can potentially be tested by detailed examination of the wavenumber regions where S bonds are observed in Raman spectra (200 -1200 cm^{-1} and ~2600 cm^{-1}; Klimm *et al.* 2012). The results of the Raman spectra I obtained to determine H_2O content (Section 3.3.5, Figure A-3) are not detailed enough in these wavenumber regions to distinguish peaks due to S bonding. At present I am unable to determine the reason for the limit to increasing SCSS with increasing alkalinity that I observe.

Experiments P479 and P480 used moderate alkalinity starting materials (RD3K and RD1K, respectively) and the glasses have ~2 wt.% FeO^{tot} , having lost some Fe to the Pt wire loops placed in them to monitor f_{O2}. Iron is known to exert a strong control on SCSS at FeO^{tot} contents below 1 – 2 wt.% (O'Neill and Mavrogenes, 2002; Wykes *et al.*, 2015), thus I have avoided using experiments P479 and P480 in describing the SCSS-alkalinity relationships above. However, the SCSS recorded by P479 and P480 increases in a linear manner between experiments using starting materials with lower and higher alkalinity. If the SCSS of P479 and P480 had been increased due to their lower FeO^{tot}, I would expect these two experiments to show much higher SCSS due to the very steep increase of SCSS with decreasing FeO^{tot} (Wykes *et al.*, 2015). Thus, I postulate the increases in SCSS in experiments P479 and P480 are due to their higher alkalinity and not due to their lower FeO^{tot}.

3.5.2 SCSS models and alkalinity

Modelling SCSS as a function of temperature, pressure and melt composition has been a goal of many studies. Mavrogenes and O'Neill (1999) used regression analysis to find coefficients for terms of an empirical SCSS model equation rooted in the thermodynamics of S^{2-} dissolution in silicate melts. Although those authors recognized the importance of melt composition on SCSS, their work in a restricted compositional space necessitated only the consideration of P and T. O'Neill and Mavrogenes (2002) conducted a large number of experiments at 1400°C and 1 bar to determine the effect of composition on SCSS in the CMAS ± Fe ± Ti system. Significantly, O'Neill and Mavrogenes (2002) found that SCSS has an asymmetric U-shaped relationship of melt FeO content with SCSS increasing at $FeO^{tot} < 1 – 2$ wt.% and $> 7 – 8$ wt.%. Holzheid and Grove (2002) noted that the degree of melt polymerization strongly controlled the SCSS and used a compositional parameter, the NBO/T ratio, to account for this in their model, based on data from anhydrous experiments. Scaillet and Pichavant (2005) presented a model for melt S content, that included a term for H_2O and six terms to account for T, P, f_{S2}, f_{O2} and a single compositional term, which itself embodies 10 oxide species terms. Liu *et al.* (2007) used a model of the form presented by Mavrogenes and O'Neill (1999), but using MFM to parameterize the melt composition. The MFM compositional parameter is a Fe^{3+}- and Fe^{2+}-bearing modification (Liu *et al.*, 2007) of the FM parameter used to predict rutile saturation (Ryerson and Watson, 1987). The FM paramter is itself a Fe- and Mg-bearing modification of the M paramter originally developed to predict zircon saturation (Watson and Harrison, 1983). The MFM parameter is closely related to NBO/T and calculated as:

$$MFM = \frac{Na + K + 2(Ca + Mg + Fe^{2+})}{Si(Al + Fe^{3+})} \quad [3.4]$$

using the mole fractions of each element per 100 g and calculating Fe^{2+} and Fe^{3+} by the method of Kress and Carmichael (1991). The negative dependence of SCSS on melt FeO content was included in the empirical model Li and Ripley (2005) developed for anhydrous compositions, although those authors removed this term in an updated model (Li and Ripley, 2009) that also accounted for H_2O.

The effect of H_2O on SCSS was explicitly tested and parameterized by Fortin *et al.* (2015) who present two empirical SCSS models that account for H_2O: one, an update of the Liu *et al.* (2007) MFM model, and a second model based on linear regression of oxides species present in the melt. Finally, Ariskin *et al.* (2013) found that Ni has a strong impact on the SCSS of a melt and developed an empirical relationship to account for this predicated on the existence of (Fe,Ni)S species in the melt. The empirical models developed by Fortin *et al.* (2015) include experiments with variable Ni in the melt and they found that their oxide species model predicted SCSS in these Ni-bearing melts to within 5%, thus avoiding the need to separately parameterize the Fe-Ni-S solution mechanism that Ariskin *et al.* (2013) advocated. In the following discussion, I refer to the models of Liu *et al.* (2007), Li and Ripley (2009) and Fortin *et al.* (2015) as these are recent SCSS models and are based on, and their predictions compare well against, larger and more comprehensive datasets than older models.

3.5.3 Previously published SCSS model results at varying alkalinity

In general, no single MFM model is consistently better than any other in predicting the SCSS of my experiments (Figure 3.5a). The Liu *et al.* (2007) model consistently deviates from the measured SCSS by 25% or more. The Fortin *et al.* (2015) MFM model best

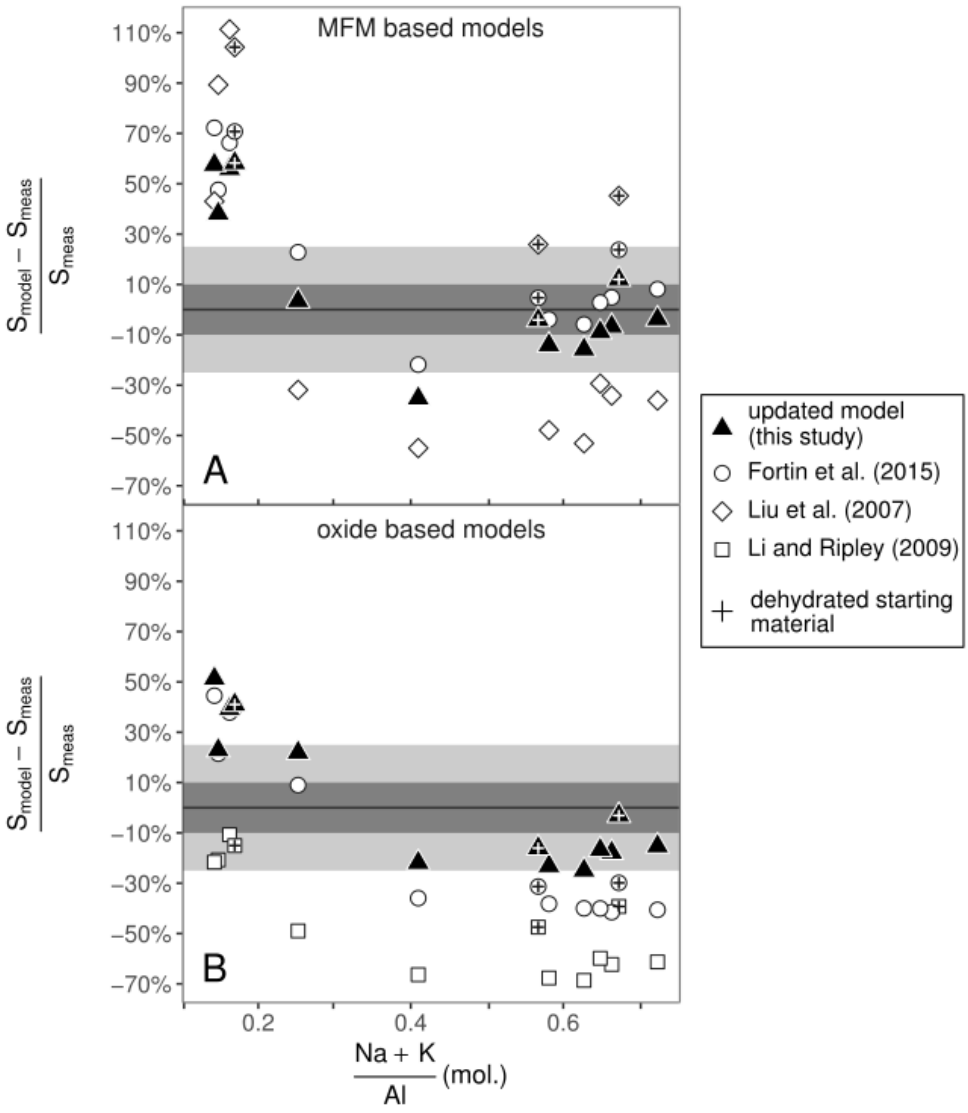

Figure 3.5: Percent difference between predicted and measured SCSS in my experiments plotted against molar (Na + K)/Al for a) MFM parameterized models (Liu *et al.*, 2007; Model A from Fortin *et al.*, 2015) and b) oxide species models (Li and Ripley, 2009; Model B from Fortin *et al.*, 2015). Also shown are the results of the updated models using data from the present study as black triangles. Experiments using partially dehydrated starting materials are indicated with a '+' in the symbol. The light grey and dark grey regions are 25% and 10% error envelopes, respectively.

predicts the SCSS in melts with high alkali concentration, deviating by ~10% from the measured SCSS though one experiment, P478 using dehydrated starting material, deviates by ~25%. The Fortin *et al.* (2015) MFM model deviates by +10 – -40% at moderate alkalinity and by up to 90% at low alkalinity. Comparing the oxide species models that I consider, the Fortin *et al.* (2015) model is more successful at predicting the SCSS of my experiments, deviating by 25 – 60% at low alkalinity to ~-40% at high alkalinity (Figure 3.5b). The Li and Ripley (2009) model performs best for low alkalinity glasses, underestimating SCSS by 15 – 25%, however this model underestimates the observed SCSS by 50 – 70% in higher alkalinity experiments.

Part of the reason these models inconsistently predict the effects of alkalinity on SCSS is due to the underlying data sets on which the models are calibrated. As discussed above, the effect of alkalis on SCSS has not been systematically studied, resulting in sparse coverage of the high alkali compositional space relative to other compositions (Figure 3.1), particularly for the basaltic andesite melts of this study. Although my experiments are on the outer limits of the compositional space of previous SCSS experiments, they are within the realm of many natural magmas in arcs, particularly the high-K or shoshonite series (Figure 3.1b). Therefore, to increase the calibrated range of SCSS models, I have used my new experimental results to retrain the two models presented by Fortin *et al.* (2015) and present a model of my own in the following sections.

3.5.4 Updates to previously published models

As discussed above and by Fortin *et al.* (2015), H_2O has a significant control on SCSS. I therefore use the dataset compiled by Fortin *et al.* (2015), containing only data from the literature where the H_2O content of sulfide-bearing melts was directly measured, together

with the results that I present in this study. I used a dataset comprising the 13 analyses from this study, the 18 analyses from Fortin *et al.* (2015) and the 234 analyses compiled by those authors (Baker *et al.*, 2001; Beermann *et al.*, 2011; Brenan, 2008; Ding *et al.*, 2014; Haughton *et al.*, 1974; Holzheid and Grove, 2002; Jugo *et al.*, 2005a, Liu *et al.*, 2007; Mavrogenes and O'Neill, 1999; Moune *et al.*, 2009; Peach and Mathez, 1993; Peach *et al.*, 1994; Righter *et al.*, 2009; Sattari *et al.*, 2002). Although there are a great many other SCSS studies than those listed above, I have not included them in my database primarily because they did not measure H_2O content directly or because they used very different bulk compositions (see Fortin *et al.* 2015 for details). This dataset was randomly split into a training subset comprising 201 analyses, including SCSS data from the present study, and a verification subset of 64 analyses (a 3:1 split of the overall dataset).

I determined coefficients to the parameters of the MFM and oxide species models (Table 3.4) presented by Fortin *et al.* (2015), using linear regression and 10-fold cross-validation, repeated 10 times, with the R package 'caret' (R Core Team, 2017; Kuhn, 2017). The retrained MFM model is:

$$\ln(SCSS_{ppm}) = 10.79 - \frac{5077}{T} - 310.9\frac{P}{T} + 0.4173\ln MFM + 0.4044\ln X_{FeO} + 3.513 X_{H_2O} \quad [3.5]$$

with T in Kelvin, P in GPa, and X_i being the mole fraction of oxide i. The coefficients to equation [3.5] are within error of those presented by Fortin *et al.* (2015), but the updated MFM model provides a slightly better fit to the training dataset (R^2 =0.827 for the updated model compared to 0.807 for the old model). The updated MFM model, however, performs more poorly on the randomly selected verification on the randomly

MFM			oxide model		
Parameter	Coefficient*	Coefficient**	Parameter	Coefficient*	Coefficient**
Intercept	10.79 (0.4399)	10.430 (0.428)	Intercept	30.359 (7.885)	34.784 (7.089)
1/T	-5077 (526.3)	-4981.6 (532.7)	1/T	-5829.233 (464.102)	-5772.3 (407.85)
P/T	-310.9 (51.88)	-332.37 (54.01)	P/T	-331.152 (40.118)	-346.54 (37.39)
ln[MFM]	0.4173 (0.04550)	0.45280 (0.03910)	X_{H2O}	-15.402 (7.863)	-20.393 (7.109)
$\ln X_{FeO}$	0.4044 (0.04279)	0.32270 (0.03650)	X_{SiO2}	-21.275 (7.856)	-25.499 (7.068)
X_{H2O}	3.513 (0.5537)	3.7449 (0.5663)	X_{TiO2}	-14.482 (8.291)	-18.344 (7.331)
			X_{Al2O3}	-22.231 (7.420)	-27.381 (6.683)
			X_{FeOtot}	-12.603 (7.975)	-17.275 (7.159)
			X_{MgO}	-17.967 (7.803)	-22.398 (7.003)
			X_{CaO}	-15.380 (7.970)	-20.378 (7.242)
			X_{Na2O}	-16.931 (8.333)	-18.954 (7.445)
			X_{K2O}	-19.246 (7.818)	-32.194 (7.556)
$R^2_{training}$	0.825	0.807	$R^2_{training}$	0.905	0.918
$R^2_{verification}$	0.777		$R^2_{verification}$	0.931	
$R^2_{overall}$	0.808		$R^2_{overall}$	0.912	
* this study					
** Fortin *et al.* (2015)					

Table 3.4: Comparison of MFM and oxide model parameter coefficients from Fortin *et al.* (2015) and as updated in the present study. All coefficients are provided to maximum available precision to avoid rounding errors in implementation. Values in parentheses are 1σ error.

selected verification dataset ($R^2 = 0.779$).

The updated oxide species model is:

$$\ln(SCSS_{ppm}) = 30.4 - \frac{5829}{T} - 331.2\frac{P}{T} - 15.40\,X_{H_2O} - 21.28\,X_{SiO_2} - 14.48\,X_{TiO_2} - 22.23\,X_{Al_2O_3} - 12.60\,X_{FeO^{wt}} - 17.97\,X_{MgO} - 15.38_{XCaO} - 16.93\,X_{Na_2O} - 19.25\,X_{K_2O} \quad [3.6]$$

with T, P and X_i as above. The coefficients to equation [3.6] are also within error of those presented by Fortin *et al.* (2015), and the updated model and the original oxide species models reproduce their training datasets similarly well: $R^2 = 0.905$ for the updated model compared to 0.918 for the original model. The updated model also performs well in predicting SCSS of the verification dataset ($R^2 = 0.931$). The greatest difference between the oxide species model coefficients presented by Fortin *et al.* (2015) and mine is for K_2O, though still within error.

The updated MFM model shows negligible improvement overall, with SCSS predictions that are consistently 10 – 15% lower than the Fortin *et al.* (2015), resulting in smaller differences between predicted and observed SCSS at low alkalinity, but slightly greater difference at high alkalinity (Figure 3.5a). The updated oxide species model is more obviously improved, giving SCSS predictions that are ~25% lower than observed SCSS at high alkalinity (Figure 3.5b). The updated oxide species model fares as well as the original Fortin *et al.* 2015 oxide model at low alkalinity overestimate the SCSS by upto ~50%.

3.5.5 Developing a new model

I chose to develop a new SCSS model based on the MFM model of Liu *et al.* (2007), updated by Fortin *et al.* (2015). Models relying on universal melt descriptors depend on the linearity of the relationship between observed SCSS and the chosen compositional

parameter. On that basis, Liu *et al.* (2007) chose the MFM paramener, which is effectively the ratio of network modifiers to network formers present in a melt and a high MFM implies a high NBO/T. In natural log space, MFM shows a linear relationship against observed SCSS for the experiments in the Fortin *et al.* (2015) compilation (Figure 3.6a) . I observe, however, that the experiments from my study show little separation in MFM values even though they vary from subalkaline low K to alkaline shoshonitic compositions. This lack of variation for such a large compositional shift is likely why the MFM model performance with changing alkalinity is not significantly changed between the updated MFM model I present above and that presented by Fortin *et al.* (2015).

In an effort to find a compositional parameter that better reflects the variation in alkalinity of my experiments, I have assessed the performance of optical basicity (Λ, lamda). Optical basicity is a universal melt descriptor used in material sciences to quantify the polymerization of slags and is essentially the weighted average of the negative charge borne by the cations in a melt (Mills, 1993). As per Mills (1993), Λ is calculated as:

$$\Lambda = \frac{\sum X_i n_i \Lambda_{th,i}}{\sum X_i n_i} \quad [3.7]$$

where X_i is the mole fraction of oxide i, n is the number of O associated with i, $\Lambda_{th,i}$ is the theoretical Λ of i and the summation is over the different oxide species present in the melt. In the present work, I used values for Λ_{th} for the oxide species (Table A-3) from Mills (1993) and Duffy (1996). The mole fractions of Fe_2O_3 and FeO were calculated using the Kress and Carmichael (1991) algorithm. Similar to MFM, Λ also has a linear relationship with observed SCSS. However, because Λ accounts for the identity of the

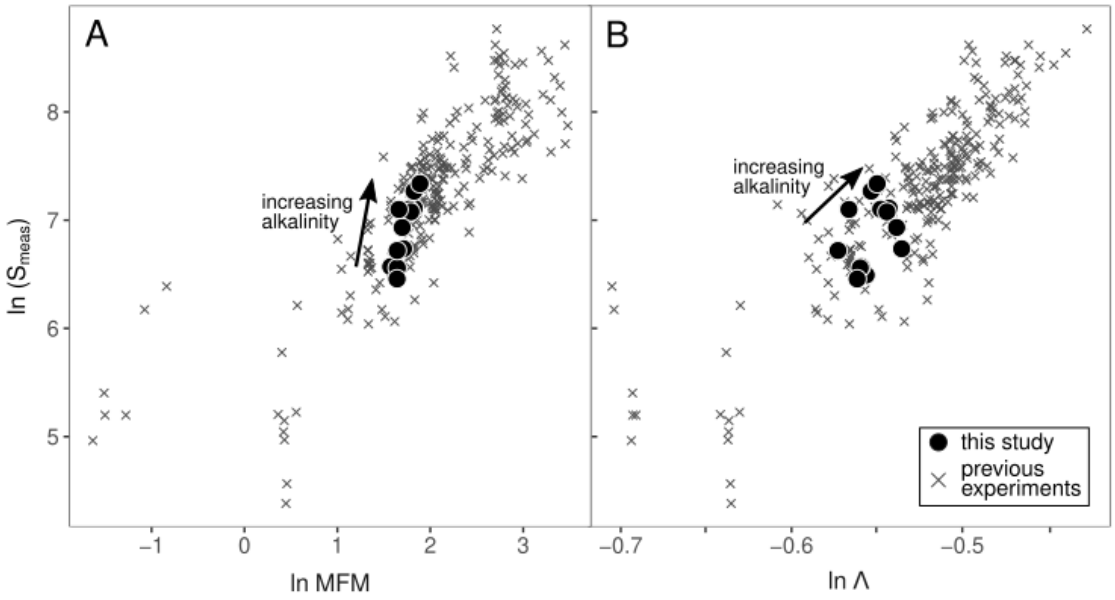

Figure 3.6: SCSS in experimental glasses from this and previous work (see text for references) plotted as a function of a) MFM and b) optical basicity, Λ, calculated using the equation [3.7] with the optical basicity values given by Mills (1993) and Duffy (1996). The arrows point in the direction of increasing alkalinity of the glasses from the present study.

cation via Λ_{th}, in addition to the relative abundance, the high alkalinity glasses from my study have higher Λ compared to low alkalinity glasses (Table 3.3, Figure 3.6b).

I used Λ in an empirical SCSS model with the same form as the MFM model of Fortin *et al.* (2015):

$$\ln SCSS_{ppm} = a + \frac{b}{T} + c\frac{P}{T} + d\ln\Lambda + eX_{FeO} + fX_{H_2O} \quad [3.8]$$

where T is temperature in Kelvin, P is pressure in GPa, Λ is optical basicity calculated as above (equation [3.7]), X_{FeO} is the mole fraction of FeO calculated by the method of Kress and Carmichael (1991), and X_{H2O} is the mole fraction of H_2O. Fortin *et al.* (2015) used $\ln X_{FeOtot}$, however, I found that using X_{FeO} gave an improved fit (see Section 3.5.6 for the implications of this). I found the coefficients to equation [3.8] (referred to hereafter as the OB model for brevity) by multiple linear regression with the R package 'caret' (R Core Team, 2017; Kuhn, 2017), using 10-fold cross-validation repeated 10 times, applied to the same training and verification datasets as used above to update the Fortin *et al.* (2015) models to include my new data. The resulting OB model is:

$$\ln SCSS_{ppm} = 16.34 - \frac{5784}{T} - 339.4\frac{P}{T} + 10.85\ln\Lambda + 3.750\,X_{FeO} + 6.704\,X_{H_2O} \quad [3.9]$$

The values of the coefficients are given with their standard errors in Table 3.5 to the maximum available precision to avoid rounding errors in implementation.

The OB model fits the training and verification datasets with R^2 values of 0.869 and 0.891, respectively. The OB model predicts SCSS in the training and verification datasets to within 5 – 10% of the measured value in natural log space (Figure 3.7a) for all but two cases at low SCSS. This is equivalent to differences between predicted and observed SCSS of -50 – 120% over the full range of observed SCSS (Figure 3.7b), though in most

Parameter (label)*	Coefficient	Std. Error
Intercept (a)	16.3415	0.4237
1/T (b)	-5784.0562	433.8896
P/T (c)	-339.3541	44.5225
ln[Λ] (d)	10.8476	0.6743
X_{FeO} (e)	3.7504	0.6464
X_{H2O} (f)	6.7032	0.4834
$R^2_{training}$ = 0.869		
$R^2_{verification}$ = 0.891		
$R^2_{overall}$ = 0.874		
* labels refer to equation [8] in text		

Table 3.5: OB model parameters

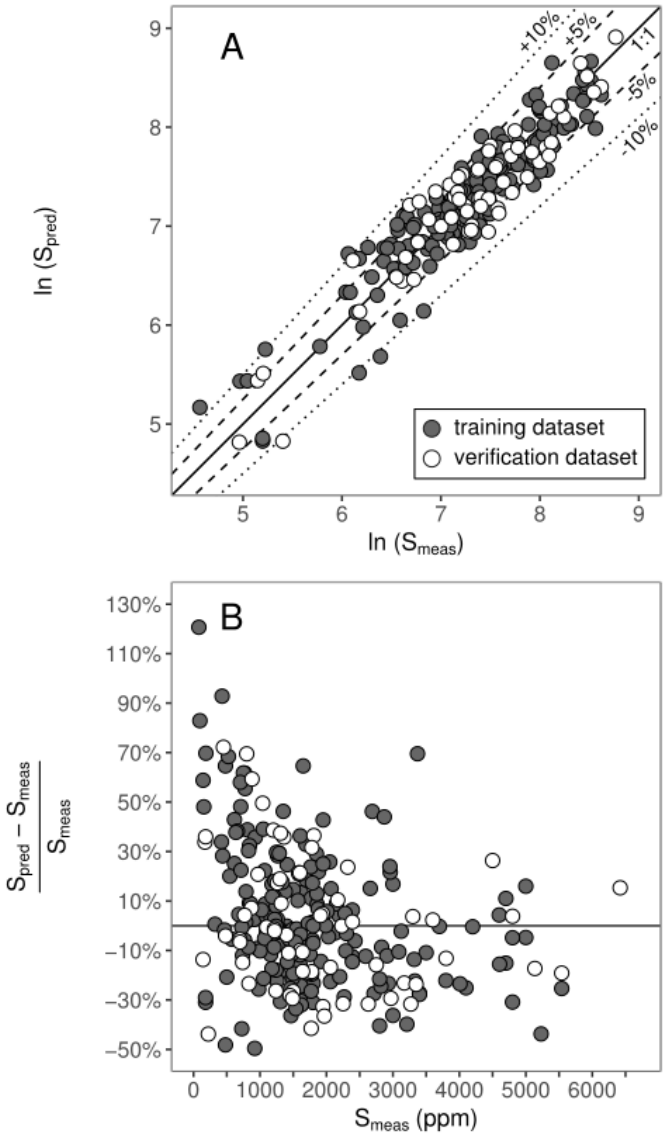

Figure 3.7: a) Predicted SCSS plotted against measured SCSS using the OB model for the training and verification datasets. The solid line shows a 1:1 relationship (0% error) and the dashed and dotted lines are 5% and 10% error envelopes respectively. b) The percent difference between modelled and measured SCSS in training and verification datasets plotted against measured SCSS.

cases SCSS is < 70% overestimated by the OB model. The range of difference between predictions and observations that I observe in the training and verification datasets is similar to that observed by Fortin *et al.* (2015) for their oxide species model.

Overall the OB model reduces the spread of predicted SCSS for all my experiments to within -10 – 60% of the observed SCSS, compared to -35% to 60% for the updated MFM model (Figure 3.8) and -25 – 70% for the Fortin *et al.* (2015) MFM model (Figure 3.7a). In detail, the Fortin *et al.* (2015) MFM model performs better at high alkalinity, predicting SCSS to within -10 – 25%, compared to OB model predictions which deviate by 10 – 35% from the observed SCSS. In the lowest alkalinity glasses, the OB model fares better than either the Fortin *et al.* (2015) MFM model or my update to that model, with predictions ~20 – 30% closer to the actual SCSS than either of those models.

The difference between the observed and predicted SCSS is larger at the highest and lowest alkalinity for the OB model but is within 10% of the observed SCSS at moderate to high alkalinity (Figure 3.8). One reason for this may be gleaned from considering the range of compositions for which SCSS experiments have been carried out. Figure 3.1 shows that the silica and alkalinity range of published SCSS experiments is quite small when considering experiments for which H_2O concentrations have been directly measured. At low alkalinity, the majority of experiments are basaltic compared to the basaltic andesite compositions studied here and there is almost no previous work in the compositional region of my highest alkalinity experiments. Thus, my experiments at the extremes of alkalinity are on the edge of the compositional space in which my SCSS models have been calibrated and it is to be expected that the model performance will be degraded at these extremes (Figure 3.8). On the other hand, my experiments at moderate

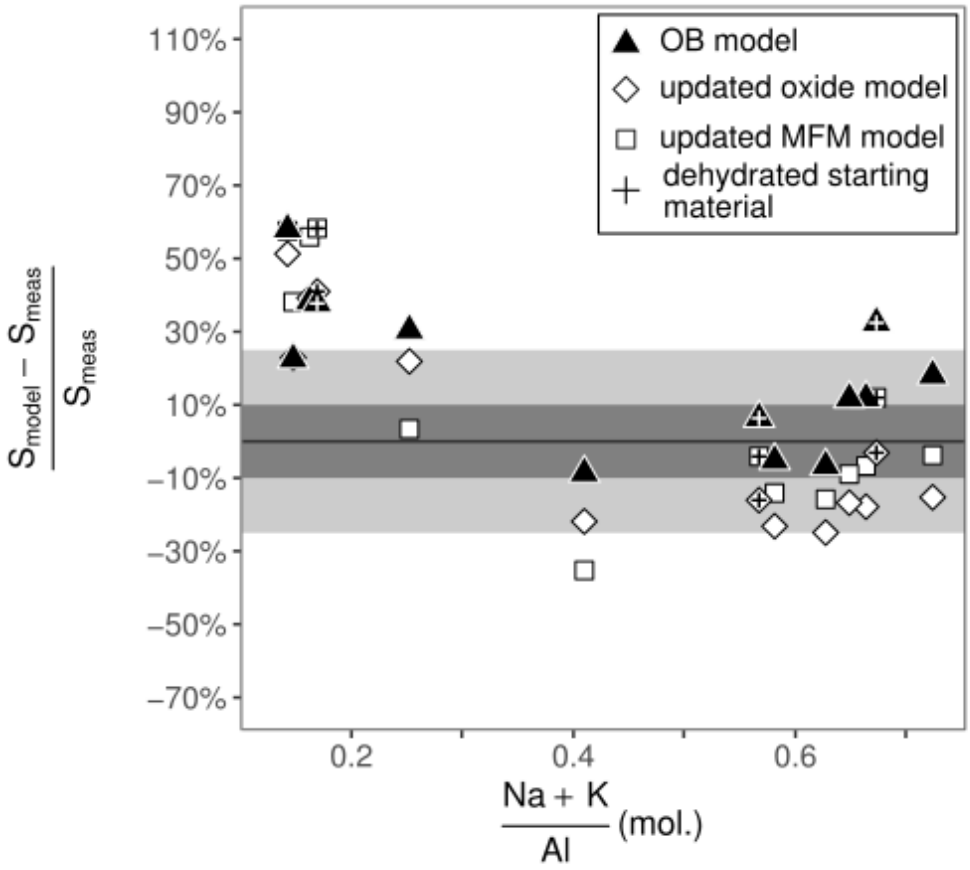

Figure 3.8: Percent difference between predicted and measured SCSS in my experiments plotted against molar (Na + K)/Al for the OB model from the present study. Also shown are the results of the updated MFM and oxide species models presented in this study. The light grey and dark grey regions are 25% and 10% error envelopes, respectively.

to high alkalinity occupy a region of compositional space where the database of experiments shows the greatest co-variation of alkalis and SiO_2 (Figure 3.1). The OB model accordingly performs well at moderate alkalinity, predicting SCSS to within 10% of the observed value (Figure 3.8).

3.5.6 SCSS models and low FeO systems

The work of O'Neill and Mavrogenes (2002) and Wykes *et al.* (2015) indicates the importance of FeO on SCSS, both at high concentration (> 8 wt.% FeO^{tot}) and at low concentration (<1 – 2 wt.% FeO^{tot}). The variation of SCSS with FeO^{tot} describes an asymmetric U-shape with a very steep limb at low FeO^{tot}, due to a negative $\ln X_{FeO}$ term in the thermodynamically derived relationship between SCSS, P, T and melt composition (O'Neill and Mavrogenes 2002). I have tried including this term in the OB model, with and without X_{FeO}, and training the model using the dataset described above in addition to the results from O'Neill and Mavrogenes (2002). From these trials, I found that the fit of the model to the training and verification datasets were severely reduced (typical R^2 values of ~0.5) likely owing to the very different compositions studied by O'Neill and Mavrogenes (2002) compared to the large database of experiments used here. Additionally, inclusion of the > 200 O'Neill and Mavrogenes (2002) data skews the overall dataset to low pressure (100 kPa) and relatively high temperatures (1673 K), thus reducing the fit of data at higher pressures and lower temperatures. I therefore have not considered the negative $\ln X_{FeO}$ term in the present work, although I recognize that the effect of low FeO is undoubtedly important in highly evolved granites and pegmatites, for example.

3.6 Conclusions

I have investigated effect of alkalis and H_2O on the SCSS of basaltic andesite melts. The alkalis and H_2O affect the degree of polymerization of a melt which strongly controls the SCSS as noted by previous studies. My results show that SCSS increases in a melt with increasing alkalinity, showing an approximately two-fold increase in SCSS for melts with high alkalinity (~1500 ppm S) compared to low alkalinity (~700 ppm S), when other compositional parameters (i.e. SiO_2, FeO^{tot}, H_2O) are unchanged. My work also shows an apparent peak in SCSS at total alkali content of ~7.5 wt.% although I have been unable to determine the mechanism for such a limit. The results I have presented show that the ability of alkaline melts to carry S has been under-appreciated and this is particularly important in the geological S cycle given the increasing alkalkinty of arc magmas with maturity and thickness of arcs (e.g. Green, 1980).

Whereas the MFM and oxide species models of Fortin *et al.* (2015) overestimate SCSS at low alkalinity by 40 – 70%, those authors' MFM model performs well with ~10 – 25% deviation from observed SCSS at high alkalinity. The Fortin *et al.* (2015) oxide species model underestimates SCSS by ~40% at high alkalinity. Part of the reason for this inconsistency in predicting SCSS with changing alkalinity is that the effect of SCSS on alkalinity in basaltic andesite melts has not been systematically tested previously. Thus, models trained on earlier datasets cannot fully capture the variation in SCSS with alkalinity. I recalibrated the SCSS models of Fortin *et al.* (2015) and find that the updated models reduce the spread of over- and under-estimates of SCSS. I also present a new model that builds on the work of Fortin *et al.* (2015), but employs the theoretical optical basicity (Mills, 1993; Duffy, 1996) to take into account the different identities of network modifiers and network formers and not just the mole fractions of each as previous

compositional parameters have done. Compared with earlier models and the updated ones I present, the OB model reduces the spread of SCSS predictions with changing alkalinity and also provides a slightly better fit to the overall database of SCSS experiments for which H_2O concentration is directly measured.

Chapter 4.
The partitioning of chalcophile elements between sediment melts and fluids at 3 GPa, 950 – 1050ºC and implications for slab fluids in subduction zones

4.1 Abstract

It is generally agreed that the distinctive enrichment of large ion lithophile elements in arc lavas reflects the influence of fluids sourced from a subducting slab. There is also growing evidence for the importance of sediment melts in transferring trace elements into the arc mantle. Of the trace elements enriched in arcs, the chalcophile elements are of particular interest due to their differing compatibility in sulfide and sulfate phases, the stability of which are themselves dependent on sediment redox. Many studies have shown that chalcophile elements are compatible in saline aqueous fluids at pressures relating to shallow levels of arcs (<10 km below the surface) but there is comparatively limited work on chalcophile element mobility in aqueous fluids at P-T conditions relevant to sediment melting. In the present study, I performed piston cylinder experiments at 3 GPa and 950 – 1050ºC on pelite melt compositions doped with S, V, Sc, Ce, Mo, As, Sb and Pb at reduced conditions where pyrrhotite (Po) is stable and at oxidized conditions where anhydrite (Anh) is stable. The trace element composition of quenched melts in my fluid-saturated experiments was analyzed and used to determine the fluid composition by mass balance. The concentration of lithophile elements V and Sc in melts and fluids are unaffected by redox, however Ce concentration is higher in melts and lower in fluids in reduced experiments compared to oxidized ones. Of the chalcophile elements, S is in higher concentration in the melts and fluids whereas Mo, As, Sb and Pb, are enriched in melt and depleted in fluid in oxidized experiments. The partition coefficients determined for these elements are the first reported at the conditions of subduction in reduced f_{O2}

conditions where Po is present (at 1000ºC, $D^{fluid/melt}$ Ce = 4 ± 0.3, $D^{fluid/melt}$ Mo = 319 ± 43, $D^{fluid/melt}$ As = 669 ± 134, $D^{fluid/melt}$ Sb = 1437 ± 208, $D^{fluid/melt}$ Pb = 73 ± 4) and in oxidized conditions where Anh is present (at 1000ºC, $D^{fluid/melt}$ Ce = 150 ± 48, $D^{fluid/melt}$ Mo = 3.7 ± 1.9, $D^{fluid/melt}$ As = 2.5 ± 1.7, $D^{fluid/melt}$ Sb = 12 ± 5.1, $D^{fluid/melt}$ Pb = 3.8 ± 1.8; all errors are 1σ). My results are consistent with the notion that low Mo/Ce in lavas from the Lesser Antilles arc, occurred due to sulfide breakdown in subducted black shales, but with concomitant enrichment by sediment melts and not fluids. The Mo/Ce ratio may be a promising tool in other arcs to infer the role of fluid (or not) for chalcophile enrichment.

4.2 Introduction

It has long been recognized that the volcanic arcs formed at convergent tectonic margins show distinctive enrichment in large ion lithophile elements (e.g. K, Rb, Cs), chalcophile elements (e.g. Mo, Cu, As, S) and the light REE, and show depletion in high field strength elements (e.g. Nb, Ta, Zr) relative to basalts from mid-ocean ridges or ocean islands (e.g. Hawkesworth *et al.*, 1991). The source of this geochemical 'arc signature', particularly regarding chalcophile element enrichment, is debated. One view holds paramount the importance of processes occurring in the over-riding plate like crustal contamination (e.g. Bezard *et al.*, 2015) and magma or sulfide fractionation in the lower crust (e.g. Lee *et al.*, 2012; Chiaradia, 2014). The other view is that the chalcophile element enrichment observed in arc magmas reflects enrichment of the source mantle by components of the subducting slab (e.g. Noll *et al.*, 1996; Mungall, 2002; Freymuth *et al.*, 2015; Turner and Langmuir, 2015).

A potent source for the enrichment of the arc mantle is the sedimentary veneer of the subducting slab which is known to contain high concentrations some trace elements

(Plank and Langmuir, 1993; 1998) relative to MORB. The role of sediments has been clearly illustrated by Freymuth *et al.* (2016), showing that the heavy $\delta^{98/95}$Mo signature of lavas from the Lesser Antilles arc could only be related to black shales subducted beneath this arc. In this view, the trace element enrichment characteristic of arcs may result from aqueous fluids, silicate melts or supercritical melts of subducted sediments. In this chapter I refer to 'aqueous fluids' and 'silicate melts' simply as 'fluids' and 'melts' for brevity. Although there is strong evidence for the importance of fluid transfer of these elements, including the chalcophile elements (e.g. Noll *et al.*, 1996; Jégo and Dasgupta, 2014; Freymuth *et al.*, 2015), it is also possible that sediment melts may transfer these elements to the arc mantle wedge. Fluid-absent melting of pelitic sediment occurs at 870 – 1050ºC at 3 GPa, though fluid-fluxing can reduce these temperatures by up to 200ºC (Mann and Schmidt, 2015). Thermal models predict a wide range of sub-arc temperatures (400 – 900ºC; e.g. van Keken *et al.*, 2002; England and Wilkins, 2004) and a growing amount of petrological evidence suggests these models may underestimate temperatures (Labanieh *et al.*, 2012; Penniston-Dorland *et al.*, 2015; Yogodzinski *et al.*, 2017). Additionally, sediments may also melt by buoyantly rising from the subducting slab as diapirs (Marsh, 1979) thereby reaching hotter regions of the mantle wedge (e.g. Gerya *et al.*, 2006; Behn *et al.*, 2011; Marschall and Schumacher, 2012). The existence of supercritical melts in the sub-arc setting is presently debated with some studies locating the second critical end-point (SCEP), beyond which there is complete miscibility between silicate melts and aqueous fluids, at 900ºC and 1.5 GPa (Bureau and Keppler, 1999) whereas others locate the SCEP at 900 – 1000ºC and > 5 GPa (e.g. Schmidt *et al.*, 2004; Kessel *et al.*, 2005a).

A long history of geochemical and experimental studies have examined how slab-derived fluid can transport lithophile trace elements to enrich or oxidize the sub-arc mantle (e.g. Green and Adam, 2003; Kessel *et al.*, 2005b; Brounce *et al.*, 2014). In contrast, although there are many studies on chalcophile element partitioning in aqueous fluids at crustal pressures (e.g. Keppler and Wyllie, 1991; Scaillet *et al.*, 2006; Keppler, 2010; Simon *et al.* 2007; Zajacz *et al.*, 2008), there are far fewer investigations at conditions melt generation beneath arcs. Jégo and Dasgupta (2013, 2014) show $D^{fluid/melt}$ for S up to at least 2000 in basaltic partial melts at sub-arc conditions (2 – 3 GPa, 800 – 1050ºC). Bali *et al.* (2012) show that W and Mo are both highly fluid mobile at high P and that Mo mobility is enhanced by fluid salinity and increasing f_{O2}. Chalcophile element enrichment has also been observed in oxidized sediment melts (Skora *et al.* 2017; Canil and Fellows, 2017). It is also important to consider the effect of redox on chalcophile element fluid-melt partitioning as, in S-bearing melts, reduced conditions favouring sulfide stability dramatically lowers the chalcophile element concentration in the melt phase. In the present study, I seek to fill this knowledge gap by experimentally quantifying if fluids in equilibrium with sediment melts can carry chalcophile elements and how this varies with redox.

4.3 Methods

4.3.1 Starting materials

The starting materials used here, PM and CM3 (Table 4.1), are liquid compositions from melting experiments on Fe-rich (Ca/Fe = 0.62) and Ca-rich (Ca/Fe = 0.98) pelite at 3 GPa 1050°C by Mann and Schmidt (2015) and Tsuno and Dasgupta (2011), respectively (Figure 4.1). I chose melt compositions of sediments based on previous

	Sediment melts		Starting materials	
	BE1116*	G58**	PM	CM3
Major elements (wt.%)				
SiO_2 (wt. %)	73.45	72.67	70.65	69.47
TiO_2	0.40	0.48	0.38	0.31
Al_2O_3	15.70	14.45	15.33	13.92
FeO^T	0.86	1.84	3.11	3.81
MgO	0.14	0.22	0.13	0.39
CaO	0.42	2.56	1.69	2.39
Na_2O	3.08	2.51	2.96	3.20
K_2O	5.96	5.26	5.74	6.51
Sum^+	100	100	100	100
S	-	-	1.92	2.01
H_2O	3.48	-	3.97	6.28
CO_2	-	4.68	-	-
Ca/Fe (mol)	0.62	0.98	0.69	0.80
Trace elements (ppm)				
Sc	-	-	74.3	100.8
V	-	-	92.7	120.7
As	-	-	65.0	95.4
Mo	-	-	23.5	18.9
Sb	-	-	54.7	61.7
Ce	-	-	114.8	99.9
Pb	-	-	107.5	95.7

* Mann and Schmidt (2015)
** Tsuno and Dasgupta (2011)
$^+$ volatile-free

Table 4.1: Starting materials compositions for this study and the sediment melts they are based on.

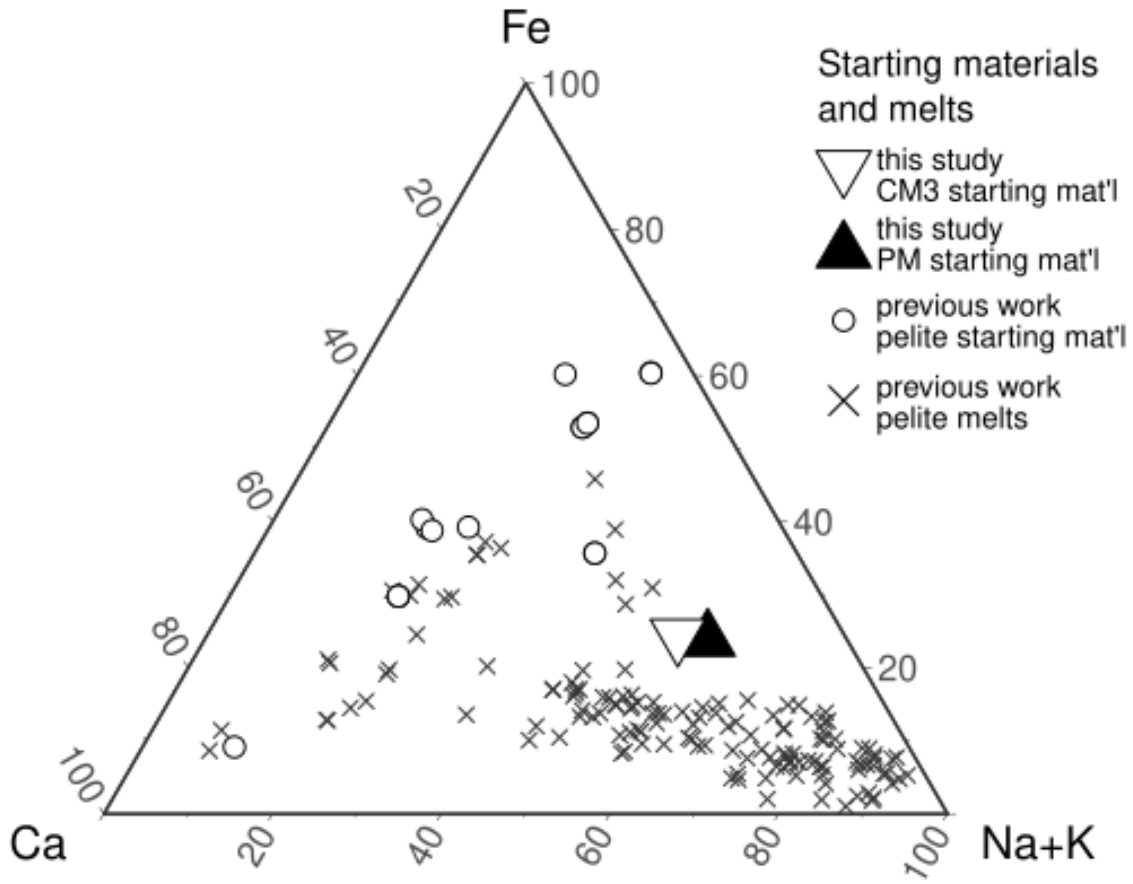

Figure 4.1: Ternary diagram of molar Ca-Fe-(Na+K) showing the compositions of my starting materials in the context of starting materials used in previous sediment melting studies and the range of sediment melts generated in previous studies.

experimental work for my starting materials in order to maximize melt volumes in my experiments and enable easier *in-situ* microanalysis by LA-ICP-MS. Two different starting material compositions were examined to test the effect of bulk Ca/Fe on the position of the sulfide-sulfate transition in f_{O2} space (Canil and Fellows, 2017) or its possible effect on the fluid-melt partitioning of chalcophile trace elements.

For each starting material, reagent grade oxides (SiO_2, TiO_2, Al_2O_3, Fe_2O_3 and MgO) and carbonates ($CaCO_3$, Na_2CO_3 and K_2CO_3) were weighed out, shaken together and ground under ethanol. The mechanically mixed material was decarbonated overnight at 900°C and fused at 1400°C for 12 hours in a Pt crucible before quenching to a glass in H_2O. The glass was crushed, ground and fused a second time, then re-ground to a powder. Gibbsite, $Al(OH)_3$, was then weighed into the glass powder as a source of H_2O, followed be re-grinding and drying under a heat lamp. A total of 2 wt.% S was then added to the starting materials as ferro-sulfate monohydrate ($FeSO_4.H_2O$) and $CaSO_4$. Following the addition of S as a combination of $CaSO_4$ and $FeSO_4$, starting materials PM and CM3 have a final Ca/Fe of 0.69 and 0.80, respectively. Approximately 7 g of each starting material was then doped with Sc, V, Ce, Mo, As, Sb, and Pb (Table 4.1), added as dilute ICP-MS standard solutions of HNO_3, and the final mixture was dried under a heat lamp. Trace element concentrations in PM and CM3 were confirmed by solution ICP-MS (Table 4.1).

4.3.2 Experimental procedure

Experiments were carried out in a 12.7 mm end-loaded piston cylinder apparatus. Starting materials were packed into 2 mm outer diameter (o.d.) Au capsules together with a small loop of 30 μm thick Pt wire and then welded shut. Two such capsules, each

containing different starting materials, were then placed into an outer Au capsule (3.5 mm o.d.) packed with $Al(OH)_3$ and, for reduced experiments, powdered graphite. The outer capsule was then also welded shut. The capsule was placed in the centre of a 30 mm tall cylindrical graphite furnace using crushable MgO spacer blocks. The graphite furnace was placed in a CsCl pressure cell, which was lined externally with Pb foil to reduce friction against the WC pressure vessel. The friction correction for the CsCl assembly is essentially nil (Canil, 1999).

Temperature was monitored by a WRe_5-WRe_{26} (i.e. 'Type C') thermocouple and controlled by to within 2°C by a Eurotherm PID controller connected to the thermocouple via an Omega ice-point. At the start of each experiment, pressure was held constant at 0.5 GPa and ambient temperature for 1 hour, followed by heating at 40°C/min to 600°C where P and T were held for 6 minutes. The temperature was then increased at the same rate while pressure was gradually increased such that the experiment reached the target temperature approximately 1 minute after reaching target pressure. Experiment conditions are given in Table 4.2. Pressure was controlled to within 0.02 GPa and each experiment was quenched (after 24 or 48 hours) by shutting off power to the furnace, reaching room temperature in < 15 seconds. Experimental products were sectioned with a diamond saw, impregnated with epoxy under vacuum, mounted in a 2.5 cm epoxy puck and polished with successively finer sandpaper up to 1600 grit. To prevent the dissolution of crystalline sulfate phases, the capsules were cut and polished without the aid of H_2O. Although final polishing was done with a 6 and 0.25 μm diamond suspension, I did not observe any dissolution of crystalline sulfate phases due to the use of H_2O-based suspensions in this step.

Run	SM	T (°C)	Duration (h)	phase modes, by weight																	Σr^2 *
				liq	±1σ	fl	±1σ	anhy	±1σ	po	±1σ	gt	±1σ	qtz	±1σ	ky	±1σ	cpx	±1σ	ox	±1σ	trace	
P487a	PM	1000	24	0.821	0.056	0.045	0.007	0.025	0.001			0.040	0.010	0.036	0.040	0.022	0.014					ox	0.35
P498b	PM	1000	48	0.846	0.035	0.043	0.004	0.011	0.001	0.032	0.001			0.030	0.024	0.038	0.009						0.17
P486a	PM	1050	24	0.870	0.005	0.049	0.005	0.026	0.002							0.043	0.004			0.013	0.002	qtz	1.81
P494b	PM	950	48	0.904	0.004	0.043	0.003			0.039	0.002					0.014	0.004					gt, ox, ttn	0.18
P490a	PM	1000	24	0.862	0.006	0.048	0.004			0.051	0.003					0.039	0.005					qtz	1.74
P491a	PM	1000	48	0.903	0.004	0.047	0.004			0.050	0.003											qtz	1.82
P491b	PM	1000	48	0.877	0.003	0.046	0.002			0.048	0.001					0.029	0.000						0.99
P497b	PM	1000	48	0.888	0.005	0.044	0.003			0.044	0.002					0.024	0.004					ox	0.24
P494a	CM3	950	48	0.808	0.010	0.068	0.004			0.046	0.001					0.033	0.003	0.045	0.008				0.55
P495b	CM3	950	48	0.814	0.011	0.068	0.003			0.040	0.002							0.078	0.013			qtz	0.35

* sum of squared residuals of mass balance

Abbreviations: gt, garnet; qtz, quartz; anhy, anhydrite; ky, kyanite; cpx, clinopyroxene; po, pyrrhotite; ox, Fe-Ti oxide; ttn, titanite

Table 4.2: Experiment conditions and resulting phase proportions. All experiments carried out at 3 GPa.

4.3.3 Buffering and measuring f_{O2}

Oxygen fugacity (f_{O2}) is a main control on sulfide saturation in a given S-bearing system. Because Au capsules are permeable to H_2, the f_{H2} from the dissociation of H_2O in the outer capsule is imposed on the inner capsules. To ensure sulfide saturation, I loaded a small amount of graphite in the outer capsule of the experimental charges, to buffer the f_{H2} of the inner capsule at the CCO oxygen buffer (i.e. ΔFMQ = – 1.3 at 1000ºC and 3 GPa). Except as noted below, experiments without graphite in the outer capsule saturated in sulfate and had high melt S commensurate with a high $S^{6+}/\sum S$ indicating their f_{O2} is greater than at least FMQ + 2 at experimental conditions (Jugo *et al.* 2005a; 2005b; 2010). I attempted to directly measure the f_{O2} of the experiments with the Fe-in-Pt oxybarometer (Médard *et al.*, 2008) by placing a small Pt wire loop in the capsules, however this was unsuccessful as the Pt alloyed with the S to form PtS. Where garnet or clinopyroxene were observed and analyzed by EPMA, I calculated f_{O2} using the GAP and CASP buffers of Canil and Fellows (2017; Table 4.3).

4.3.4 Electron Probe Micro-Analysis (EPMA)

Experiments were analyzed by EPMA at the University of British Columbia (Cameca SX-50). Major elements in glasses were analyzed using a 10 μm beam diameter, 15 kV accelerating voltage and 10 nA beam current, with peak and background count times of 20 seconds and 10 seconds, respectively. Sulfur in glass was analyzed with the same conditions, except using a 100 nA beam current with peak and background count times of 240 seconds and 120 seconds, respectively. Glass analyses were calibrated against the following standards: albite, Na (analyzed first); spinel, Al; diopside, Mg, Ca and Si; orthoclase, K; rutile, Ti; synthetic fayalite, Fe; pyrite, S. Repeated analysis of Juan de

Run #	P487a			P498b			P486a			P494b					P490a			P491a			P491b				P497b			P494b			P495b					
SM	PM			PM			PM			PM					PM			PM			PM				PM			CM3			CM3					
T (°C)	1000			1000			1050			950					1000			1000			1000				1000			950			950					
t (hours)	24			48			24			48					24			48			48				48			48			48					
graphite?	n			n			n			y					y			y			y				y			y			n					
phase	glass	±1σ	gt	glass	±1σ		glass	±1σ		glass	±1σ	gt	±1σ	po	glass	±1σ		glass	±1σ		glass	±1σ		po	±1σ	glass	±1σ		glass	±1σ		glass	±1σ	cpx	±1σ		VG-2 analyses (n = 18)	±1σ	VG-2 Reference values	±1σ
Major elements (wt.%)																																									
SiO_2	72.68	0.62	36.51	73.24	0.30		73.19	0.34		72.59	0.25	38.65	0.34	-	-	-		74.00	0.40		72.75	0.45		73.55	0.22	-	-		73.54	0.34		73.52	0.41		72.91	0.24		72.91	0.33		52.91	0.46		49.68	0.26		50.81	-
TiO_2	0.36	0.02	1.15	0.36	0.03		0.39	0.03		0.35	0.05	0.37	0.03	-	-	-		0.41	0.02		0.43	0.02		0.45	0.03	-	-		0.42	0.03		0.36	0.03		0.33	0.06		0.33	0.03		0.47	0.03		1.86	0.06		1.85	-
Al_2O_3	14.65	0.27	20.22	14.28	0.18		13.46	0.18		14.84	0.21	32.99	0.37	-	-	-		14.06	0.24		15.13	0.13		14.49	0.11	-	-		14.55	0.17		12.88	0.13		6.97	0.61		14.16	0.16		13.88	0.60		13.35	0.21		14.06	-
FeO[1]	1.63	0.08	35.31	1.04	0.06		2.47	0.21		0.29	0.05	0.39	0.04	58.03[3]	0.28	0.05	0.73	0.26	0.03		0.27	0.03		0.27	0.04	57.14[3]	0.92		0.21	0.04		0.52	0.06		8.49	0.78		0.60	0.09		7.69	1.57		11.67	0.27		11.84	-
MgO	0.11	0.01	4.19	0.15	0.02		0.48	0.14		0.18	0.02	0.29	0.04	-	0.23	0.01		0.49	0.03		0.22	0.01		0.27	0.04	-	-		0.19	0.02		0.24	0.03		9.10	0.55		0.13	0.02		5.26	0.78		6.90	0.11		6.95	-
CaO	0.26	0.02	2.49	0.12	0.05		0.82	0.10		1.75	0.04	23.83	0.23	-	1.80	0.07		2.07	0.10		1.88	0.03		3.12	0.06	-	-		1.92	0.05		1.84	0.08		16.92	0.78		1.60	0.04		11.84	1.34		10.84	0.13		1.112	-
Na_2O^*	3.26	0.09	0.42	3.27	0.08		3.13	0.10		3.08	0.11	0.09	0.02	-	3.14	0.12		3.02	0.08		3.12	0.06	-	3.12	0.06	-	-		3.12	0.06		3.37	0.08		3.68	0.32		3.01	0.07		6.04	0.42		2.59	0.11		2.62	-
K_2O^*	6.35	0.11	-	6.33	0.12		6.06	0.13		5.95	0.13	0.05	0.02	-	6.09	0.16		5.85	0.10		6.03	0.09	-	6.03	0.09	-	-		6.04	0.08		7.26	0.09		0.13	0.07		7.27	0.13		0.10	0.04		0.21	0.02		0.19	-
S	0.149	0.012	-	0.048	0.005		0.139	0.007		0.038	0.005	-	-	39.61	0.026	0.002	0.679	0.080	0.003		0.049	0.002	38.71	0.060	0.004	0.53		0.060	0.004		0.031	0.004		-	-		0.032	0.009		-		0.152	0.004		0.140	0.009
total	99.46		100.29	100.05			100.14			99.07		96.66		97.64	100.03			100.08			100.05		95.85		100.06			100.03			98.87			98.19			97.25			99.58	
H_2O^*	7.88	0.70	-	8.83	0.39		8.26	0.50		9.68	0.38	-	-	-	8.45	0.52		10.73	0.50		8.66	0.28	-	8.92	0.40				9.29	0.40		9.29	0.46		-	-		9.49	0.41		-	-		-	-		-	-
H_2O^{**}	8.38	0.70	-	9.11	0.39		10.46	0.50		9.91	0.38	-	-	-	11.03	0.52		12.71	0.50		10.56	0.28	-	9.50	0.40				10.72	0.46		-	-		-	-		10.11	0.41		-	-		-	-		-	-
																																							BCR2-g analyses (n = 19)	±1σ	BCR2-g Reference values	±1σ	
Trace elements (ppm)																																									
Sc	69.0	8.5	-	-	-		-	-		-	-	-	-	-	71.6	2.5		99.4	2.0		116.7	3.1	-	98.1	1.9		71.9	1.8	-	-		49.0	6.9	-	-		0.21	-		-	-		-	-		-	-
V	85.2	26.2	-	79.0	9.7		74.9	1.7		68.6	1.5	-	-	-	63.3	1.6		70.3	0.9		63.9	1.0	-	51.7	7.5		54.7	3.2	-	-		50.0	13.0	-	-		0.06	-		-	-		-	-		-	-
As	78.6	7.5	-	60.7	12.9		73.6	1.6		7.5	2.4	-	-	-	4.4	1.5		bdl	-		bdl	-	-	2.4	1.5		8.7	1.9	-	-		40.5	2.6	-	-		-	-		2.6	1.2		0.7–2.5	-		-	-
Mo	24.5	0.9	-	11.4	0.7		28.3	0.5		1.4	0.4	-	-	-	3.6	1.6		bdl	-		bdl	-	-	5.0	0.85		bdl	-	-	-		5.3	1.9	-	-		-	-		262.8	13.7		270	30		-	-
Sb	43.6	3.6	-	17.9	3.2		48.5	0.9		1.7	0.1	-	-	-	1.4	0.1		0.6	0.1		bdl	-	-	1.5	0.7		2.0	0.1	-	-		9.0	0.8	-	-		-	-		0.3	0.7		0.35	0.08		-	-
Ce	15.6	4.3	-	106.3	2.5		38.8	0.6		55.9	0.7	-	-	-	95.0	2.8		107.9	1.6		126.4	1.4	-	113.9	0.7		114.7	3.3	-	-		107.7	7.5	-	-		-	-		53.7	2.3		53.3	0.5		-	-
Pb	111.1	5.7	-	136.7	16.0		113.6	1.8		36.6	1.1	-	-	-	32.7	1.2		24.4	0.6		21.3	0.5	-	25.1	2.0		42.8	1.1	-	-		80.4	1.5	-	-		-	-		10.4	0.4		11	1		-	-
$X_{fluorapatite}$	-	-	-	-	-		-	-		-	-	-	-	-	-	-		-	-		-	-	-	-	-		-	-	-	-		-	-	-	-		0.23	-		-	-		-	-		-	-
X_{Cl-Ap}	-	-	-	-	-		-	-		-	-	-	-	-	-	-		-	-		-	-	-	-	-		-	-	-	-		-	-	-	-		0.03	-		-	-		-	-		-	-
$X_{whitlockite}$	-	-	0.77	-	-		-	-		-	-	0.01	-	-	-	-		-	-		-	-	-	-	-		-	-	-	-		-	-	-	-		-	-		-	-		-	-		-	-
$X_{graphite}$	-	-	0.07	-	-		-	-		-	-	0.97	-	-	-	-		-	-		-	-	-	-	-		-	-	-	-		-	-	-	-		-	-		-	-		-	-		-	-
X_{pyr}	-	-	0.16	-	-		-	-		-	-	0.02	-	-	-	-		-	-		-	-	-	-	-		-	-	-	-		-	-	-	-		-	-		-	-		-	-		-	-
ΔFMQ[2]	-	-	-	-	-		-	-		-	-	-	-	-	-	-		-	-		-	-	-	-	-		-	-	-	-		-	-	-	-		0.80	-		0.56	-		-	-		-	-
ΔFMQ[3]	-	-	0.59	-	-		-	-		-	-	-0.60	-	-	-	-		-	-		-	-	-	-	-		-	-	-	-		-	-	-	-		-	-		-	-		-	-		-	-

* Na_2O and K_2O corrected by mass balance procedure (see text)

** Sum using uncorrected Na_2O and K_2O

[1] Fe content of pyrrhotite reported in wt.% Fe, not FeO

[2] CAP buffer, Canil and Fellows (2017)

[3] GAP buffer, Canil and Fellows (2017)

bdl = below detection limit (3 x blank concentration)

Table 4.3: Phase compositions measured by EPMA (major elements, S) in wt.% and LA-ICP-MS (trace elements) in ppm.

Fuca MORB glass VG-2 (Smithsonian NMNH 111240-52) over several sessions gives an average of 1521 ± 82 ppm (n = 18, Table 4.3) , within the range of values recommended for this glass standard (1397 ± 172 ppm). Garnet and pyroxene were analyzed using a 5 μm beam (1 μm for very small crystals), 15 kV, 20 nA, counting for 20 seconds on the peak and 10 seconds on background. Pyroxene analyses were calibrated using albite, Na; kyanite, Al; diopside, Mg, Si, Ca; orthoclase, K; rutile, Ti; fayalite, Fe. Garnet analyses were calibrated using albite, Na; pyrope, Mg, Al, Si, Ca, Fe; rutile, Ti. Sulfides were analyzed using a 2 μm beam, 20 kV and 20 nA, 20 seconds counting on the peak and 10 seconds counting on the background. Analyses of Fe and S in sulfide were calibrated using pyrite.

4.3.5 Laser Ablation-Inductively Coupled Plasma-Mass Spectrometry (LA-ICP-MS)

Trace elements (^{45}Sc, ^{51}V, ^{75}As, ^{95}Mo, ^{121}Sb, ^{140}Ce, ^{208}Pb) in experimental glasses were determined by LA-ICP-MS at the University of Victoria, using a New Wave UP-213 laser ablation system and a Thermo X-Series II (X7) quadrupole ICP-MS. The laser was run at 60% power, ~6.2 J/cm^{-2} fluence with a beam diameter of 40 μm. Background signal was collected for 30 seconds, then laser was pulsed for 30 seconds, with the peak signal decaying to background levels approximately 20 seconds after the laser was shut off. Background-subtracted analyses were internally standardized using Si as measured by EPMA and externally calibrated against NIST glasses 611, 613 and 615. No drift correction was required. Typical detection limits for Sc and As were ~1.3 ppm; V, 6.2 ppm; Mo, Sb, Ce and Pb, 0.5 – 0.8 ppm. Multiple analyses of BCR2-g reproduce the concentration of these elements within the uncertainty of GEOREM preferred values (Table 4.3). Arsenic in BCR2g has no GEOREM preferred value, but the average of my

analyses (2.6 ± 1.2 ppm, n = 19) is within uncertainty of the reported range of previous analyses (0.7 – 2.5 ppm).

4.3.6 Phase modes and fluid composition

To obtain proportions of the phases present in the experiments, I used an iterative mass balance approach similar to that described by Jégo and Dasgupta (2014). I used anhydrous glass compositions, measured compositions for garnet and clinopyroxene where observed, ideal compositions for Fe-Ti oxide (ilmenite), quartz, kyanite, titanite, pyrrhotite (Po) and anhydrite (Anh) and a fluid consisting of initially pure H_2O. Least-squares mass balance was performed iteratively with a custom R script using the 'limSolve' package (R Core Team, 2017; Soetaert *et al.*, 2009). After each iteration, the sulfur content in the fluid was estimated as the difference between the bulk S contained in the glass, Po and/or Anh and the amount of S in the starting material. The resulting fluid concentration was then used in the next iteration of the mass balance calculation and the process was repeated until the fluid S concentrations converged. Less than 90 iterations were required for the fluid S concentration to converge to within 0.1 wt.% in all experiments. Phase modes converged to within 10% relative in less than five iterations. The phase modes and uncertainties reported in Table 4.2 are the mean and standard deviation of 1000 Monte Carlo runs to account for the error in phase compositions. Relative uncertainty on the modes is < 2% (1σ) for glass and < 10% for all other phases.

Alkali migration during beam exposure has long been recognized as a significant problem in EPMA of silicic hydrous glasses (Morgan and London, 1996; 2005) such as the glasses in this study. To reduce uncertainty resulting from this phenomenon in the mass balanced phase modes, I excluded Na_2O and K_2O from the mass balance

calculations. However by keeping track of the bulk Na_2O and K_2O in crystalline phases during the mass balance procedure, I determined 'corrected' Na_2O and K_2O contents in the melt (Table 4.3), assuming that these elements are not fluid compatible. This calculation method provides the maximum possible concentration Na2O and K2O possible in the melt and gives analytical totals that are 0.6 – 1.3 wt.% higher than the values reported from EPMA (Table 4.3).

The trace element concentration of the fluid was calculated by mass balance using the calculated phase modes, measured concentrations in the glass and estimated trace element compositions of the mineral phases present (see below). Determining the fluid compositions, thus $D^{fluid/melt}$ values, by mass balance ideally requires complete knowledge of the trace element budget in a system. Trace element concentrations in glass were measured directly using LA-ICP-MS (Table 4.3) but those in the mineral phases were estimated from mineral-melt partition coefficients (Table 4.4) as the crystals were too small for analysis by LA-ICP-MS. The EPMA results for the sulfides in my experiments (Table 4.3) indicate that they are Po ($Fe_{1-\alpha}S$), but I cannot rule out ppm levels of Sb, As and Pb (Barton, 1971; Stimac and Hickmott, 1994). Arsenic and Pb are known to be present up to 40 ppm in Po (Stimac and Hickmott, 1994) and since Po makes up < 5 wt.% in the experiments (Table 4.2), it will contains less than 3% of the trace element budget of As and Pb. I thus ignore the Po contribution to the As, Sb and Pb budget in the mass balance calculations. Quartz and kyanite were assumed to contain no trace elements. Given these assumptions, my estimates of $D^{fluid/melt}$ are maxima. Where element concentrations are below analytical detection limits, P491a (As, Mo), P491b (As, Mo, Sb) and P494a (Mo; Table 4.3), I calculated the fluid composition and $D^{fluid/melt}$ for these

element	mineral	$D^{mineral/melt}$	$\pm 1\sigma$	melt composition	reference
Sc	gt	63	*2.9*	rhyolite	Sisson (1992)
	cpx	150	*38*	rhyolite	Sisson (1991)
V	gt	7	*0.6*	rhyolite	Sisson (1992)
	cpx	14	*1.4*	rhyolite	Sisson (1991)
	Fe Ti oxide	248	*121*	dacite	Klemme *et al.* (2006)
As*	po	3	-	rhyolite	Stimac and Hickmott (1994)
Mo	po	35	*3.0*	rhyolite	Mengason *et al.* (2011)
Ce	cpx	1.1	*0.1*	rhyolite	Sisson (1991)
Pb*	po	2	-	rhyolite	Stimac and Hickmott (1994)
* not used in mass balance (see text)					

Table 4.4: Mineral-melt partition coefficients used for trace element mass balance

elements using their detection limit as a maximum estimate of their concentration in the melt, resulting in minimum fluid concentrations and $D^{fluid/melt}$ estimates.

I implemented a Monte Carlo mass balance procedure in R (R Core Team, 2017), to calculate the fluid trace element composition from the phase compositions, phase modes and the bulk composition, taking into account the uncertainties on these three parameters. The calculation procedure produced 30,000 estimates of fluid concentration for each trace element in each experiment. I took the mean and standard deviation of these estimates as the fluid composition and the uncertainty, respectively (Table 4.5). In the case of Sc, its concentration in the melt was near that in the starting material and calculated fluid concentrations ranged to negative values, indicating that the melt phase (plus garnet and clinopyroxene, where observed) contained almost all of the Sc budget. Calculation of fluid compositions in the manner described above relies on the robustness of assumptions made in the calculation, particularly the choice of mineral/melt partition coefficients ($D^{fluid/melt}$) to constrain the various minerals' contribution to the trace element budget. As melt is by far the most abundant phase in my experiments, I contend that the general patterns of trace element enrichment or depletion, if not their absolute concentrations, in the fluids is robust and unaffected by the choice of particular values of $D^{mineral/melt}$. I nonetheless tested the sensitivity of my results for $D^{fluid/melt}$ Mo on the choice of the $D^{Po/silicate\ melt}$ used to estimate the Mo concentration in Po by varying the latter by ± 50%, but find that there is little effect outside of uncertainty (see below).

4.4 Results

4.4.1 Experimental run products and phase assemblages

Table 4.5: Mass balanced fluid compositions and Dfluid/melt

Run	SM	T (°C)	fluid concentrations (S in wt.%, all other in ppm)															
			S	±1σ	Sc	±1σ	V	±1σ	Ce	±1σ	Mo	±1σ	As	±1σ	Sb	±1σ	Pb	±1σ
P487a-avg	RDPM	1000	10.8	*1.7*	-	-	423	*318*	2337	*383*	91	*46*	193	*136*	513	*217*	417	*201*
P498b avg	RDPM	1000	6.6	*0.7*	15	*12*	636	*198*	568	*131*	42	*29*	439	*228*	887	*199*	225	*174*
P486a-avg	RDPM	1050	9.7	*1.2*	289	*107*	710	*180*	1781	*226*	10	*8*	117	*92*	318	*146*	214	*108*
P494b avg	RDPM	950	8.9	*1.0*	67	*51*	712	*127*	1488	*106*	472	*44*	1362	*182*	1252	*200*	1735	*156*
P490a-avg	RDPM	1000	4.2	*0.9*	279	*80*	801	*123*	704	*81*	293	*45*	1269	*164*	1139	*158*	1639	*165*
P491a-avg	RDPM	1000	3.9	*1.1*	-	-	640	*99*	363	*52*	447*	*46*	1345*	*154*	1098	*186*	1794	*166*
P491b-avg	RDPM	1000	5.0	*0.5*	-	-	777	*94*	110	*54*	467*	*38*	1364*	*130*	1203*	*139*	1949	*129*
P497b avg	RDPM	1000	6.6	*0.9*	-	-	1043	*179*	320	*63*	247	*39*	1424	*162*	1208	*140*	1947	*160*
P494a avg	CM3	950	4.1	*0.4*	-	-	628	*139*	51	*34*	249*	*15*	1286	*86*	873	*67*	898	*54*
P495b avg	CM3	950	5.4	*0.5*	-	-	397	*193*	85	*56*	107	*27*	919	*115*	778	*58*	452	*41*

Run	SM	T (°C)	$D^{fluid/melt}$															
			S	±1σ	Sc	±1σ	V	±1σ	Ce	±1σ	Mo	±1σ	As	±1σ	Sb	±1σ	Pb	±1σ
P487a-avg	RDPM	1000	72	*12*	-	-	5.0	*4.0*	150	*47.9*	3.7	*1.9*	2.5	*1.7*	12	*5.1*	3.8	*1.8*
P498b avg	RDPM	1000	138	*20*	0.14	*0.11*	8.1	*2.7*	5.3	*1.2*	3.7	*2.6*	7.2	*4.1*	50	*14*	1.6	*1.3*
P486a-avg	RDPM	1050	69	*10*	4.1	*1.5*	9.5	*2.4*	46	*5.9*	0.34	*0.3*	1.6	*1.2*	6.6	*3.0*	1.9	*1.0*
P494b avg	RDPM	950	232	*40*	0.77	*0.59*	10	*1.9*	27	*1.9*	332	*88*	181	*62*	727	*130*	47	*4.5*
P490a-avg	RDPM	1000	159	*38*	3.9	*1.1*	13	*2.0*	7.4	*0.88*	82	*40*	287	*106*	794	*129*	50	*5.4*
P491a-avg	RDPM	1000	49	*14*	-	-	9.1	*1.4*	3.4	*0.48*	559*	*57*	897*	*103*	1732	*367*	74	*7.0*
P491b-avg	RDPM	1000	102	*11*	-	-	12	*1.5*	0.87	*0.43*	584*	*47*	909*	*86*	2406*	*278*	92	*6.4*
P497b avg	RDPM	1000	111	*16*	-	-	20	*4.5*	2.8	*0.55*	50	*12*	583	*362*	818	*402*	78	*8.8*
P494a avg	CM3	950	135	*22*	-	-	11	*2.6*	0.44	*0.30*	311*	*19*	147	*33*	428	*39*	21	*1.4*
P495b avg	CM3	950	172	*51*	-	-	8.0	*4.4*	0.79	*0.52*	20	*9.0*	23	*3.2*	86	*10*	5.6	*0.5*

uncertainties are 1 standard deviation of 30,000 Monte Carlo estimates of fluid trace element content

* elements are below detection limits in melt; calculation uses detection limit as maximum concentration of element in melt

Experiments were examined optically and by SEM and EPMA to determine the phase assemblage present in each charge (Table 4.2, Figure 4.2). The capsules all contained glass, small bubbles 5 – 10 μm in diameter and some combination of kyanite, quartz, ilmenite, garnet, clinopyroxene, titanite, Anh and/or Po. The identity of all phases was determined by their EDX spectra but quantitative compositional data for glass, garnet, clinopyroxene and Po (where large enough for analysis), was obtained by WDX (Table 4.3). Garnet and clinopyroxene were 5 – 10 μm in largest dimension. Kyanite and ilmenite were too small (~1 μm wide) to analyze without beam overlap with adjacent phases. Quartz formed generally large, 10 – 20 μm-wide, equant crystals. Po (< 1 – 15 μm wide) is the stable sulfur-bearing phase in all experiments containing graphite in the outer capsule, except in experiments P495b and P498b, which contained no graphite in the outer capsule. Anh is present as large crystals up to 20 μm in longest dimension in experiments P486a and P487a, both without graphite in the outer capsule.

4.4.2 Glass compositions

The glasses produced in my experiments are andesitic and similar in composition to S-bearing glasses from the pelite melting study of Canil and Fellows (2017; Figure 4.3). My glasses are considerably poorer in Ca than the melts from Skora *et al.* (2017; Figure 4.3) who used Ca-rich starting materials similar to calcareous black shale. I observe little difference between the melt compositions of PM and CM3 starting materials at 950ºC (the only temperature at which CM3 experiments were conducted; Table 4.3), consistent with their small differences in initial bulk Ca/Fe. Experiments that saturated in Po have melts that are richer in Ca and poorer in Fe (i.e. higher X_{Ca}) than those that saturate in Anh (Table 4.3, Figures 4.3 and 4.4a). Previously published analyses of S-bearing pelite

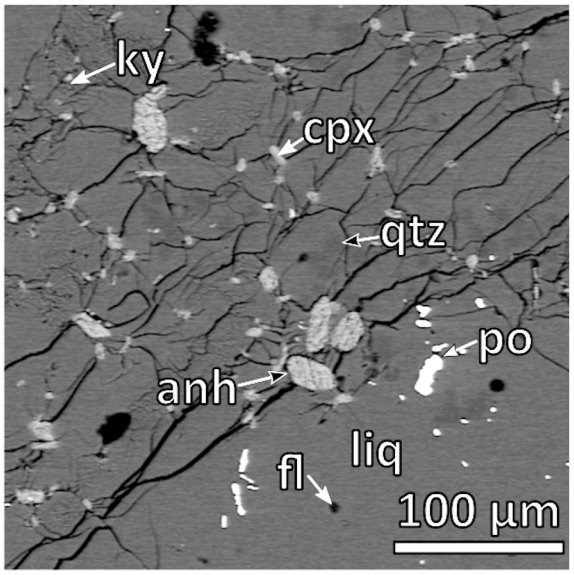

Figure 4.2: Back scattered electron image of a typical experimental product from this study showing the presence of Po, Anh, clinopyroxene (cpx), quartz (qtz), kyanite (ky) and bubbles (fl).

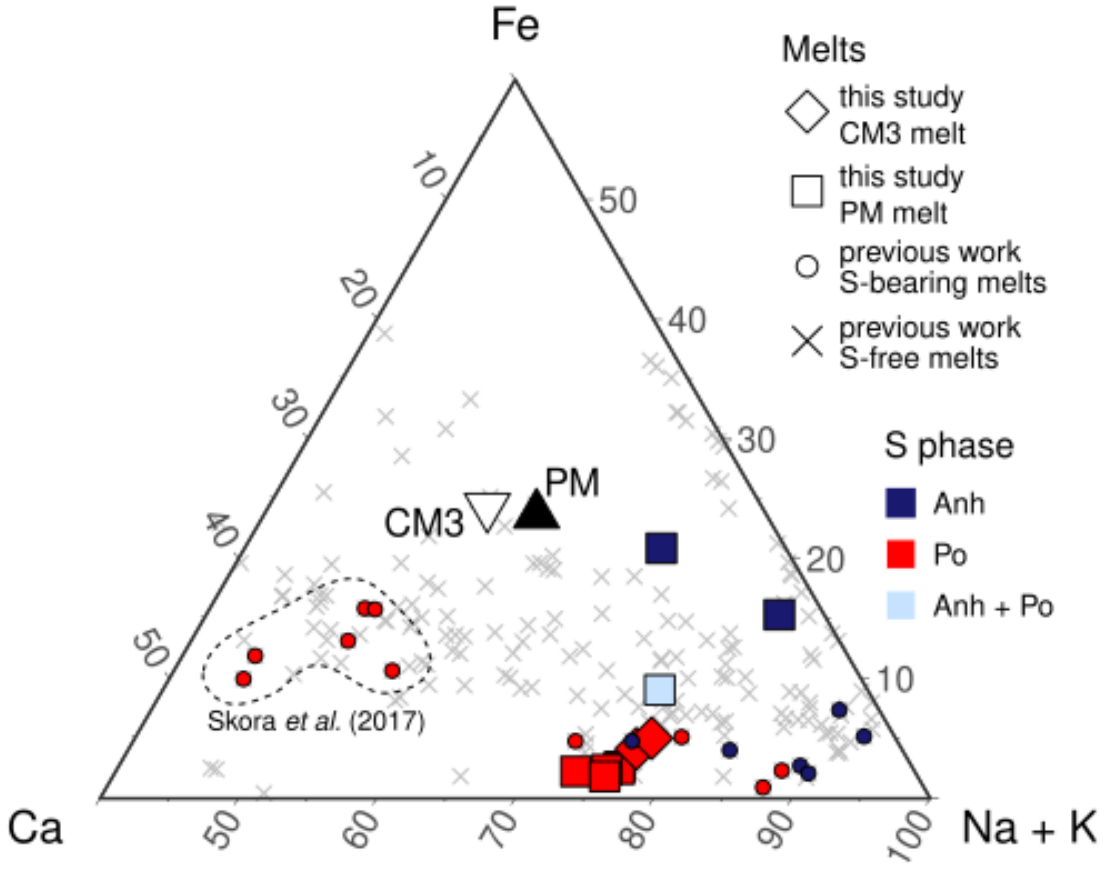

Figure 4.3: Molar Ca-Fe-(Na+K) ternary diagram showing the compositions of melts produced in the present study and in other sediment melting studies. Experiments in which S was present (the present study; Canil and Fellows, 2017; Skora *et al.*, 2017) are colour coded according to the identity of the S-bearing mineral that is observed.

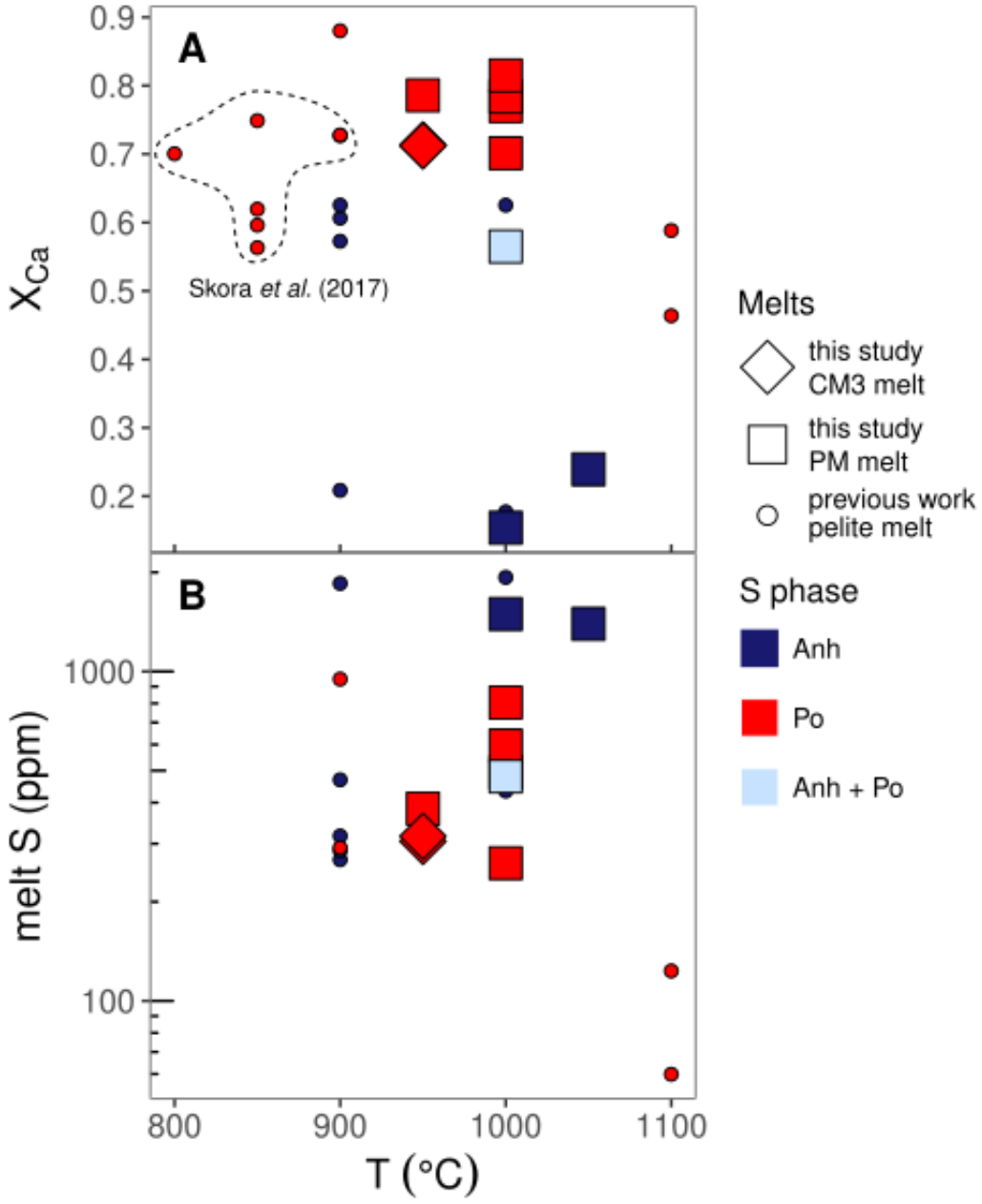

Figure 4.4: a) Variation of Ca and Fe content as represented by X_{Ca} (molar Ca/(Ca+Fe+Mg)) with temperature and identity of S-bearing mineral for experiments from the present study and from previous pelite melting studies in which S was present (Canil and Fellows, 2017; Skora *et al.*, 2017). b) Variation of melt S concentration with temperature and identity of S-bearing mineral in the present study and in the pelite melting study of Canil and Fellows (2017). As Skora *et al.* (2017) did not report their pelite melt S contents, their experiments are not shown in panel b.

melts (Canil and Fellows, 2017) show a similar variation of X_{Ca} with the presence of Anh or Po at a given temperature (Figure 4.4a).

Glasses from experiments in which Po is stable contain lower S than those in which Anh is stable (Figure 4.4b), as expected given the lower concentration of S in melts at Po saturation, compared to Anh saturation (Baker and Moretti, 2011, and references therein). Concentration of Na_2O, corrected as described above, varies from 3 – 3.4 wt.% across all melts. The corrected K_2O concentrations shows similarly small variation: 5.9 – 6.4 wt.% in PM melts and ~7.3 wt.% in CM3 melts. The H_2O content in the melts, inferred by difference of analytical totals from 100% , and using corrected K_2O and Na_2O concentrations, varies from 7.9 – 10.7 wt.%. The H_2O content is higher than expected given the amount of H_2O in the starting materials and the degree of crystallization (Tables 4.1 and 4.2), indicating the H_2O formation in the capsule from H_2 addition from the external capsule over the duration of each experiment.

Scandium in the glass is 0.5 – 1.5 times the concentration in the starting material, whereas V is up to 0.5 times lower in the glass than in the starting material, and there there appears to be no correlation with temperature or redox (Figure 4.5), with experiments using CM3 having lower concentrations of V and Sc than those using PM. The concentration of Ce, Mo, As, Sb and Pb in the glasses normalized to that in the starting material, varies depending on whether experiments were reduced or oxidized (Figure 4.5). In oxidized experiments, Mo, As, Sb and Pb are enriched and Ce is depleted in the glass, relative to reduced experiments. Furthermore, in reduced experiments, the chalcophile elements are in higher concentrations in the melt at 950ºC compared to 1000ºC (Figure 4.5a and b, respectively).

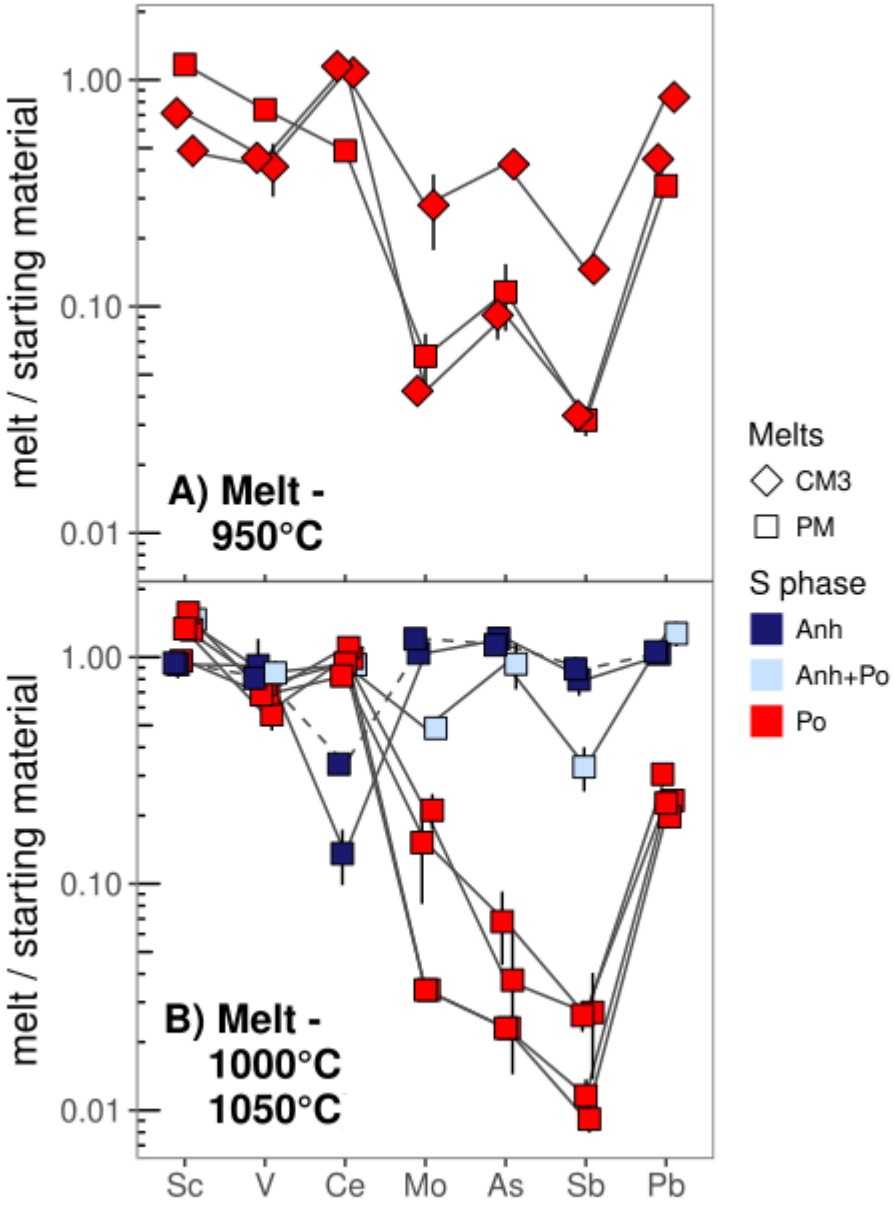

Figure 4.5: Melt concentrations of trace elements normalized to their bulk concentrations for experiments from the present study at a) 950ºC and b) 1000ºC and 1050ºC (dashed line). Symbol shapes represent the different starting materials used and are colour coded according to the observed S-bearing mineral.

4.4.3 Garnet, clinopyroxene and sulfide compositions

Clinopyroxene crystals are observed in both reduced, Po-bearing experiments of CM3 (P494a and P495b; Table 4.2) and show a small Ca-Tschermaks component (~0.05) and $X_{hedenbergite}$ of ~0.2. Using these compositions with the CASP oxygen buffer (Canil and Fellows, 2017), indicates a maximum f_{O2} of ΔFMQ = 0.80 (P494a) and 0.56 (P495b). Two experiments of PM starting material (P487a and P494b) saturated in garnet (Table 4.2). The garnet in the oxidized, Anh-bearing experiment P487a has high almandine (0.77), moderate pyrope (0.16) and low grossular (0.07) components, indicating a minimum f_{O2} of ΔFMQ = 0.59 using the GAP oxygen buffer (Canil and Fellows, 2017). Po-bearing experiment P494b shows almost end-member grossular garnet ($X_{grossular}$ = 0.97), indicating a maximum f_{O2} of ΔFMQ = -0.60 using the GAP buffer. Po was only large enough for microprobe analysis in two experiments, P491b and P494a, and is $Fe_{0.84}S$ in both experiments (Table 4.3). None of the crystalline phases present in my experiments were large enough for trace element analysis by LA-ICP-MS.

4.4.4 Equilibrium

I have assessed equilibrium in these experiments as follows:

1. The measured S and trace element concentrations in the glasses show low variability in all experiments (Table 4.3), suggesting that diffusion of S and trace elements in the melts approached equilibrium.
2. The major element concentration in glasses from experiments carried out at 1000ºC and 3 GPa with the PM starting material changes very little for experiments of 24 hours (P487a) and 48 hours (P498b) duration.

Given that this study focuses on the fluid-melt system where diffusion is rapid, I am confident that my experiments are at equilibrium. However, the phase assemblages produced in my experiments deviate from the eclogitic phase assemblages reported by Mann and Schmidt (2015) and Tsuno and Dasgupta (2011) for their experiments whose liquid compositions I have used as starting materials and this requires some comment. The melt in Mann and Schmidt's (2015) experiment BE1116 at 1000ºC and 3 GPa, the basis for the PM starting material, is in equilibrium with fluid, quartz/coesite + kyanite + rutile + garnet + clinopyroxene. Tsuno and Dasgupta's (2011) melt from experiment GS58, at 1050ºC and 3 GPa, was the basis for the CM3 starting material and is in equilibrium with clinopyroxene + garnet + quartz/coesite and a CO_2 vapour. The phase assemblage I observe in my experiments is melt + fluid ± kyanite ± quartz/coesite ± garnet ± clinopyroxene ± ilmenite ± Anh ± Po, and a single crystal of titanite (in P494b). One explanation for the differences between phase assemblages is that I have used liquid compositions as the starting materials, thus the bulk compositions may simply be too Mg-poor to saturate in clinopyroxene, except at 950°C. In addition to the starting materials being Al-poor, garnet is a notoriously difficult phase to nucleate and grow in experiments which may explain why only two of my experiments saturate in garnet. Furthermore, the PM melts have EMPA totals that are ~5 wt.% lower than BE1116 (Mann and Schmidt, 2015) indicating, albeit in a coarse way, that my glasses contain more H_2O likely due to the use of an external H_2O source. The Tsuno and Dasgupta (2011) experiments were anhydrous and CO_2-bearing whereas the CM3 starting material is deliberately hydrous and CO_2-free, in order to increase the melt volumes produced. The increased H_2O content of the bulk compositions used in this study will depress the liquidi. Furthermore, my

starting materials contain S and slightly more CaO and FeO^{tot} than the original liquid compositions they are based on. Thus, the exact equilibrium solid phase assemblages observed by Mann and Schmidt (2015) and Tsuno and Dasgupta (2011) may not necessarily apply to my experiments.

4.5 Discussion

4.5.1 Chalcophile elements in melt and fluids

Oxidized, Anh saturated experiments show higher melt S content than reduced, Po saturated ones (Figure 4.4b), in agreement with much previous work (e.g. Baker and Moretti, 2011). My results also indicate that fluids carry more S (Figure 4.6) and that $D^{fluid/melt}$ S (Figure 4.7a) is higher for oxidized rather than reduced experiments, similar to observations by Jégo and Dasgupta (2014) in the basalt system (Figure 4.7b). Estimates for $D^{fluid/melt}$ S in rhyolite by Scaillet *et al.* (2006) at 150 MPa and 800ºC, vary from ~50 to 500, and increases with peralkalinity, f_{O2} and bulk S. The SMN experiment series by Scaillet *et al.* (2006) is similar in bulk composition to my experiments and have $D^{fluid/melt}$ S = 200 – 350, within error of my results (Figure 4.7b). Keppler's (2010) results for the haplogranite system at 850ºC, 50 – 300 MPa show $D^{fluid/melt}$ S decreasing from ~500 at the Co-CoO oxygen buffer to ~50 at 1 log unit above the Ni-NiO buffer.

The concentration of other chalcophile elements in fluids (Figure 4.8) and their $D^{fluid/melt}$ values (Figure 4.9) also appears to be controlled primarily by redox. The chalcophile elements show lower concentrations in the fluid (Figure 4.8), 1 – 5 times lower than the bulk concentration in oxidized compared to reduced experiments (up to 20 times greater than bulk concentration). In reduced experiments $D^{fluid/melt}$ for the chalcophile elements is 1 – 2 orders of magnitude higher than for oxidized experiments (Figure 4.9). For the

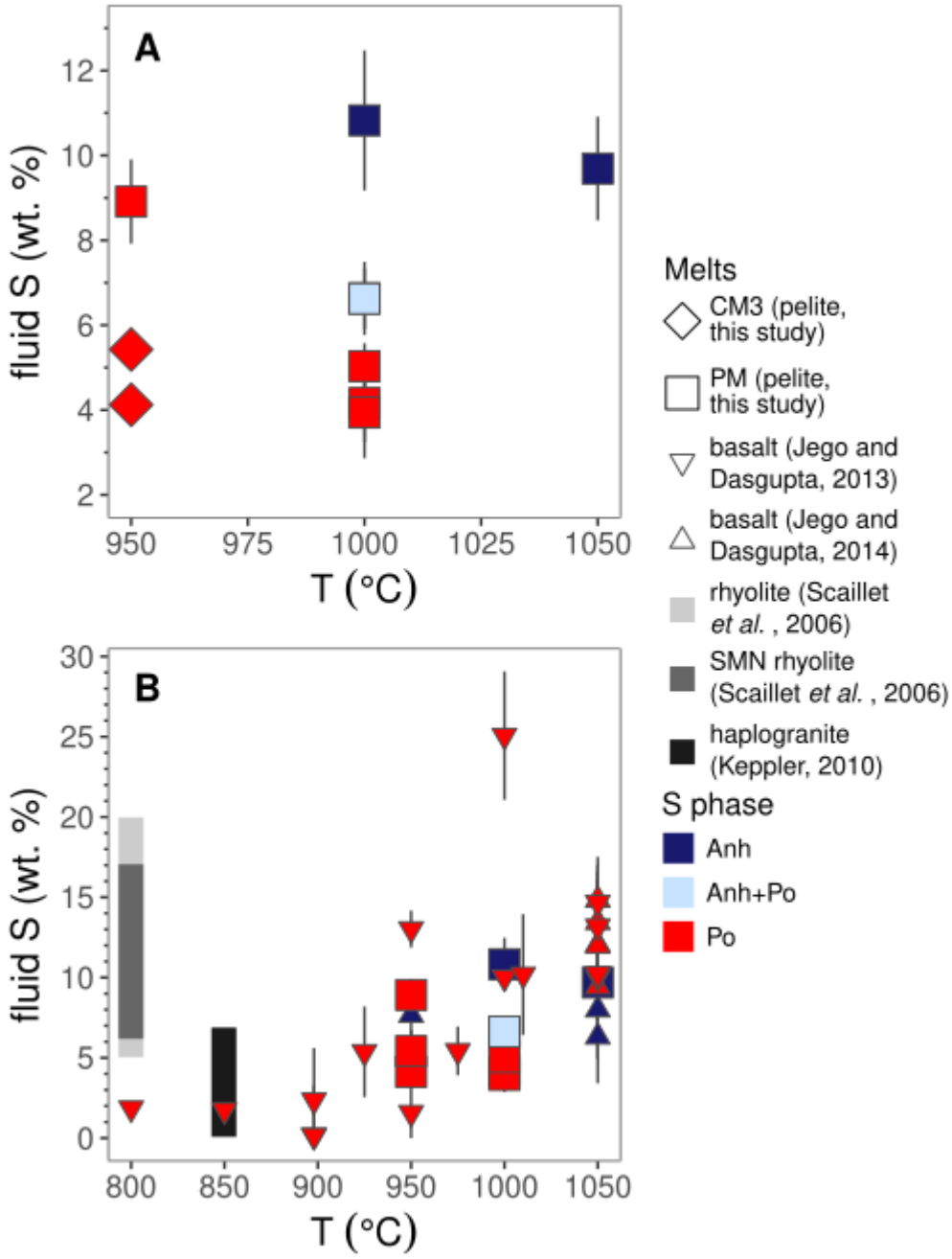

Figure 4.6: a) Fluid S concentrations in the present study as a function of temperature. Symbol shapes represent the different starting materials used and are colour coded according the S-bearing mineral present. b) Results from the present study in the context of previous measurements of fluid S concentration (Scaillet *et al.*; 2006, Keppler, 2010; Jégo and Dasgupta, 2013; 2014).

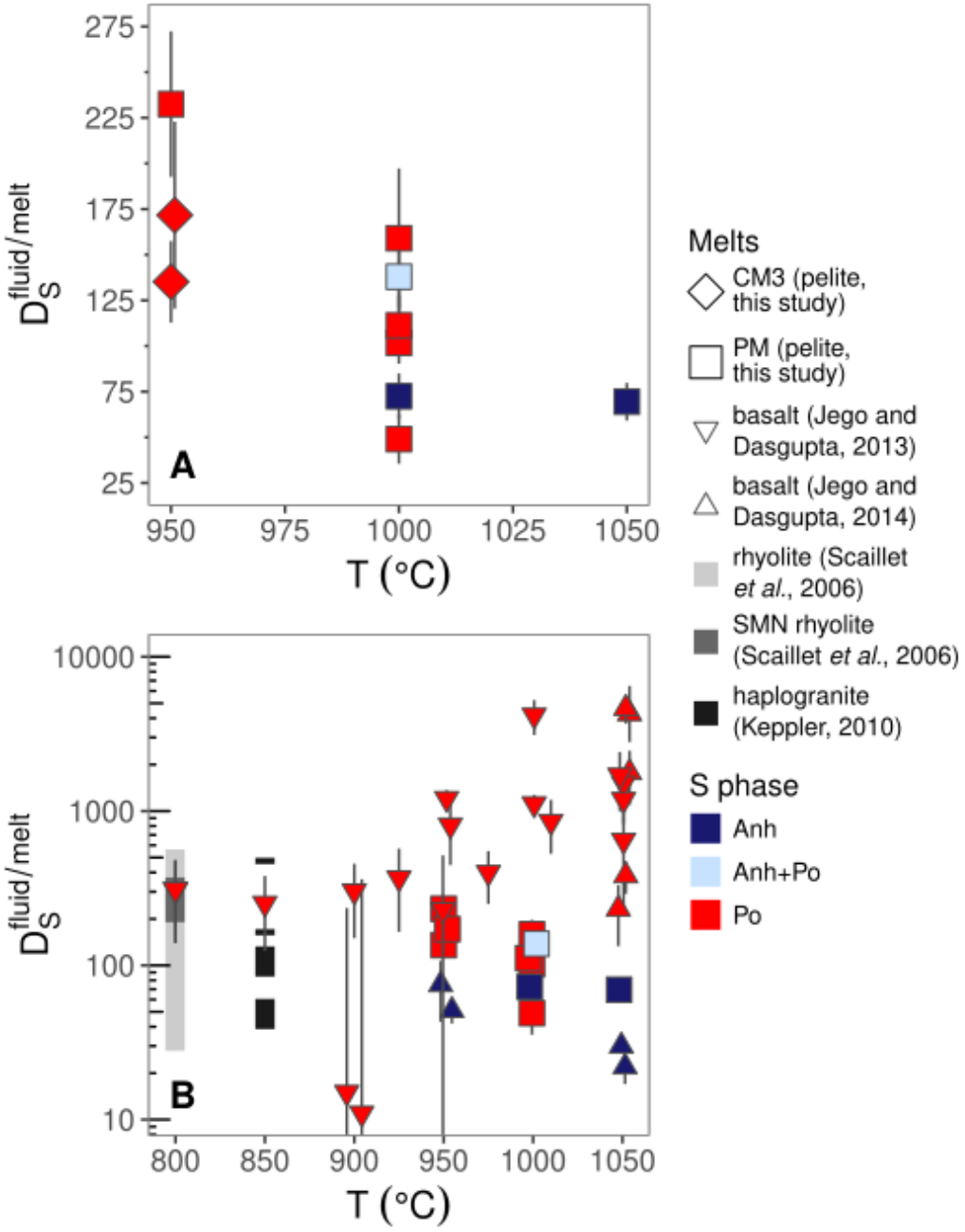

Figure 4.7: a) $D^{fluid/melt}$ S calculated in the present study as a function of temperature. Symbol shapes represent the different starting materials used and are colour coded according the S-bearing mineral present. b) Results from the present study shown in context of previous measurements of $D^{fluid/melt}$ S (Scaillet *et al.*, 2006; Keppler, 2010; Jégo and Dasgupta, 2013; 2014).

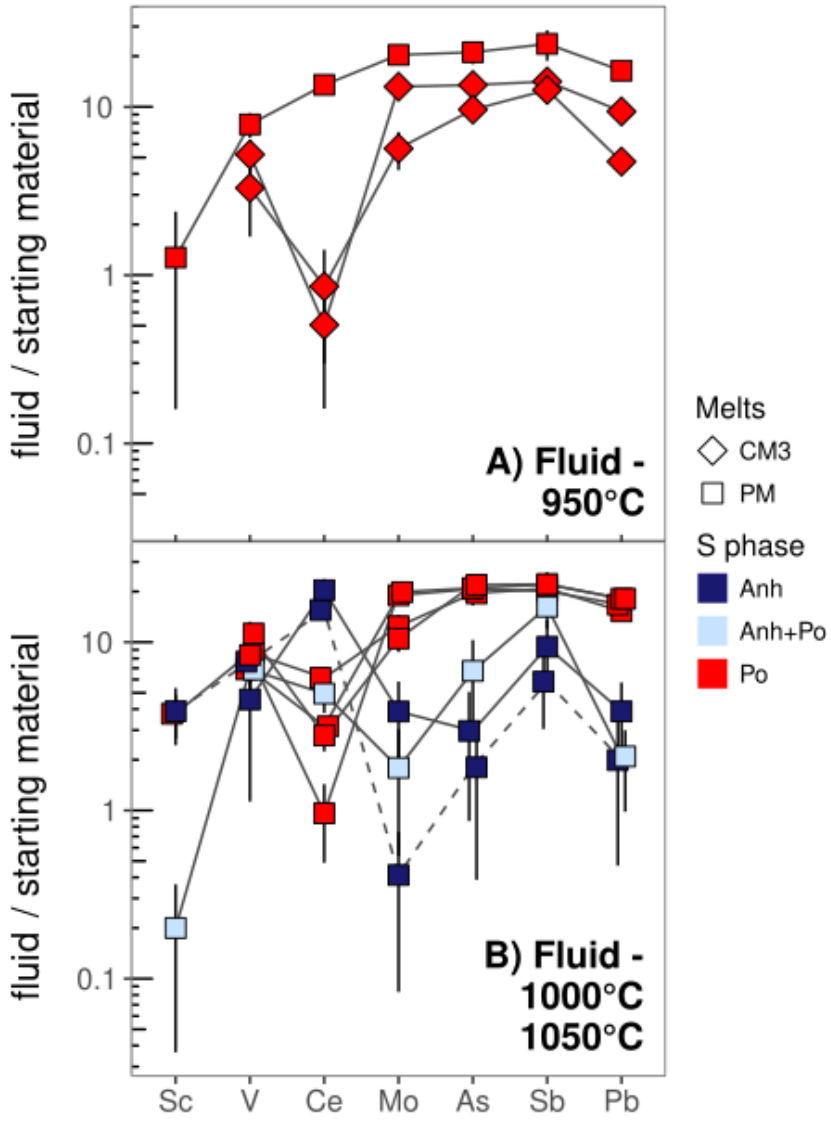

Figure 4.8: Mass balanced fluid concentrations of trace elements normalized to their bulk concentrations for experiments from the present study at a) 950ºC and b) 1000ºC and 1050ºC (dashed line). Symbol shapes represent the different starting materials used and are colour coded according to the observed S-bearing mineral.

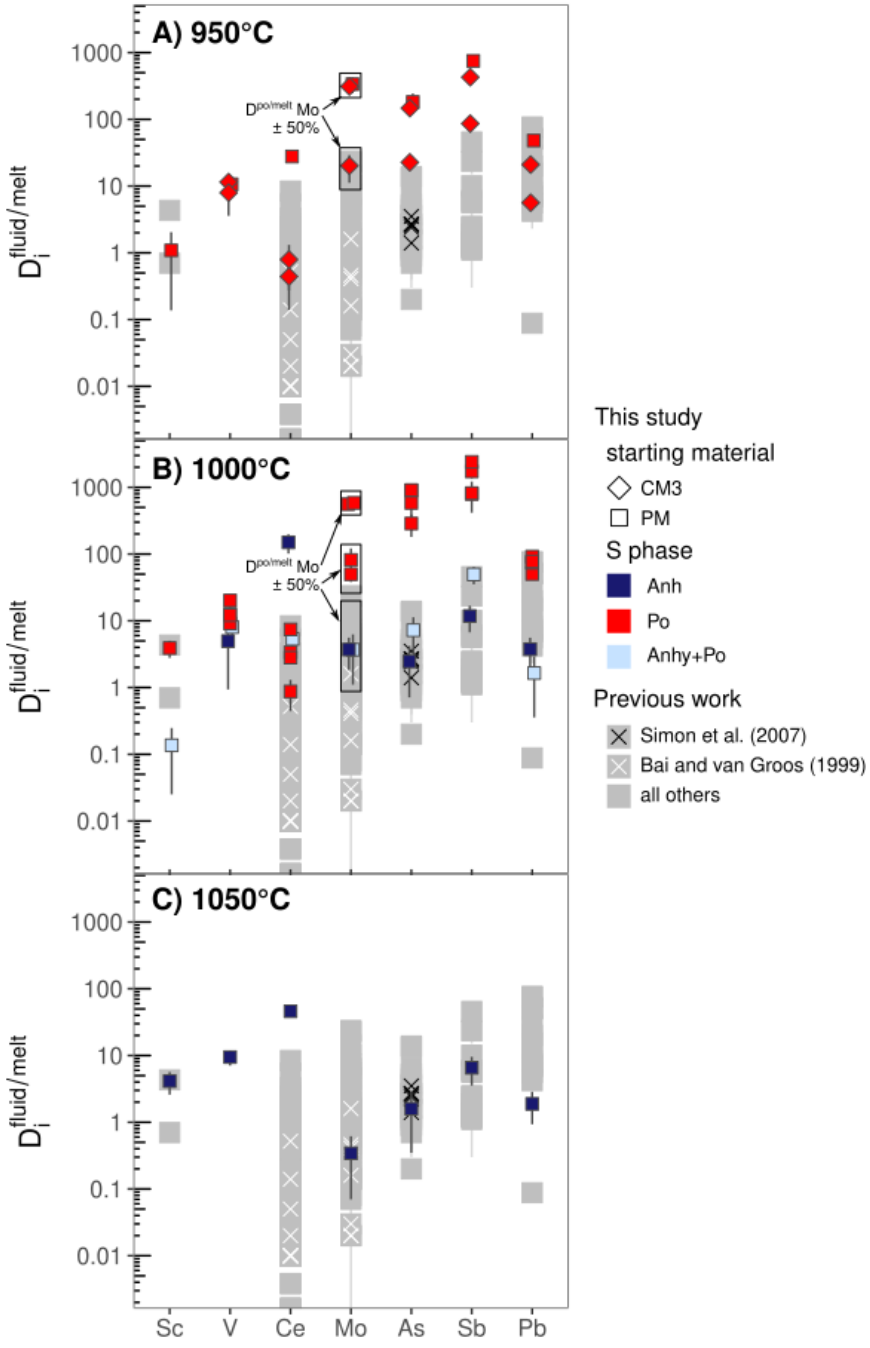

Figure 4.9: $D^{fluid/melt}$ values for the trace elements in the present study at a) 950, b) 1000 and c) 1050°C shown with previous estimates. Data are from Flynn and Burnham (1978), Webster *et al.* (1989), Keppler and Wyllie (1991), Keppler (1996), Bai and van Groos (1999), Reed *et al.* (2000), Simon *et al.* (2007) and Zajacz (2008). Results for different starting materials used in the present study are represented by different symbol shapes and are colour coded according to observed S-bearing mineral. The boxes around data points for Mo in Po-bearing experiments in panels a and b represent the variation in $D^{fluid/melt}$ expected by changing $D^{Po/silicate\ melt}$ Mo by ± 50%.

experiments in which As, Mo and Sb are below analytical detection limits in glass I calculated the fluid concentration and $D^{fluid/melt}$ using the detection limit as a maximum melt concentration.

Arsenic and Mo show up to three orders of magnitude difference in $D^{fluid/melt}$ between reduced and oxidized melts. In the case of Mo, I estimated the contribution of Po to the overall Mo budget using the partition coefficient (35 ± 3; Table 4.4) from Mengason *et al.* (2011). I tested the dependence of the calculated $D^{fluid/melt}$ on the exact choice of $D^{Po/silicate\ melt}$ for Mo by varying the latter by ± 50%. I find that 50% variation in $D^{Po/silicate\ melt}$ changes $D^{fluid/melt}$ by less than the error reported in Table 4.5, except for P498b. Experiment P498b co-saturates in Anh and Po and $D^{fluid/melt}$ changes by up to an order of magnitude when varying $D^{Po/silicate\ melt}$ by 50% (Figure 4.9b), reflecting the high Mo concentration in glass, thus the high Mo concentration in Po estimated using $D^{Po/silicate\ melt}$.

The $D^{Po/silicate\ melt}$ values from Stimac and Hickmott (1994; Table 4.4) indicate that Po will only carry a small fraction of the As and Pb budget in high silica melts ($D^{Po/silicate\ melt}$ As and Pb = ~2) such as those in my experiments. I have not accounted for As and Pb in Po in the mass balance, however even large variations of $D^{Po/silicate\ melt}$ for As and Pb will not significantly change the calculated $D^{fluid/melt}$ values. To my knowledge, there are no $D^{Po/silicate\ melt}$ estimates for Sb in rhyolite melts, thus my $D^{fluid/melt}$ estimates for Sb, As and Pb are maxima.

4.5.2 Lithophile trace elements in fluids

Scandium and V each show large overlap in melt concentrations in all experiments (Figure 4.5, Table 4.3), indicating the insensitivity of these elements' partitioning behaviour to redox. Scandium and V are typically incompatible in fluids (e.g. Green and

Adam, 2003; Kessel *et al.*, 2005b) and the compatible $D^{fluid/melt}$ values I report (Table 4.5, Figure 4.9) requires some explanation. Of the major hosts for Sc and V in my experiments (melt and, where present, garnet, clinopyroxene and Fe-Ti oxides) only the melt could be analyzed by LA-ICP-MS. I estimated the Sc and V concentrations of the minerals using published $D^{mineral/melt}$ (Table 4.4). In the case of Sc, all but two mass balanced fluid concentrations (Table 4.5) are negative or within uncertainty of zero, implying that melt, garnet and/or clinopyroxene indeed carry all of the Sc budget in the system, and that Sc is fluid incompatible in those experiments. Two experiments show $D^{fluid/melt}$ Sc up to 4.0 ± 1.5 (1σ). My results also show that $D^{fluid/melt}$ V is between 5 and 20. In general, the low modes of crystalline phases in which Sc and V are compatible in these experiments indicates that these phases cannot carry large absolute amounts of Sc and V. The $D^{mineral/melt}$ values for clinopyroxene, garnet and/or Fe-Ti oxide (Table 4.4) would need to be higher by factors of at least 20 for the calculated to $D^{fluid/melt}$ to be less than one. Presuming that Sc and V are indeed incompatible in the fluids present in these experiments, I conclude that the $D^{fluid/melt}$ for Sc and V calculated by my method is correct to within a factor of 4 and 20, respectively. Alternatively, my data may show that V has some small fluid compatibility.

My results show that Ce behaves in an opposite manner to the chalcophile elements, being enriched in reduced melts and depleted in oxidized melts (Figure 4.5). Natural Anh is known to contain up to 50 ppm Ce (Baumer *et al.*, 1997) and the only measured $D^{Anh/melt}$ for Ce that I am aware of is 2.7 (Luhr *et al.* 1984). Thus, it is likely that some of the depletion in Ce in oxidized melts is due to its inclusion in Anh. As discussed above for As and Pb in Po, the small $D^{Anh/melt}$ for Ce, together with the low Ce concentration in

the melt and the low mode of Anh (< 2 wt.%) in my experiments means that only a small portion of the Ce budget will be carried by Anh and the melt, resulting in high concentrations of Ce in the fluid and high $D^{fluid/melt}$. Conversely, when Anh is not present (i.e. in reduced melts), Ce is higher in the melt and it accounts for a larger portion of the Ce budget, resulting in lower Ce fluid concentrations and $D^{fluid/melt}$. As above for the chalcophile elements, the assumptions made in calculating the fluid compositions mean that the $D^{fluid/melt}$ values reported here are maxima only.

4.5.3 Effect of temperature on $D^{fluid/melt}$

My experiments allow me to make limited observations about the effect of temperature on trace element fluid-melt partitioning. The $D^{fluid/melt}$ estimates for trace elements show little difference outside of uncertainty for all trace elements except Ce in oxidized experiments at 1000ºC and 1050ºC where Anh is the only S-bearing mineral. Cerium partitions more strongly into fluid in oxidized experiments at high temperature ($D^{fluid/melt}$ = 150 ± 48 at 1050ºC vs. 46 ± 5.9 at 1000ºC). Directly comparing $D^{fluid/melt}$ between reduced, Po-bearing experiments at 1000ºC and 950ºC is complicated by the range of values I observe, however considering the average of $D^{fluid/melt}$ estimates in these experiments and the propagated uncertainties is useful. At 1000ºC, the average $D^{fluid/melt}$ for As (669 ± 134), Mo (319 ± 43), Sb (1437 ± 208) and Pb (73 ± 4) are higher than at 950ºC (117 ± 24, 223 ± 31, 422 ± 47 and 25 ± 2, respectively). In reduced experiments, Ce has lower $D^{fluid/melt}$ values at 1000ºC (4 ± 0.3) than at 950ºC (10 ± 1).

4.5.4 Comparison to published studies

Given the interest in vapour and brine as a means of transporting chalcophile elements in the shallow subsurface of ore-deposits, there are a great many estimates of trace

element partitioning in such systems. In contrast, there are few fluid-melt partitioning estimates from naturally occurring fluid-silicate melt inclusions or from experiments and I have compiled the previous estimates that I could obtain in Figure 4.9. Comparisons of my results with the previously published experimental $D^{fluid/melt}$ estimates must necessarily be equivocal for a number of reasons: 1) the published $D^{fluid/melt}$ values apply to the low pressure entrapment of fluid-melt inclusions (P = 0.125 – 0.4 GPa; T = 750 – 1040ºC) whereas my experiments are at considerably higher pressure (3 GPa); 2) the fluid phases in previous experiments vary in salinity and this is known to strongly impact fluid-melt partitioning (e.g. Zajacz, 2008), whereas my experiments do not include Cl or other halogens; 3) with the exception of Bai and van Groos (1999) and Simon *et al.* (2007), previous fluid-melt partitioning studies do not include the effect S. Bai and van Groos (1999) conducted nine Cl- and S-bearing experiments with haplogranite melts and show that Mo is incompatible in fluids at less than 0.3 GPa ($D^{fluid/melt} < 0.4$) and fluid compatible above 0.4 GPa ($D^{fluid/melt} = 1.6$). Those authors also report that Ce is incompatible in all their S-bearing experiments ($D^{fluid/melt} < 0.5$) . Bai and van Groos' (1999) experiments are significantly different from mine being undersaturated in Anh and Po.

The S-bearing experiments of Simon *et al.* (2007) are Po saturated and the average $D^{fluid/melt}$ As of 3 ± 1 reported for their experiments at 800ºC and 0.12 GPa is 2 – 2.5 orders of magnitude lower than the average reported in this study for reduced experiments at 950ºC (117 ± 2) and at 1000ºC (669 ± 134) at 3 GPa. As the major element compositions of the melts in Simon *et al.* (2007) and this study are similar, this difference may be due to effects of P, T and/or salinity. I rule out P and salinity differences as the cause as

decreasing salinity negatively effects the fluid-melt partitioning of chalcophile elements and the effects of pressure are minor (Keppler, 1996). The difference in temperature most likely accounts for the differences observed in $D^{fluid/melt}$ As between Simon *et al.* (2007) and the present work. As discussed above, a change in temperature from 1000ºC to 950ºC lowers the average $D^{fluid/melt}$ of As by over half an order of magnitude, thus the 150ºC difference in temperature between Simon *et al.* (2007) and this study may account for at least a portion of the difference in $D^{fluid/melt}$ As.

4.5.5 Application to Mo/Ce systematics in the Lesser Antilles arc

My experiments show a large range in melt Mo/Ce (Figure 4.10a) related to redox. Low melt Mo/Ce is caused by simultaneously low Mo and high Ce melt concentrations when Po rather than Anh is present. Skora *et al.* (2017) find a similar change in Mo/Ce in their melting experiments of sediment analogues, although they also see the effect of phases like epidote, monazite and carbonate in which Ce is compatible. Those authors combined their experimental results with Mo stable isotope systematics (Freymuth *et al.*, 2015; 2016; König *et al.*, 2016) to determine that fluid or melt associated with subducted black shales, marine clay and terrigenous sediment can produce the high $\delta^{98/95}$Mo and low Mo/Ce of arc magmas in the Lesser Antilles. My results allow me to further investigate the source of the low Mo/Ce in the Lesser Antilles by having determined the contrasting mobility of this element pair in reduced and oxidized experiments. High Mo/Ce is carried by the melt phase in oxidized Anh bearing experiments (Figure 4.10b), but when Po is stable (i.e. in reduced experiments) only the fluid phase will carry this signature. Thus, if Po breakdown in oxidized conditions is the source of Mo in the Antilles arc as postulated

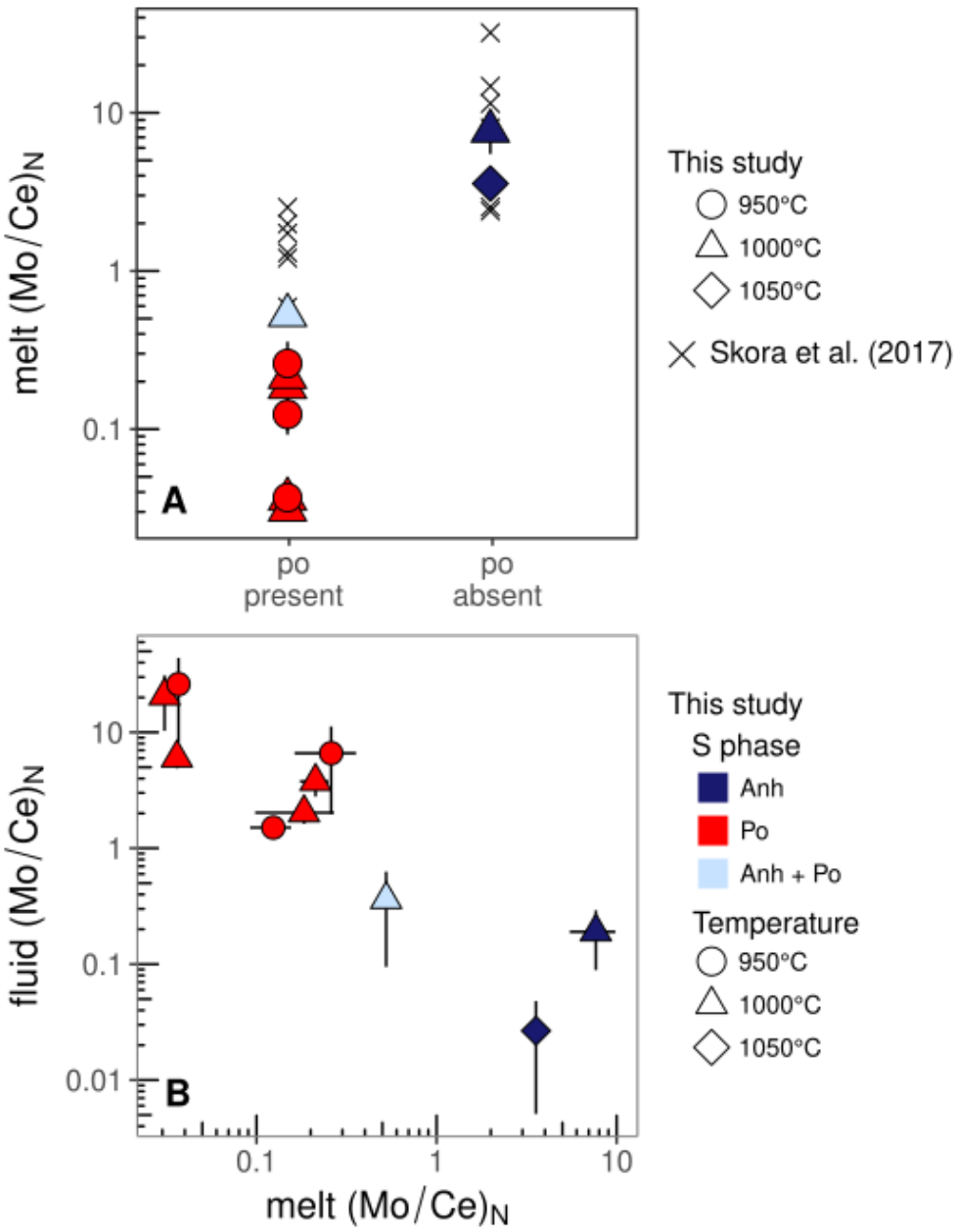

Figure 4.10: a) Melt Mo/Ce variation with presence or absence of Po in the present study and in Skora *et al.* (2017). b) Mo/Ce in the fluid and melt in the present study. Symbol shapes represent different temperatures and colour coded according to observed S-bearing mineral. Error bars are 1σ.

by Skora *et al.* (2017) on the basis of their experiments, melts and not fluids must be the agent of Mo and Ce transfer into the sub-arc mantle.

4.6 Conclusions and implications

The results presented in this chapter have shown that chalcophile trace elements can be mobilized in fluids in equilibrium with sediment partial melts and that this partitioning is particularly sensitive to f_{O2} as indicated in this study by the stability of Po. The concentration of chalcophile elements is low in reduced melts where Po is stable, thereby decreasing the portion of the trace element budget carried by the melt. As Po is a minor phase in melts and has a relatively low $D^{Po/silicate\ melt}$ for the chalcophile elements I consider (Table 4.4), it can only be a minor carrier of these chalcophile elements in the system and the remainder of the chalcophile element budget is carried in the melt and fluid phases. This work shows that Mo, As, Sb and Pb are fluid mobile at all investigated conditions and, unexpectedly, that their fluid partitioning is enhanced by melting at reduced conditions where sulfide is stable. I emphasize here that the $D^{fluid/melt}$ values calculated herein are maxima, particularly for the chalcophile elements, as the concentration of these elements in the sulfide phase has only been estimated and has not been analyzed directly. Although not studied here, for elements with very high $D^{Po/silicate\ melt}$ (i.e. > 10,000; e.g. Ir, Pd; Peach *et al.*, 1994) their concentration in Po must be determined to accurately mass balance their concentration in the fluid.

Fluids in equilibrium with reduced, Po-bearing sediments will be enriched in chalcophile elements and these fluids can endow the arc mantle in S and chalcophile elements without necessarily oxidizing the arc mantle. This resolves the paradox implied by models that seek to endow the arc mantle with high chalcophile element loads in

oxidized melts (e.g. Evans and Tomkins, 2011), but which are constrained by V/Sc in primitive arc lavas indicating that the sub-arc mantle is no more oxidized than MORB mantle (Lee *et al.* 2005). An arc mantle preconditioned by reduced, chalcophile enriched fluids can host elevated chalcophile element concentrations in sulfides. This stored endowment of S and chalcophile elements can be later transferred to ascending oxidized melts or fluids in which sulfide is broken down. The resulting melts could then carry high chalcophile element concentrations upward to shallow levels of arcs where they eventually undergo fractionation and/or vapour/brine separation to further concentrate the chalcophile elements in a fluid phase. The chalcophile elements carried by such melts or fluids may later be further concentrated by the processes that form ore deposits. Such a multi-stage process of preconditioning the arc mantle in chalcophile elements by reduced fluids and then releasing the chalcophile elements by later oxidized melts or fluids transiting the arc mantle, fits well with the multi-stage "redox yo-yo" process envisioned by Nebel *et al.* (2015) to explain the observed Fe isotope composition of arc lavas.

Finally, the results presented here also allow me to fine tune the interpretation of Mo/Ce ratios in arcs like the Lesser Antilles, where heavy $\delta^{98/95}$Mo and unradiogenic Pb isotopes have been previously used to isolate the source of elevated Mo in arc lavas to subducted black shales (Freymuth *et al.* 2016; König *et al.*, 2016) whose low Ca/Fe favour sulfide stability (Canil and Fellows, 2017). The results presented here indicate that the elevated Mo concentrations observed in arc lavas from the Lesser Antilles could most effectively have been delivered by melts, not fluids.

Chapter 5.
Conclusions

5.1 Research overview and significance

The detailed structure of arcs has been documented from rare, well-exposed sections like the Talkeetna and Kohistan (DeBari and Coleman, 1989; Jagoutz *et al.*, 2007) however extending those findings to incompletely exposed arc sections is nessecarily tenuous. One example of an incompletely exposed arc is the Bonanza arc on Vancouver Island, Canada, which also provides a unique opportunity to study an island arc emplaced on pre-existing non-oceanic crust. The work I presented in Chapter 2 shows that garnet must have been a fractionating phase in the Bonanza arc and agrees well with independent estimates of the Bonanza arc thickness from seismic studies and my structural reconstruction. This inference of a garnet-bearing lower crust negates a major difference between it and the coeval Talkeetna arc (DeBari *et al.*, 1999) and leads to the tantalizing possibility that these arcs may have been part of a single arc front in Jurassic time. In this interpretation, the presence of pre-Jurassic substrate in the Bonanza arc section but not the Talkeetna may simply relfect along-strike variations, such as observed in the modern-day Aleutian arc. A further consequence of allowing the correlation of the Bonanza and Talkeetna arcs is that the large displacement observed between these arc sections in the present day requires movements of up to 1000 km along strike-slip faults (e.g. Plafker *et al.*, 1989), and thus provides further insight into accretion processes by which continents are thought to grow.

As arcs mature and thicken, their magmas become more alkaline (e.g. Green, 1980) and thick arcs are associated with PCD. The experimental work presented in Chapters 3 and 4 are each a significant contribution to our understanding of how chalcophile elements

move in arc systems. In Chapter 3 I show that the S concentration of melts saturated in sulfide increases with alkalinty. Thus, as arcs mature, their magmas will be able to carry greater amounts of S and recognition of this variability permits a finer-grained understanding of the geologic cylcing S at convergent margins. An extended implication of this work is that alkaline magmas from other tectonic settings can also carry more S than previously recognized with numerous implications. For example, it may thus be possible that alkaline magmas from the early stages of intraplate volcanism could release more S gases into the atmosphere than previously estimated, with potentially significant consequence for global climate (e.g. McLinden *et al.*, 2016).

Although the association of porphyry Cu deposits with arcs has long been regcognized, the ultimate source of those chalcophile elements is enigmatic. Chalcophile elements are known to be compatible in fluids at upper crustal pressures (0.125 − 0.4 GPa) and the results of Chapter 4 show for the first time that this remains the case at the high pressure conditions of sediment melting (3 GPa; ~100 km depth) beneath arcs. In particular, we see that the Dfluid/melt of the chalcophile elements considered in Chapter 4 are up to three orders of magnitude greater at reduced conditions (i.e. where sulfide is stable), compared to oxidized conditions. This work, therefore, shows that the chalcophile element endowment of the sub-arc mantle may be effectively delivered by fluids associated with reduced sediments. Importantly such fluids can enrich the arc mantle in chaclophile elements without oxidizing it, thus satisfying constraints from V/Sc systematics showing the sub-arc mantle has similar fO2 as MORB (Lee *et al.*, 2005).

5.2 Future research directions

The work presented here opens up further avenues of questioning for future research. Foremost among the outstanding issues on the Bonanza arc is the bi-modal age distribution reported in Chapter 2. At present there are very few dated rocks for which there are also geochemical data available and the dataset of such paired data should be expanded in future work. Samples with Paired geochronology and geochemistry data are crucial for determining if the different age populations observed are also associated with chemical differences, which will help better elucidate the evolution of this arc. For example, with such data, it would be possible to test whether the influence of garnet fractionation and/or alkalinity of the Bonanza arc rocks increases with time, as would be expected for a thickening arc. Given the bi-modal distribution of the Bonanza arc ages, it may also be possible that further geochemical and age data may reveal that what we presently refer to as the Bonanza arc actually represents a pair of temporally distinct arcs. Other potential inquiries include determining whether ultramafic rocks found near Kennedy Lake, Vancouver Island, are part of the Bonanza arc (Debari *et al.*, 1999), and whether the metamorphosed calc-silicate septa in the Talkeetna plutonic rocks represent pre-Jurassic basement (Burns, 1985), both of which may strengthen the correlation between the Bonanza and Talkeetna arcs.

The results in Chapter 3 indicate an apparent limit to increasing SCSS solely by increasing alkalinity. Given the absence of significant variations in the other main parameters known to control SCSS (e.g. temperature, melt FeO and SiO2 content), this is an important finding to pursue as it implies that the number of non-bridging oxygen is not the only parameter to control SCSS. In depth Raman microscopy studies may help in this endeavor by determining how the S melt environment and/or S redox change with

increasing alkalinity. Another worthwhile research direction is examining whether the form of the empirical SCSS models examined in Chapter 3 may be improved. The empirical models at present are essentially linear and thus unable to resolve the nearly parabolic shape of the model misfits with increasing alkalinity. An apparently systematic error like this points to a fundamental shortcoming in the assumptions underlying the mode. Resolving these systematic errors with an improved model form will ultimately further uncover the nature of S dissolution in silicate melts.

In Chapter 4, I calculated Dfluid/melt values for the chalcophile elements by mass balance, but these values are maxima only due to the assumptions made about the pyrrhotite contribution to the chalcophile element budget. Directly measuring the chalcophile element concentrations in pyrrhotite and using these in the mass balance calculation will provide more accurate Dfluid/melt estimates and this is imperative if the Dfluid/melt for very highly sulfide compatible elements (e.g. Ir, Pd) are to be determined by mass balance. An alternative approach is to analyze the experimental run products as a whole by solution ICP-MS to give the chalcophile element concentration in the glass and mineral phases in bulk. Thus method avoids the need to accurately determine the non-fluid contributions to the chalcophile element budget in the system. The fluid composition can be more accurately determined by mass balance in this manner, providing the fluid phase can be extracted from the run products, perhaps by crushing, washing and drying, prior to analysis. Yet another extension of this work is to examine the effect of Cl on fluid-melt partitioning, which is known to have strong positive impact at low pressure.

The results presented in Chapter 4 also show that the fluid-melt partitioning of chalcophile elements is opposite to that of Ce in oxidized and reduced conditions but the reasons for this requires further investigation. Possible reasons for this behaviour include enhanced fluid solubility of reduced S ligands, which is testable with S-free experimental runs, or reduced ionic species of the chalcophile elements themselves. The latter possibility is difficult to test without measuring the fluid itself, thus a fruitful extension of this work will be to trap the fluid within synthetic fluid inclusions for direct analysis. Not only would such experiments allow direct testing of the redox dependent patterns of variation of fluid compositions and Dfluid/melt presented in this work, but will also allow for direct measurement of speciation of the elements and/or the complexes that they form.

5.3 Concluding remarks

Chemical similarities between lavas observed at volcanic arcs and the bulk continental crust are a strong indication that continental crust is produced at convergent tectonic margins (Taylor, 1977). Although continental crust is destroyed over geologic time by sediment subduction, continental rocks are preserved from all periods of Earth's history, from over four billion years ago to the present. The continents thus carry the longest running record of geologic processes on our planet. However, despite decades of research, there remain many little studied and poorly understood aspects of arc magmatism and this dissertation examines three such topics.

As not all ancient arcs are exposed to the lowest crustal levels, I have shown that how the geochemistry of upper crustal arc rocks can be used to determine the mineralogy of the unexposed lower crust in the Bonanza arc, thereby providing a robust minimum bound on the thickness of that arc. The conclusions of that study strengthen correlations

between the Bonanza and Talkeetna arcs, which, if correct, begs question the along-strike extent of Wrangellia arc volcanism in Jurassic time.

Arc thickness is known to correlate with magma alkalinity and my experimental results from arc-like melts have shown for the first time that alkalinity is positively correlated with the melt concentration of S. This finding indicates that arc magmas will vary in S content depending on arc maturity, a previously unsuspected feature of the geologic S cycle. My results also suggest that increasing S concentration in reduced melts solely by alkalinity is limited, potentially indicating a hitherto unknown aspect of S dissolution in reduced silicate melts.

The ultimate source of S and other chalcophile elements in arc magmas has long been enigmatic. I have shown here that fluids related to sediment melting deep in the arc are a potent means by which to enrich the arc mantle with chalcophile elements. A surprising finding of this work is that reduced fluids carry higher concentrations of chalcophile elements than oxidized fluids, although the reason for this difference requires further study. This work nonetheless indicates that reduced sediments subducted beneath arcs are a viable source from which to enrich the arc mantle.

The questions answered by this work are small steps on our path to understanding the processes controlling the chemistry of volcanic arcs and, thus, Earth's unique continental crust. In turn, the questions raised by the answers provided in this work highlight further steps by which we may continue to acquire the knowledge needed to read the unique geologic story of our planet.

Bibliography

Adam, J. and Green, T., 2006. Trace element partitioning between mica-and amphibole-bearing garnet lherzolite and hydrous basanitic melt: 1. Experimental results and the investigation of controls on partitioning behaviour. *Contributions to Mineralogy and Petrology*, *152*(1), pp.1-17.

Akella, J. and Kennedy, G.C., 1971. Melting of gold, silver, and copper—proposal for a new high-pressure calibration scale. *Journal of Geophysical Research*, *76*(20), pp.4969-4977.

Anderson, J.L. and Smith, D.R., 1995. The effects of temperature and fO_2 on the Al-in-hornblende barometer. *American Mineralogist*, *80*(5-6), pp.549-559.

Andrew, A., Armstrong, R.L. and Runkle, D., 1991. Neodymium–strontium–lead isotopic study of Vancouver Island igneous rocks. *Canadian Journal of Earth Sciences*, *28*(11), pp.1744-1752.

Annen, C., Blundy, J.D. and Sparks, R.S.J., 2005. The genesis of intermediate and silicic magmas in deep crustal hot zones. *Journal of Petrology*, *47*(3), pp.505-539.

Arculus, R.J. and Johnson, R.W., 1978. Criticism of generalised models for the magmatic evolution of arc-trench systems. *Earth and Planetary Science Letters*, *39*(1), pp.118-126.

Ariskin, A.A., Danyushevsky, L.V., Bychkov, K.A., McNeill, A.W., Barmina, G.S. and Nikolaev, G.S., 2013. Modeling solubility of Fe-Ni sulfides in basaltic magmas: the effect of nickel. *Economic Geology*, *108*(8), pp.1983-2003.

Bai, T.B. and Van Groos, A.K., 1999. The distribution of Na, K, Rb, Sr, Al, Ge, Cu, W, Mo, La, and Ce between granitic melts and coexisting aqueous fluids. *Geochimica et Cosmochimica Acta*, *63*(7), pp.1117-1131.

Baker, D.R., Barnes, S.J., Simon, G. and Bernier, F., 2001. Fluid transport of sulfur and metals between sulfide melt and basaltic melt. *The Canadian Mineralogist*, *39*(2), pp.537-546.

Baker, D.R. and Moretti, R., 2011. Modeling the solubility of sulfur in magmas: a 50-year old geochemical challenge. *Reviews in Mineralogy and Geochemistry*, *73*(1), pp.167-213.

Bali, E., Keppler, H. and Audetat, A., 2012. The mobility of W and Mo in subduction zone fluids and the Mo–W–Th–U systematics of island arc magmas. *Earth and Planetary Science Letters*, *351*, pp.195-207.

Barton, P.B., 1971. The Fe-Sb-S system. *Economic Geology*, *66*(1), pp.121-132.

Baumer, A., Blanc, P., Cesbron, F. and Ohnenstetter, D., 1997. Cathodoluminescence of synthetic (doped with rare-earth elements) and natural anhydrites. *Chemical Geology*, *138*(1-2), pp.73-80.

Beermann, O., Botcharnikov, R.E., Holtz, F., Diedrich, O. and Nowak, M., 2011. Temperature dependence of sulfide and sulfate solubility in olivine-saturated basaltic magmas. *Geochimica et Cosmochimica Acta*, *75*(23), pp.7612-7631.

Bédard, J.H., 2006. Trace element partitioning in plagioclase feldspar. *Geochimica et Cosmochimica Acta*, *70*(14), pp.3717-3742.

Bédard, J.H., 2007. Trace element partitioning coefficients between silicate melts and orthopyroxene: parameterizations of D variations. *Chemical Geology*, *244*(1), pp.263-303.

Behn, M.D., Kelemen, P.B., Hirth, G., Hacker, B.R. and Massonne, H.J., 2011. Diapirs as the source of the sediment signature in arc lavas. *Nature Geoscience*, *4*(9), pp.641-646.

Behrens, H., Roux, J., Neuville, D.R. and Siemann, M., 2006. Quantification of dissolved H 2 O in silicate glasses using confocal microRaman spectroscopy. *Chemical Geology*, *229*(1), pp.96-112.

Bezard, R., Schaefer, B.F., Turner, S., Davidson, J.P. and Selby, D., 2015. Lower crustal assimilation in oceanic arcs: Insights from an osmium isotopic study of the Lesser Antilles. *Geochimica et Cosmochimica Acta*, *150*, pp.330-344.

Bird, P., 1979. Continental delamination and the Colorado Plateau. *Journal of Geophysical Research: Solid Earth*, *84*(B13), pp.7561-7571.

Bradbury J. W., 1983. *Pyrrhotite solubility in hydrous albite melts.* (Ph.D. thesis, Pennsyvania State University)

Breitsprecher, K. and Mortensen, J.K., 2004. BCAge 2004A-1-a database of isotopic age determinations for rock units from British Columbia. *BC Ministry of Forests, Mines and Lands, Open File*, *3*.

Brenan, J.M., 2008. Re–Os fractionation by sulfide melt–silicate melt partitioning: a new spin. *Chemical Geology*, *248*(3), pp.140-165.

Brounce, M.N., Kelley, K.A. and Cottrell, E., 2014. Variations in Fe3+/∑ Fe of Mariana Arc Basalts and Mantle Wedge f O2. *Journal of Petrology*, *55*(12), pp.2513-2536.

Buchanan, D.L., Nolan, J., Wilkinson, N. and de Villiers, J.R., 1983. An experimental investigation of sulphur solubility as a function of temperature in synthetic silicate melts. *Geol. Soc. South Africa Spec. Pub*, *7*, pp.383-391.

Bureau, H. and Keppler, H., 1999. Complete miscibility between silicate melts and hydrous fluids in the upper mantle: experimental evidence and geochemical implications. *Earth and Planetary Science Letters*, *165*(2), pp.187-196.

Burns, L.E., 1985. The Border Ranges ultramafic and mafic complex, south-central Alaska: cumulate fractionates of island-arc volcanics. *Canadian Journal of Earth Sciences, 22*(7), pp.1020-1038.

Canil, D., 1999. The Ni-in-garnet geothermometer: calibration at natural abundances. *Contributions to Mineralogy and Petrology*, *136*(3), pp.240-246.

Canil, D., Styan, J., Larocque, J., Bonnet, E. and Kyba, J., 2010. Thickness and composition of the Bonanza arc crustal section, Vancouver Island, Canada. *Geological Society of America Bulletin*, *122*(7-8), pp.1094-1105.

Canil, D., Johnston, S.T., Larocque, J., Friedman, R. and Heaman, L.M., 2013. Age, construction, and exhumation of the midcrust of the Jurassic Bonanza arc, Vancouver Island, Canada. *Lithosphere*, *5*(1), pp.82-91.

Canil, D. and Fellows, S.A., 2017. Sulphide–sulphate stability and melting in subducted sediment and its role in arc mantle redox and chalcophile cycling in space and time. *Earth and Planetary Science Letters*, *470*, pp.73-86.

Carroll, M.R. and Rutherford, M.J., 1985. Sulfide and sulfate saturation in hydrous silicate melts. *Journal of Geophysical Research: Solid Earth*, *90*(S02).

Carroll, M.R. and Rutherford, M.J., 1987. The stability of igneous anhydrite: experimental results and implications for sulfur behavior in the 1982 El Chichon trachyandesite and other evolved magmas. *Journal of Petrology*, *28*(5), pp.781-801.

Carroll, M.R. and Rutherford, M.J., 1988. Sulfur speciation in hydrous experimental glasses of varying oxidation state--results from measured wavelength shifts of sulfur X-rays. *American Mineralogist*, *73*(7), pp.845-9.

Chiaradia, M., 2014. Copper enrichment in arc magmas controlled by overriding plate thickness. *Nature Geoscience*, *7*(1), pp.43-46.

Cicconi, M.R., Giuli, G., Ertel-Ingrisch, W., Paris, E. and Dingwell, D.B., 2015. The effect of the [Na/(Na+ K)] ratio on Fe speciation in phonolitic glasses. *American Mineralogist*, *100*(7), pp.1610-1619.

Clémente, B., Scaillet, B. and Pichavant, M., 2004. The solubility of sulphur in hydrous rhyolitic melts. *Journal of Petrology*, *45*(11), pp.2171-2196.

Clowes, R.M., Brandon, M.T., Green, A.G., Yorath, C.J., Brown, A.S., Kanasewich, E.R. and Spencer, C., 1987. LITHOPROBE—southern Vancouver Island: Cenozoic subduction complex imaged by deep seismic reflections. *Canadian Journal of Earth Sciences*, *24*(1), pp.31-51.

Condie, K.C., 1989. Origin of the Earth's crust. *Palaeogeography, Palaeoclimatology, Palaeoecology*, *75*(1-2), pp.57-81.

Condie, K.C., 1990. Growth and accretion of continental crust: inferences based on Laurentia. *Chemical Geology*, *83*(3-4), pp.183-194.

Creaser, R.A., Erdmer, P., Stevens, R.A. and Grant, S.L., 1997. Tectonic affinity of Nisutlin and Anvil assemblage strata from the Teslin tectonic zone, northern Canadian Cordillera: Constraints from neodymium isotope and geochemical evidence. *Tectonics*, *16*(1), pp.107-121.

Creaser, R.A., Grütter, H., Carlson, J. and Crawford, B., 2004. Macrocrystal phlogopite Rb–Sr dates for the Ekati property kimberlites, Slave Province, Canada: evidence for multiple intrusive episodes in the Paleocene and Eocene. *Lithos*, *76*(1), pp.399-414.

D'Souza, R.J., Canil, D. and Creaser, R.A., 2016. Assimilation, differentiation, and thickening during formation of arc crust in space and time: The Jurassic Bonanza arc, Vancouver Island, Canada. *Geological Society of America Bulletin*, *128*(3-4), pp.543-557.

Danckwerth, P.A., Hess, P.C. and Rutherford, M.J., 1979. The solubility of sulfur in high-TiO2 mare basalts. In *Lunar and Planetary Science Conference Proceedings* (Vol. 10, pp. 517-530).

Day, D.E., 1976. Mixed alkali glasses—their properties and uses. *Journal of Non-Crystalline Solids*, *21*(3), pp.343-372.

DeBari, S.M. and Coleman, R.G., 1989. Examination of the deep levels of an island arc: Evidence from the Tonsina Ultramafic-Mafic Assemblage, Tonsina, Alaska. *Journal of Geophysical Research: Solid Earth*, *94*(B4), pp.4373-4391.

DeBari, S.M. and Sleep, N.H., 1991. High-Mg, low-Al bulk composition of the Talkeetna island arc, Alaska: Implications for primary magmas and the nature of arc crust. *Geological Society of America Bulletin*, *103*(1), pp.37-47.

DeBari, S.M., Anderson, R.G. and Mortensen, J.K., 1999. Correlation among lower to upper crustal components in an island arc: the Jurassic Bonanza arc, Vancouver Island, Canada. *Canadian Journal of Earth Sciences*, *36*(8), pp.1371-1413.

Defant, M.J. and Drummond, M.S., 1990. Derivation of some modern arc magmas by melting of young subducted lithosphere. *Nature*, *347*(6294), pp.662-665.

DePaolo, D.J., 1981. Trace element and isotopic effects of combined wallrock assimilation and fractional crystallization. *Earth and planetary science letters*, *53*(2), pp.189-202.

Ding, S., Dasgupta, R. and Tsuno, K., 2014. Sulfur concentration of martian basalts at sulfide saturation at high pressures and temperatures–implications for deep sulfur cycle on Mars. *Geochimica et Cosmochimica Acta*, *131*, pp.227-246.

Ducea, M.N., Mcinnes, B.I. and Wyllie, P.J., 1994. Sulfur variations in glasses from volcanic rocks: effect of melt composition on sulfur solubility. *International Geology Review*, *36*(8), pp.703-714.

Duffy, J.A., 1996. Optical basicity: A practical acid-base theory for oxides and oxyanions. *Journal of Chemical Education*, *73*(12), p.1138.

England, P. and Wilkins, C., 2004. A simple analytical approximation to the temperature structure in subduction zones. *Geophysical Journal International*, *159*(3), pp.1138-1154.

Evans, K.A. and Tomkins, A.G., 2011. The relationship between subduction zone redox budget and arc magma fertility. *Earth and Planetary Science Letters*, *308*(3), pp.401-409.

Falcone, R., Ceola, S., Daneo, A. and Maurina, S., 2011. The role of sulfur compounds in coloring and melting kinetics of industrial glass. *Reviews in Mineralogy and Geochemistry*, *73*(1), pp.113-141.

Fecova, K., 2009. *Conuma River and Leagh Creek intrusive complexes: windows into mid-crustal levels of the Jurassic Bonanza island arc, Vancouver Island, British Columbia* (M.Sc thesis, Dept. of Earth Sciences-Simon Fraser University).

Fincham, C.J.B. and Richardson, F.D., 1954, April. The behaviour of sulphur in silicate and aluminate melts. In *Proceedings of the Royal Society of London A: Mathematical, Physical and Engineering Sciences* (Vol. 223, No. 1152, pp. 40-62). The Royal Society.

Flynn, R.T. and Burnham, C.W., 1978. An experimental determination of rare earth partition coefficients between a chloride containing vapor phase and silicate melts. *Geochimica et Cosmochimica Acta*, *42*(6), pp.685-701.

Fortin, M.A., Riddle, J., Desjardins-Langlais, Y. and Baker, D.R., 2015. The effect of water on the sulfur concentration at sulfide saturation (SCSS) in natural melts. *Geochimica et Cosmochimica Acta*, *160*, pp.100-116.

Freymuth, H., Vils, F., Willbold, M., Taylor, R.N. and Elliott, T., 2015. Molybdenum mobility and isotopic fractionation during subduction at the Mariana arc. *Earth and Planetary Science Letters*, *432*, pp.176-186.

Freymuth, H., Elliott, T., van Soest, M. and Skora, S., 2016. Tracing subducted black shales in the Lesser Antilles arc using molybdenum isotope ratios. *Geology*, *44*(12), pp.987-990.

Gerya, T.V., Connolly, J.A., Yuen, D.A., Gorczyk, W. and Capel, A.M., 2006. Seismic implications of mantle wedge plumes. Physics of the Earth and Planetary Interiors, 156(1), pp.59-74.

Green, T.H., 1980. Island arc and continent-building magmatism—A review of petrogenic models based on experimental petrology and geochemistry. Tectonophysics, 63(1-4), pp.367-385.

Green, T.H. and Adam, J., 2003. Experimentally-determined trace element characteristics of aqueous fluid from partially dehydrated mafic oceanic crust at 3.0 GPa, 650–700°C. *European Journal of Mineralogy*, *15*(5), pp.815-830.

Greene, A.R., Scoates, J.S., Weis, D., Nixon, G.T. and Kieffer, B., 2009. Melting history and magmatic evolution of basalts and picrites from the accreted Wrangellia oceanic plateau, Vancouver Island, Canada. *Journal of Petrology*, *50*(3), pp.467-505.

Grove, T., Parman, S., Bowring, S., Price, R. and Baker, M., 2002. The role of an H2O-rich fluid component in the generation of primitive basaltic andesites and andesites from the Mt. Shasta region, N California. *Contributions to Mineralogy and Petrology*, *142*(4), pp.375-396.

Gupta, A.K., 2015. *Origin of potassium-rich silica-deficient igneous rocks*. New Delhi: Springer.

Gvirtzman, Z. and Nur, A., 1999. The formation of Mount Etna as the consequence of slab rollback. *Nature*, *401*(6755), pp.782-785.

Gwinn, R. and Hess, P.C., 1989. Iron and titanium solution properties in peraluminous and peralkaline rhyolitic liquids. *Contributions to Mineralogy and petrology*, *101*(3), pp.326-338.

Hacker, B.R., Mehl, L., Kelemen, P.B., Rioux, M., Behn, M.D. and Luffi, P., 2008. Reconstruction of the Talkeetna intraoceanic arc of Alaska through thermobarometry. *Journal of Geophysical Research: Solid Earth*, *113*(B3).

Hacker, B.R., Kelemen, P.B. and Behn, M.D., 2011. Differentiation of the continental crust by relamination. *Earth and Planetary Science Letters*, *307*(3), pp.501-516.

Haughton, D.R., Roeder, P.L. and Skinner, B.J., 1974. Solubility of sulfur in mafic magmas. *Economic Geology*, *69*(4), pp.451-467.

Hawkesworth, C.J., Hergt, J.M., Ellam, R.M. and Mc Dermott, F., 1991. Element fluxes associated with subduction related magmatism. *Philosophical Transactions of the Royal Society of London A: Mathematical, Physical and Engineering Sciences*, *335*(1638), pp.393-405.

Hildreth, W. and Moorbath, S., 1988. Crustal contributions to arc magmatism in the Andes of central Chile. *Contributions to mineralogy and petrology*, *98*(4), pp.455-489.

Holzheid, A. and Grove, T.L., 2002. Sulfur saturation limits in silicate melts and their implications for core formation scenarios for terrestrial planets. *American Mineralogist*, *87*(2-3), pp.227-237.

Huene, R. and Scholl, D.W., 1991. Observations at convergent margins concerning sediment subduction, subduction erosion, and the growth of continental crust. *Reviews of Geophysics*, *29*(3), pp.279-316.

Isachsen, C.E., 1987. Geology, geochemistry, and cooling history of the Westcoast Crystalline Complex and related rocks, Meares Island and vicinity, Vancouver Island, British Columbia. *Canadian Journal of Earth Sciences*, *24*(10), pp.2047-2064.

Irving, A.J. and Frey, F.A., 1978. Distribution of trace elements between garnet megacrysts and host volcanic liquids of kimberlitic to rhyolitic composition. *Geochimica et Cosmochimica Acta*, *42*(6), pp.771-787.

Isard, J.O., 1969. The mixed alkali effect in glass. *Journal of Non-Crystalline Solids*, *1*(3), pp.235-261.

Jagoutz, O., Müntener, O., Ulmer, P., Pettke, T., Burg, J.P., Dawood, H. and Hussain, S., 2007. Petrology and mineral chemistry of lower crustal intrusions: the Chilas Complex, Kohistan (NW Pakistan). *Journal of Petrology*, *48*(10), pp.1895-1953.

Jagoutz, O., 2010. Construction of the granitoid crust of an island arc. Part II: a quantitative petrogenetic model. *Contributions to Mineralogy and Petrology*, *160*(3), pp.359-381.

Jagoutz, O. and Schmidt, M.W., 2012. The formation and bulk composition of modern juvenile continental crust: The Kohistan arc. *Chemical Geology*, *298*, pp.79-96.

Jagoutz, O. and Behn, M.D., 2013. Foundering of lower island-arc crust as an explanation for the origin of the continental Moho. *Nature*, *504*(7478), pp.131-134.

Jégo, S. and Dasgupta, R., 2013. Fluid-present melting of sulfide-bearing ocean-crust: Experimental constraints on the transport of sulfur from subducting slab to mantle wedge. *Geochimica et Cosmochimica Acta*, *110*, pp.106-134.

Jégo, S. and Dasgupta, R., 2014. The fate of sulfur during fluid-present melting of subducting basaltic crust at variable oxygen fugacity. *Journal of Petrology*, *55*(6), pp.1019-1050.

Jenner, F.E., O'Neill, H.S.C., Arculus, R.J. and Mavrogenes, J.A., 2010. The magnetite crisis in the evolution of arc-related magmas and the initial concentration of Au, Ag and Cu. *Journal of Petrology*, *51*(12), pp.2445-2464.

Jugo, P.J., Luth, R.W. and Richards, J.P., 2005a. An experimental study of the sulfur content in basaltic melts saturated with immiscible sulfide or sulfate liquids at 1300° C and 1.0 GPa. *Journal of Petrology*, *46*(4), pp.783-798.

Jugo, P.J., Luth, R.W. and Richards, J.P., 2005b. Experimental data on the speciation of sulfur as a function of oxygen fugacity in basaltic melts. *Geochimica et Cosmochimica Acta*, *69*(2), pp.497-503.

Jugo, P.J., 2009. Sulfur content at sulfide saturation in oxidized magmas. *Geology*, *37*(5), pp.415-418.

Jugo, P.J., Wilke, M. and Botcharnikov, R.E., 2010. Sulfur K-edge XANES analysis of natural and synthetic basaltic glasses: Implications for S speciation and S content as function of oxygen fugacity. *Geochimica et Cosmochimica Acta*, *74*(20), pp.5926-5938.

Kay, R.W. and Mahlburg-Kay, S., 1991. Creation and destruction of lower continental crust. *Geologische Rundschau*, *80*(2), pp.259-278.

Kelemen, P.B., Hanghøj, K. and Greene, A.R., 2003. One view of the geochemistry of subduction-related magmatic arcs, with an emphasis on primitive andesite and lower crust. *Treatise on Geochemistry*, *3*, p.659.

Keppler, H. and Wyllie, P.J., 1991. Partitioning of Cu, Sn, Mo, W, U, and Th between melt and aqueous fluid in the systems haplogranite-H_2O−HCl and haplogranite-H_2O−HF. *Contributions to Mineralogy and Petrology*, *109*(2), pp.139-150.

Keppler, H., 1996. Constraints from partitioning experiments on the composition of subduction-zone fluids. *Nature*, *380*(6571), pp.237-240.

Kessel, R., Ulmer, P., Pettke, T., Schmidt, M.W. and Thompson, A.B., 2005a. The water–basalt system at 4 to 6 GPa: phase relations and second critical endpoint in a K-free eclogite at 700 to 1400°C. *Earth and Planetary Science Letters*, *237*(3-4), pp.873-892.

Kessel, R., Schmidt, M.W., Ulmer, P. and Pettke, T., 2005b. Trace element signature of subduction-zone fluids, melts and supercritical liquids at 120–180 km depth. *Nature*, *437*(7059), pp.724-727.

Klemme, S., Günther, D., Hametner, K., Prowatke, S. and Zack, T., 2006. The partitioning of trace elements between ilmenite, ulvospinel, armalcolite and silicate melts with implications for the early differentiation of the moon. *Chemical Geology*, *234*(3), pp.251-263.

Klimm, K., Kohn, S.C., O'Dell, L.A., Botcharnikov, R.E. and Smith, M.E., 2012. The dissolution mechanism of sulphur in hydrous silicate melts. I: Assessment of analytical techniques in determining the sulphur speciation in iron-free to iron-poor glasses. *Chemical Geology*, *322*, pp.237-249.

König, S., Wille, M., Voegelin, A. and Schoenberg, R., 2016. Molybdenum isotope systematics in subduction zones. *Earth and Planetary Science Letters*, *447*, pp.95-102.

Kress, V.C. and Carmichael, I.S., 1991. The compressibility of silicate liquids containing Fe 2 O 3 and the effect of composition, temperature, oxygen fugacity and pressure on their redox states. *Contributions to Mineralogy and Petrology*, *108*(1), pp.82-92.

Kuhn, M.. Contributions from Jed Wing, Steve Weston, Andre Williams, Chris Keefer, Allan Engelhardt, Tony Cooper, Zachary Mayer, Brenton Kenkel, the R Core Team, Michael Benesty, Reynald Lescarbeau, Andrew Ziem, Luca Scrucca, Yuan Tang, Can Candan and Tyler Hunt. (2017). *caret: Classification and Regression Training*. R package version 6.0-77. https://CRAN.R-project.org/package=caret

Labanieh, S., Chauvel, C., Germa, A. and Quidelleur, X., 2012. Martinique: a clear case for sediment melting and slab dehydration as a function of distance to the trench. *Journal of Petrology*, *53*(12), pp.2441-2464.

Lang, J.R., Lueck, B., Mortensen, J.K., Russell, J.K., Stanley, C.R. and Thompson, J.F., 1995. Triassic-Jurassic silica-undersaturated and silica-saturated alkalic intrusions in the Cordillera of British Columbia: Implications for arc magmatism. *Geology*, *23*(5), pp.451-454.

Larocque, J.P., 2008. *The role of amphibole in the evolution of arc magmas and crust: the case from the Jurassic Bonanza arc section, Vancouver Island, Canada* (M.Sc. thesis, School of Earth and Ocean Sciences-University of Victoria).

Larocque, J. and Canil, D., 2010. The role of amphibole in the evolution of arc magmas and crust: the case from the Jurassic Bonanza arc section, Vancouver Island, Canada. *Contributions to Mineralogy and Petrology*, *159*(4), pp.475-492.

LeBas, M.J., Maitre, R.L., Streckeisen, A. and Zanettin, B., 1986. A chemical classification of volcanic rocks based on the total alkali-silica diagram. *Journal of Petrology*, *27*, pp.745-750.

Le Losq, C., Neuville, D.R., Moretti, R. and Roux, J., 2012. Determination of water content in silicate glasses using Raman spectrometry: Implications for the study of explosive volcanism. *American Mineralogist*, *97*(5-6), pp.779-790.

Lee, C.T.A., Leeman, W.P., Canil, D. and Li, Z.X.A., 2005. Similar V/Sc systematics in MORB and arc basalts: implications for the oxygen fugacities of their mantle source regions. *Journal of Petrology*, *46*(11), pp.2313-2336

Lee, C.T.A., Luffi, P., Chin, E.J., Bouchet, R., Dasgupta, R., Morton, D.M., Le Roux, V., Yin, Q.Z. and Jin, D., 2012. Copper systematics in arc magmas and implications for crust-mantle differentiation. *Science*, *336*(6077), pp.64-68.

Le Maitre, R.W., Streckeisen, A., Zanettin, B., Le Bas, M.J., Bonin, B. and Bateman, P. eds., 2005. *Igneous rocks: a classification and glossary of terms: recommendations of the International Union of Geological Sciences Subcommission on the Systematics of Igneous Rocks.* Cambridge University Press.

Lenoir, M., Grandjean, A., Poissonnet, S. and Neuville, D.R., 2009. Quantitation of sulfate solubility in borosilicate glasses using Raman spectroscopy. *Journal of Non-Crystalline Solids*, *355*(28), pp.1468-1473.

Li, C. and Ripley, E.M., 2005. Empirical equations to predict the sulfur content of mafic magmas at sulfide saturation and applications to magmatic sulfide deposits. *Mineralium Deposita*, *40*(2), pp.218-230.

Li, C. and Ripley, E.M., 2009. Sulfur contents at sulfide-liquid or anhydrite saturation in silicate melts: empirical equations and example applications. *Economic Geology*, *104*(3), pp.405-412.

Liu, Y., Samaha, N.T. and Baker, D.R., 2007. Sulfur concentration at sulfide saturation (SCSS) in magmatic silicate melts. *Geochimica et Cosmochimica Acta*, *71*(7), pp.1783-1799.

Logan, J.M. and Mihalynuk, M.G., 2014. Tectonic controls on early Mesozoic paired alkaline porphyry deposit belts (Cu-Au±Ag-Pt-Pd-Mo) within the Canadian Cordillera. *Economic Geology*, *109*(4), pp.827-858.

Long, D.A., 1977. *Raman spectroscopy* (Vol. 206). New York: McGraw-Hill.

Luhr, J.F., Carmichael, I.S. and Varekamp, J.C., 1984. The 1982 eruptions of El Chichón Volcano, Chiapas, Mexico: mineralogy and petrology of the anhydritebearing pumices. *Journal of Volcanology and Geothermal Research*, *23*(1-2), pp.69-108.

Luhr, J.F., 1990. Experimental phase relations of water-and sulfur-saturated arc magmas and the 1982 eruptions of El Chichón volcano. *Journal of Petrology*, *31*(5), pp.1071-1114.

Macpherson, C.G., 2008. Lithosphere erosion and crustal growth in subduction zones: Insights from initiation of the nascent East Philippine Arc. *Geology*, *36*(4), pp.311-314.

Mandeville, C.W., Webster, J.D., Rutherford, M.J., Taylor, B.E., Timbal, A. and Faure, K., 2002. Determination of molar absorptivities for infrared absorption bands of H2O in andesitic glasses. *American Mineralogist*, *87*(7), pp.813-821.

Mann, U. and Schmidt, M.W., 2015. Melting of pelitic sediments at subarc depths: 1. Flux vs. fluid-absent melting and a parameterization of melt productivity. *Chemical Geology*, *404*, pp.150-167.

Mantle, G.W. and Collins, W.J., 2008. Quantifying crustal thickness variations in evolving orogens: Correlation between arc basalt composition and Moho depth. *Geology*, *36*(1), pp.87-90.

Marsh, B.D., 1979. Island arc development: Some observations, experiments, and speculations. *The Journal of Geology*, *87*(6), pp.687-713.

Marschall, H.R. and Schumacher, J.C., 2012. Arc magmas sourced from mélange diapirs in subduction zones. *Nature Geoscience*, *5*(12), pp.862-867.

Mavrogenes, J.A. and O'Neill, H.S.C., 1999. The relative effects of pressure, temperature and oxygen fugacity on the solubility of sulfide in mafic magmas. *Geochimica et Cosmochimica Acta*, *63*(7), pp.1173-1180.

McDonough, W.F. and Sun, S.S., 1995. The composition of the Earth. *Chemical Geology*, *120*(3-4), pp.223-253.

McInnes, B.I. and Cameron, E.M., 1994. Carbonated, alkaline hybridizing melts from a sub-arc environment: Mantle wedge samples from the Tabar-Lihir-Tanga-Feni arc, Papua New Guinea. *Earth and Planetary Science Letters*, *122*(1-2), pp.125-141.

McLinden, C.A., Fioletov, V., Shephard, M.W., Krotkov, N., Li, C., Martin, R.V., Moran, M.D. and Joiner, J., 2016. Space-based detection of missing sulfur dioxide sources of global air pollution. *Nature Geoscience*, *9*(7), pp.496-500.

Médard, E., McCammon, C.A., Barr, J.A. and Grove, T.L., 2008. Oxygen fugacity, temperature reproducibility, and H2O contents of nominally anhydrous piston-cylinder experiments using graphite capsules. *American Mineralogist*, *93*(11-12), pp.1838-1844.

Mengason, M.J., Candela, P.A. and Piccoli, P.M., 2011. Molybdenum, tungsten and manganese partitioning in the system pyrrhotite–Fe–S–O melt–rhyolite melt: impact of sulfide segregation on arc magma evolution. *Geochimica et Cosmochimica Acta*, *75*(22), pp.7018-7030.

Metrich, N. and Clocchiatti, R., 1996. Sulfur abundance and its speciation in oxidized alkaline melts. *Geochimica et Cosmochimica Acta*, *60*(21), pp.4151-4160.

Miyashiro, A., 1974. Volcanic rock series in island arcs and active continental margins. *American Journal of Science*, *274*, pp.321-355.

Morgan, G.B. and London, D., 1996. Optimizing the electron microprobe analysis of hydrous alkali aluminosilicate glasses. *American Mineralogist*, *81*(9-10), pp.1176-1185.

Morgan, G.B. and London, D., 2005. Effect of current density on the electron microprobe analysis of alkali aluminosilicate glasses. *American Mineralogist*, *90*(7), pp.1131-1138.

Moune, S., Holtz, F. and Botcharnikov, R.E., 2009. Sulphur solubility in andesitic to basaltic melts: implications for Hekla volcano. *Contributions to Mineralogy and Petrology*, *157*(6), p.691.

Müller, D. and Groves, D.I., 1993. Direct and indirect associations between potassic igneous rocks, shoshonites and gold-copper deposits. *Ore Geology Reviews*, *8*(5), pp.383-406.

Muller, J.E., 1977. Evolution of the Pacific Margin, Vancouver Island, and adjacent regions. *Canadian Journal of Earth Sciences*, *14*(9), pp.2062-2085.

Mungall, J.E., 2002. Roasting the mantle: Slab melting and the genesis of major Au and Au-rich Cu deposits. *Geology*, *30*(10), pp.915-918.

Müntener, O. and Ulmer, P., 2006. Experimentally derived high-pressure cumulates from hydrous arc magmas and consequences for the seismic velocity structure of lower arc crust. *Geophysical Research Letters*, *33*(21) L21308.

Mysen, B.O. and Popp, R.K., 1980. Solubility of sulfur in $CaMgSi_2O_6$ and $NaAlSi_3O_8$ melts at high pressure and temperature with controlled f_{O2} and f_{S2}. *American Journal of Science*, *280*(1), pp.78-92.

Mysen, B.O., Virgo, D. and Seifert, F.A., 1982. The structure of silicate melts: implications for chemical and physical properties of natural magma. *Reviews of Geophysics*, *20*(3), pp.353-383.

Mysen, B.O., Virgo, D. and Seifert, F.A., 1985. Relationships between properties and structure of aluminosilicate melts. *American Mineralogist*, *70*(1-2), pp.88-105.

Naldrett, A.J., 1969. A portion of the system Fe–S–O between 900 and 1080 C and its application to sulfide ore magmas. *Journal of Petrology*, *10*(2), pp.171-201.

Nebel, O., Sossi, P.A., Benard, A., Wille, M., Vroon, P.Z. and Arculus, R.J., 2015. Redox-variability and controls in subduction zones from an iron-isotope perspective. *Earth and Planetary Science Letters*, *432*, pp.142-151.

Nicholls, I.A. and Harris, K.L., 1980. Experimental rare earth element partition coefficients for garnet, clinopyroxene and amphibole coexisting with andesitic and basaltic liquids. *Geochimica et Cosmochimica Acta*, *44*(2), pp.287-308.

Nielsen, R.L., Gallahan, W.E. and Newberger, F., 1992. Experimentally determined mineral-melt partition coefficients for Sc, Y and REE for olivine, orthopyroxene, pigeonite, magnetite and ilmenite. *Contributions to Mineralogy and Petrology*, *110*(4), pp.488-499.

Nixon, G.T., Hammack, Hamilton, J.V., Jennings, H., Larocque, J.P., Orr, A.J., Friedman, R.M., Archibald, Creaser, R.A., Orchard, M.J., D.A., Haggart, J.W., Tipper, H.W., Tozer, E.T., Cordey, F., and McRoberts, C.A., 2011a, Geology, geochronology, lithogeochemistry and metamorphism of the Mahatta Creek area, northern Vancouver Island (NTS 092L/05): British Columbia Geological Survey Map GM2011–03, scale 1:50 000, 1 sheet.

Nixon, G.T., Hammack, J.L., Koyanagi, V.M., Payie, G.J., Orr, A.J., Haggart, J.W., Orchard, M.J., Tozer, E.T., Friedman, R.M., Archibald, D.A., Palfy, J., and Cordey, F., 2011b, Geology, geochronology, lithogeochemistry and metamorphism of the Quatsino–Port McNeill area, northern Vancouver Island (NTS 092L/11, and parts of 092L/05, 12 and 13): British Columbia Geological Survey Map GM2011–02, scale 1:50 000, 1 sheet.

Nixon, G.T., Hammack, J.L., Koyanagi, V.M., Snyder, L.D., Payie, G.J., Panteleyev, A., Massey, N.W.D., Hamilton, J.V., Orr, A.J., Friedman, R.M., Archibald, D.A., Haggart, J.W., Orchard, M.J., Tozer, E.T., Tipper, H.W., Poulton, T.P., Palfy, J., and Cordey F., 2011c, Geology, geochronology, lithogeochemistry and metamorphism of the Holberg–Winter Harbour area, northern Vancouver Island (parts of NTS 092L/05, 12, 13; 102I/08, 09 and 16): British Columbia Geological Survey Map GM2011–01, scale 1:50 000, 1 sheet.

Nixon, G.T., Kelman, M.C., Larocque, J.P., Stevenson, D.B., Stokes, L.A., Pals, A., Styan, J., Johnston, K.A., Friedman, R.M., Mortensen, J.K., Orchard, M.J., and McRoberts, C.A., 2011d, Geology, geochronology, lithogeochemistry and metamorphism of the Nimpkish–Telegraph Cove area, northern Vancouver Island (NTS 092L/07 and part of 092L/10): British Columbia Geological Survey Map GM2011–05, scale 1:50 000, 1 sheet.

Nixon, G.T., Snyder, L.D., Payie, G.J., Long, S., Finnie, A., Orr, A.J., Friedman, R.M., Archibald, D.A., Orchard, M.J., Tozer, E.T., Poulton, T.P., and Haggart, J.W., 2011e, Geology, geochronology, lithogeochemistry and metamorphism of the Alice Lake area, northern Vancouver Island (NTS 092L/06 and part of 092L/03): British Columbia Geological Survey Map GM2011–04, scale 1:50 000, 1 sheet.

Noll, P.D., Newsom, H.E., Leeman, W.P. and Ryan, J.G., 1996. The role of hydrothermal fluids in the production of subduction zone magmas: evidence from siderophile and chalcophile trace elements and boron. *Geochimica et Cosmochimica Acta*, *60*(4), pp.587-611.

O'Neill, H.S.C. and Mavrogenes, J.A., 2002. The sulfide capacity and the sulfur content at sulfide saturation of silicate melts at 1400°C and 1 bar. *Journal of Petrology*, *43*(6), pp.1049-1087.

Paul, A. and Douglas, R.W., 1965. Ferrous-ferric equilibrium in binary alkali silicate glasses. *Physics and Chemistry of Glasses*, *6*(6), p.207.

Paulson, B.D., 2010. *Magmatic processes in the Jurassic Bonanza Arc: insights from the Alberni region of Vancouver Island,* Canada (M.Sc. Thesis, Department of Geology-Western Washington University).

Peach, C.L. and Mathez, E.A., 1993. Sulfide melt-silicate melt distribution coefficients for nickel and iron and implications for the distribution of other chalcophile elements. *Geochimica et Cosmochimica Acta*, *57*(13), pp.3013-3021.

Peach, C.L., Mathez, E.A., Keays, R.R. and Reeves, S.J., 1994. Experimentally determined sulfide melt-silicate melt partition coefficients for iridium and palladium. *Chemical Geology*, *117*(1-4), pp.361-377.

Penniston-Dorland, S.C., Kohn, M.J. and Manning, C.E., 2015. The global range of subduction zone thermal structures from exhumed blueschists and eclogites: Rocks are hotter than models. *Earth and Planetary Science Letters*, *428*, pp.243-254.

Plafker, G., Nokleberg, W.J. and Lull, J.S., 1989. Bedrock geology and tectonic evolution of the Wrangellia, Peninsular, and Chugach Terranes along the Trans-Alaska Crustal Transect in the Chugach Mountains and Southern Copper River Basin, Alaska. *Journal of Geophysical Research: Solid Earth, 94*(B4), pp.4255-4295.

Plank, T. and Langmuir, C.H., 1993. Tracing trace elements from sediment input to volcanic output at subduction zones. *Nature*, *362*(6422), pp.739-743.

Plank, T. and Langmuir, C.H., 1998. The chemical composition of subducting sediment and its consequences for the crust and mantle. *Chemical Geology*, *145*(3), pp.325-394.

Prowatke, S. and Klemme, S., 2005. Effect of melt composition on the partitioning of trace elements between titanite and silicate melt. *Geochimica et Cosmochimica Acta*, *69*(3), pp.695-709.

Prowatke, S. and Klemme, S., 2006. Trace element partitioning between apatite and silicate melts. *Geochimica et Cosmochimica Acta*, *70*(17), pp.4513-4527.

R Core Team (2017). R: A language and environment for statistical computing. *R Foundation for Statistical Computing,* Vienna, Austria. https://www.R-project.org/

Rapp, R.P., Shimizu, N., Norman, M.D. and Applegate, G.S., 1999. Reaction between slab-derived melts and peridotite in the mantle wedge: experimental constraints at 3.8 GPa. *Chemical Geology*, *160*(4), pp.335-356.

Reed, M.J., Candela, P.A. and Piccoli, P.M., 2000. The distribution of rare earth elements between monzogranitic melt and the aqueous volatile phase in experimental investigations at 800°C and 200 MPa. *Contributions to Mineralogy and Petrology*, *140*(2), pp.251-262.

Ridolfi, F., Renzulli, A. and Puerini, M., 2010. Stability and chemical equilibrium of amphibole in calc-alkaline magmas: an overview, new thermobarometric formulations and application to subduction-related volcanoes. *Contributions to Mineralogy and Petrology*, *160*(1), pp.45-66.

Righter, K., Pando, K. and Danielson, L.R., 2009. Experimental evidence for sulfur-rich martian magmas: Implications for volcanism and surficial sulfur sources. *Earth and Planetary Science Letters*, *288*(1), pp.235-243.

Rudnick, R.L., 1995. Making continental crust. *Nature*, *378*(6557), pp.571-577.

Rudnick, R.L. and Gao, S., 2003. Composition of the continental crust. *Treatise on geochemistry*, *3*, p.659.

Ryerson, F.J. and Watson, E.B., 1987. Rutile saturation in magmas: implications for TiNbTa depletion in island-arc basalts. *Earth and Planetary Science Letters*, *86*(2-4), pp.225-239.

Samson, S.D., Patchett, P.J., Gehrels, G.E. and Anderson, R.G., 1990. Nd and Sr isotopic characterization of the Wrangellia terrane and implications for crustal growth of the Canadian Cordillera. *The Journal of Geology*, *98*(5), pp.749-762.

Sarbas, B. and Nohl, U., 2008. The GEOROC database as part of a growing geoinformatics network. *Geoinformatics 2008-Data to Knowledge, Proceedings: U.S. Geological Survey Scientific Investigations Report 2008-5172,* pp.42-43.

Sattari, P., Brenan, J.M., Horn, I. and McDonough, W.F., 2002. Experimental constraints on the sulfide-and chromite-silicate melt partitioning behavior of rhenium and platinum-group elements. *Economic Geology*, *97*(2), pp.385-398.

Scaillet, B. and Macdonald, R., 2006. Experimental and thermodynamic constraints on the sulphur yield of peralkaline and metaluminous silicic flood eruptions. *Journal of Petrology*, *47*(7), pp.1413-1437.

Scaillet, B. and Pichavant, M., 2005. A model of sulphur solubility for hydrous mafic melts: application to the determination of magmatic fluid compositions of Italian volcanoes. *Annals of Geophysics*, *48*(4-5).

Schmidt, M.W. and Poli, S., 1998. Experimentally based water budgets for dehydrating slabs and consequences for arc magma generation. *Earth and Planetary Science Letters, 163*(1), pp.361-379.

Schmidt, M.W., Vielzeuf, D. and Auzanneau, E., 2004. Melting and dissolution of subducting crust at high pressures: the key role of white mica. *Earth and Planetary Science Letters*, *228*(1), pp.65-84.

Shima, H. and Naldrett, A.J., 1975. Solubility of sulfur in an ultramafic melt and the relevance of the system Fe-SO. *Economic Geology*, *70*(5), pp.960-967.

Sillitoe, R.H., 2010. Porphyry copper systems. *Economic geology*, *105*(1), pp.3-41.

Simon, A.C., Pettke, T., Candela, P.A., Piccoli, P.M. and Heinrich, C.A., 2007. The partitioning behavior of As and Au in S-free and S-bearing magmatic assemblages. *Geochimica et Cosmochimica Acta*, *71*(7), pp.1764-1782.

Sisson, T.W., 1991. Pyroxene-high silica rhyolite trace element partition coefficients measured by ion microprobe. *Geochimica et Cosmochimica Acta*, *55*(6), pp.1575-1585.

Sisson, T.W. and Bacon, C.R., 1992. Garnet/high-silica rhyolite trace element partition coefficients measured by ion microprobe. *Geochimica et Cosmochimica Acta*, *56*(5), pp.2133-2136.

Sisson, T.W., Ratajeski, K., Hankins, W.B. and Glazner, A.F., 2005. Voluminous granitic magmas from common basaltic sources. *Contributions to Mineralogy and Petrology*, *148*(6), pp.635-661.

Skora, S., Freymuth, H., Blundy, J., Elliott, T. and Guillong, M., 2017. An experimental study of the behaviour of cerium/molybdenum ratios during subduction: Implications for tracing the slab component in the Lesser Antilles. and Mariana arc. *Geochimica et Cosmochimica Acta*, *212*, pp.133-155.

Soetaert K., Van den Meersche, K., van Oevelen, D. (2009). *limSolve: Solving Linear Inverse Models.* R-package version 1.5.1. https://CRAN.R-project.org/package=limSolve

Stalder, R., Foley, S.F., Brey, G.P. and Horn, I., 1998. Mineral-aqueous fluid partitioning of trace elements at 900–1200 C and 3.0–5.7 GPa: new experimental data for garnet, clinopyroxene, and rutile, and implications for mantle metasomatism. *Geochimica et Cosmochimica Acta*, *62*(10), pp.1781-1801.

Stimac, J. and Hickmott, D., 1994. Trace-element partition coefficients for ilmenite, orthopyroxene and pyrrhotite in rhyolite determined by micro-PIXE analysis. *Chemical Geology*, *117*(1-4), pp.313-330.

Stolper, E. and Newman, S., 1994. The role of water in the petrogenesis of Mariana trough magmas. *Earth and Planetary Science Letters*, *121*(3-4), pp.293-325.

Sun, S.S. and McDonough, W.S., 1989. Chemical and isotopic systematics of oceanic basalts: implications for mantle composition and processes. *Geological Society, London, Special Publications*, *42*(1), pp.313-345.

Suzuki, T., Hirata, T., Yokoyama, T.D., Imai, T. and Takahashi, E., 2012. Pressure effect on element partitioning between minerals and silicate melt: melting experiments on basalt up to 20GPa. *Physics of the Earth and Planetary Interiors*, *208*, pp.59-73.

Taylor, S. R., 1977, Island arcs, deep sea trenches and back-arc basins, chapter Island arc models and the composition of the continental crust: Maurice Ewing Series 1. American Geophysical Union, pp. 325–335.

Taylor, S.R., 1989. Growth of planetary crusts. *Tectonophysics*, *161*(3-4), pp.147-156.

Taylor, S.R. and McLennan, S.M., 1995. The geochemical evolution of the continental crust. *Reviews of Geophysics*, *33*(2), pp.241-265.

Tiepolo, M., Oberti, R., Zanetti, A., Vannucci, R. and Foley, S.F., 2007. Trace-element partitioning between amphibole and silicate melt. *Reviews in mineralogy and geochemistry*, *67*(1), pp.417-452.

Tsujimura, T. and Kitakaze, A., 2005. Experimental study of sulfur solubility in silicate melts coexisting with graphite as a function of silicate melt composition. *Resource Geology*, *55*(1), pp.55-60.

Tsuno, K. and Dasgupta, R., 2011. Melting phase relation of nominally anhydrous, carbonated pelitic-eclogite at 2.5–3.0 GPa and deep cycling of sedimentary carbon. *Contributions to Mineralogy and Petrology*, *161*(5), pp.743-763.

Turner, S.J. and Langmuir, C.H., 2015. The global chemical systematics of arc front stratovolcanoes: Evaluating the role of crustal processes. *Earth and Planetary Science Letters*, *422*, pp.182-193.

van Keken, P.E., Kiefer, B. and Peacock, S.M., 2002. High-resolution models of subduction zones: Implications for mineral dehydration reactions and the transport of water into the deep mantle. *Geochemistry, Geophysics, Geosystems*, *3*(10), 1056.

Vermeesch, P., 2012. On the visualisation of detrital age distributions. *Chemical Geology*, *312*, pp.190-194.

Wallace, P.J. and Edmonds, M., 2011. The sulfur budget in magmas: evidence from melt inclusions, submarine glasses, and volcanic gas emissions. *Reviews in Mineralogy and Geochemistry*, *73*(1), pp.215-246.

Watson, E.B. and Harrison, T.M., 1983. Zircon saturation revisited: temperature and composition effects in a variety of crustal magma types. *Earth and Planetary Science Letters*, *64*(2), pp.295-304.

Wendlandt, R.F., 1982. Sulfide saturation of basalt and andesite melts at high pressures and temperatures. *American Mineralogist*, *67*, pp.877-885.

White, W.M., and Klein, E.M., 2014. Composition of the oceanic crust. *Treatise on geochemistry (second edition)*, 4, p. 457.

Workman, R.K. and Hart, S.R., 2005. Major and trace element composition of the depleted MORB mantle (DMM). *Earth and Planetary Science Letters*, *231*(1), pp.53-72.

Wykes, J.L., O'neill, H.S.C. and Mavrogenes, J.A., 2015. The effect of FeO on the sulfur content at sulfide saturation (SCSS) and the selenium content at selenide saturation of silicate melts. *Journal of Petrology*, *56*(7), pp.1407-1424.

Webster, J.D., Holloway, J.R. and Hervig, R.L., 1989. Partitioning of lithophile trace elements between H_2O and H_2O+ CO_2 fluids and topaz rhyolite melt. *Economic Geology*, *84*(1), pp.116-134.

Yogodzinski, G.M., Kelemen, P.B., Hoernle, K., Brown, S.T., Bindeman, I., Vervoort, J.D., Sims, K.W., Portnyagin, M. and Werner, R., 2017. Sr and O isotopes in western Aleutian seafloor lavas: Implications for the source of fluids and trace element character of arc volcanic rocks. *Earth and Planetary Science Letters*, *475*, pp.169-180.

Zajacz, Z., Halter, W.E., Pettke, T. and Guillong, M., 2008. Determination of fluid/melt partition coefficients by LA-ICPMS analysis of co-existing fluid and silicate melt inclusions: controls on element partitioning. *Geochimica et Cosmochimica Acta*, *72*(8), pp.2169-2197.

Zhang, C., Holtz, F., Koepke, J., Wolff, P.E., Ma, C. and Bédard, J.H., 2013. Constraints from experimental melting of amphibolite on the depth of formation of garnet-rich restites, and implications for models of Early Archean crustal growth. *Precambrian Research*, *231*, pp.206-217.

Zhu, B., Fang, B. and Li, X., 2010. Dehydration reactions and kinetic parameters of gibbsite. *Ceramics International*, *36*(8), pp.2493-2498.

Appendix

Figure A-1

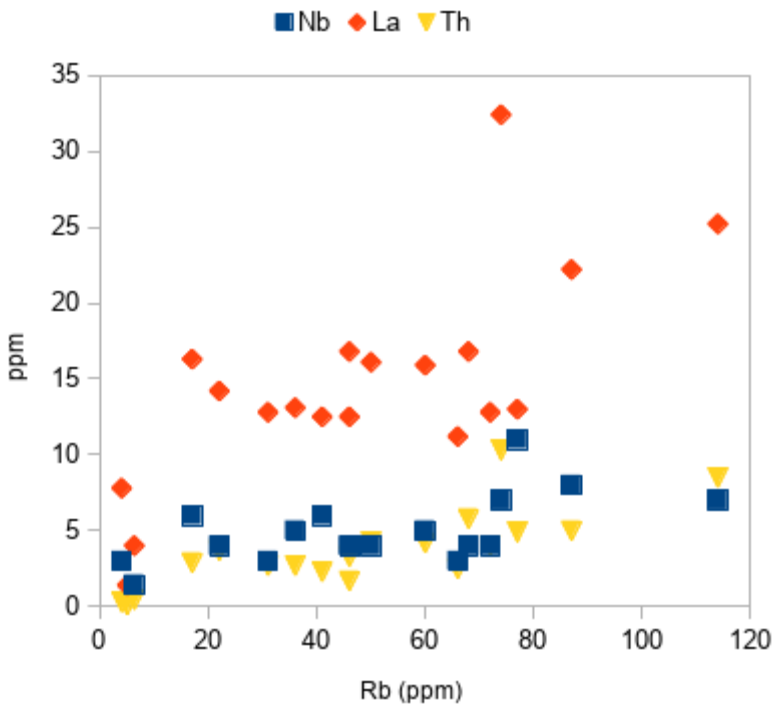

Figure A-1: Correlation of Rb with other incompatible but immobile trace elements indicates that Rb was not added or lost from the whole rock by formation of secondary minerals or other alteration.

Figure A-2

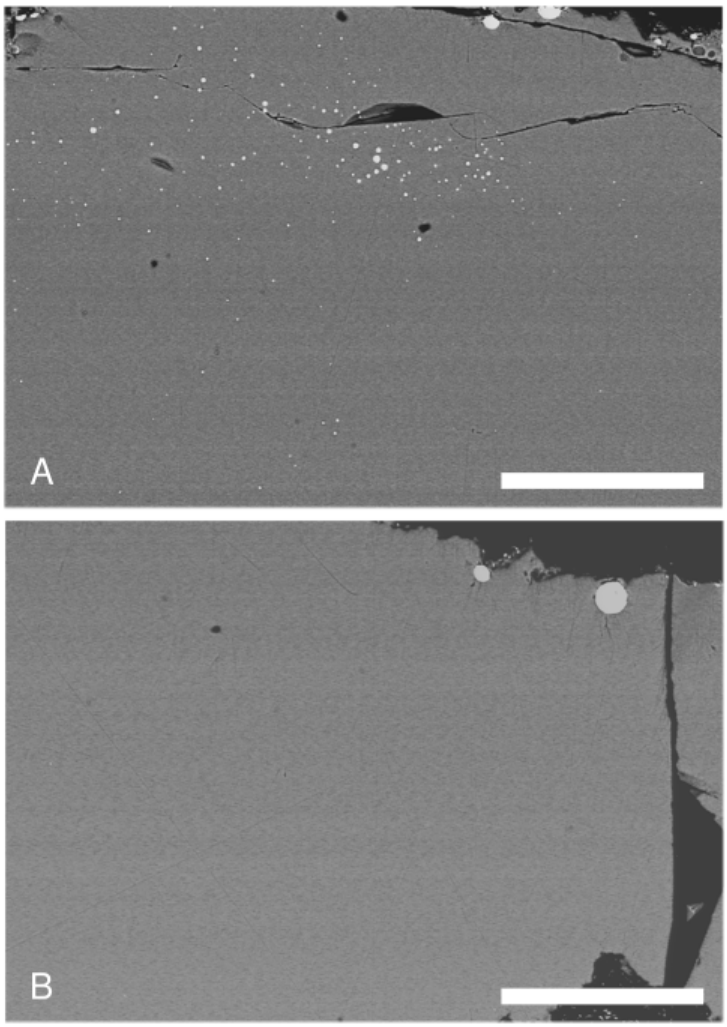

Figure A-2: Back-scattered electron images of glasses from a) P470, low alkalinity, and b) P474, high alkalinity, showing the different sizes and generally circular shapeof sulfide droplets typical of the run products from this study. The white scale bar in both images represents 100 µm.

Figure A-3

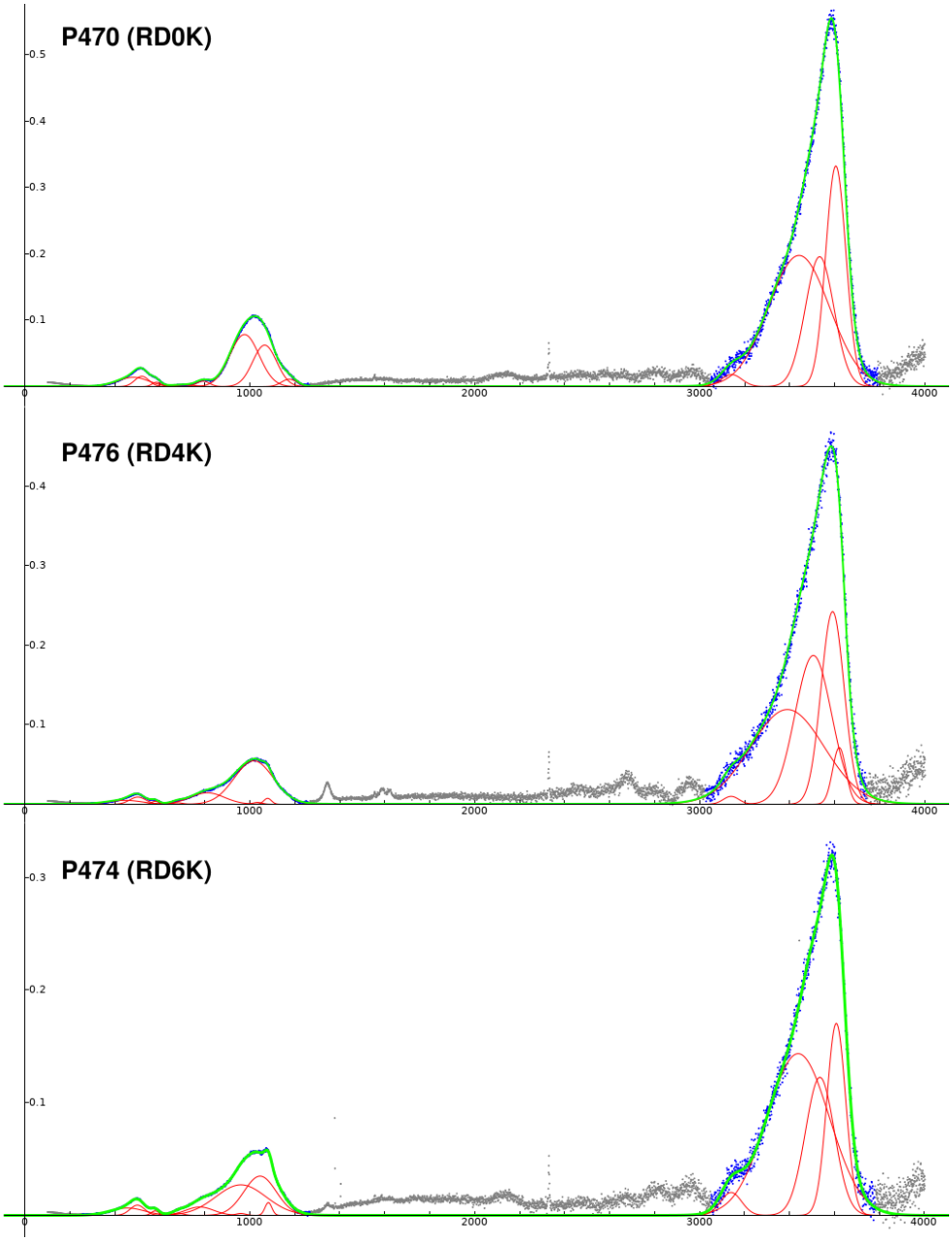

Figure A-3: Representative examples of the Raman spectra that I obtained to quantify H_2O using the method described in the text. The spectra are corrected and baseline subtracted as described in the text. Although some structure is visible in the low wavenumber regions corresponding to the silicate structure, I am unable to determine from this data the relative intensities of peaks known to be related to S bonds (i.e. sulfate at 990 cm^{-1}, sulfide at 372 and 2574 cm^{-1}; Klimm *et al.*, 2012). An increase in intesity of a peak at ~1080 cm^{-1} with increasing alkalinity is visible, though the cause is uncertain.

Table A-1

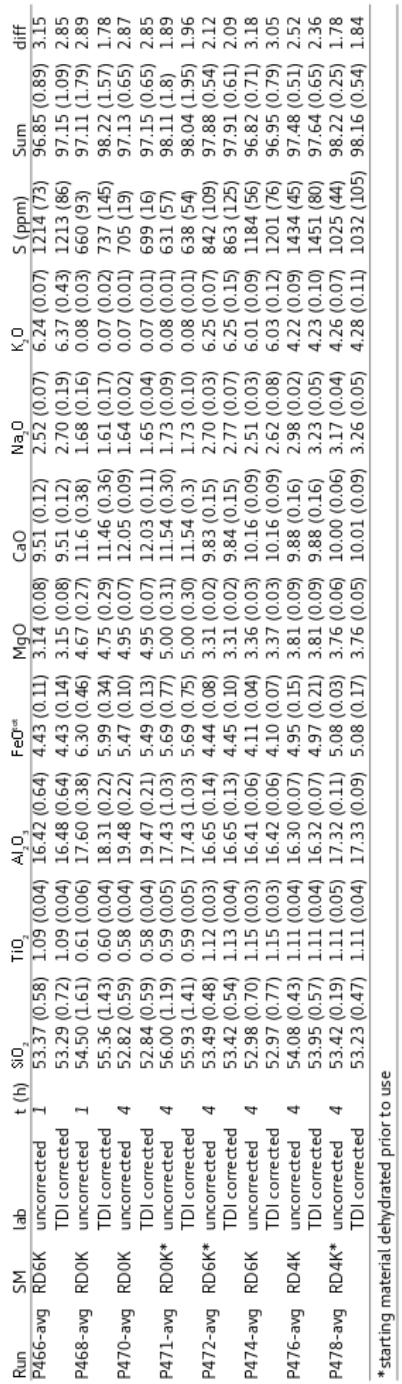

Run	SM	lab	t (h)	SiO_2	TiO_2	Al_2O_3	FeO^{tot}	MgO	CaO	Na_2O	K_2O	S (ppm)	Sum	diff
P466-avg	RD6K	uncorrected	1	53.37 (0.58)	1.09 (0.04)	16.42 (0.64)	4.43 (0.11)	3.14 (0.08)	9.51 (0.12)	2.52 (0.07)	6.24 (0.07)	1214 (73)	96.85 (0.89)	3.15
		TDI corrected		53.29 (0.72)	1.09 (0.04)	16.48 (0.64)	4.43 (0.14)	3.15 (0.08)	9.51 (0.12)	2.70 (0.19)	6.37 (0.43)	1213 (86)	97.15 (1.09)	2.85
P468-avg	RD0K	uncorrected	1	54.50 (1.61)	0.61 (0.06)	17.60 (0.38)	6.30 (0.46)	4.67 (0.27)	11.6 (0.38)	1.68 (0.16)	0.08 (0.03)	660 (93)	97.11 (1.79)	2.89
		TDI corrected		55.36 (1.43)	0.60 (0.04)	18.31 (0.22)	5.99 (0.34)	4.75 (0.29)	11.46 (0.36)	1.61 (0.17)	0.07 (0.02)	737 (145)	98.22 (1.57)	1.78
P470-avg	RD0K	uncorrected	4	52.82 (0.59)	0.58 (0.04)	19.48 (0.22)	5.47 (0.10)	4.95 (0.07)	12.05 (0.09)	1.64 (0.02)	0.07 (0.01)	705 (19)	97.13 (0.65)	2.87
		TDI corrected		52.84 (0.59)	0.58 (0.04)	19.47 (0.21)	5.49 (0.13)	4.95 (0.07)	12.03 (0.11)	1.65 (0.04)	0.07 (0.01)	699 (16)	97.15 (0.65)	2.85
P471-avg	RD0K*	uncorrected	4	56.00 (1.19)	0.59 (0.05)	17.43 (1.03)	5.69 (0.77)	5.00 (0.31)	11.54 (0.30)	1.73 (0.09)	0.08 (0.01)	631 (57)	98.11 (1.8)	1.89
		TDI corrected		55.93 (1.41)	0.59 (0.05)	17.43 (1.03)	5.69 (0.75)	5.00 (0.30)	11.54 (0.3)	1.73 (0.10)	0.08 (0.01)	638 (54)	98.04 (1.95)	1.96
P472-avg	RD6K*	uncorrected	4	53.49 (0.48)	1.12 (0.03)	16.65 (0.14)	4.44 (0.08)	3.31 (0.02)	9.83 (0.15)	2.70 (0.03)	6.25 (0.07)	842 (109)	97.88 (0.54)	2.12
		TDI corrected		53.42 (0.54)	1.13 (0.04)	16.65 (0.13)	4.45 (0.10)	3.31 (0.02)	9.84 (0.15)	2.77 (0.07)	6.25 (0.15)	863 (125)	97.91 (0.61)	2.09
P474-avg	RD6K	uncorrected	4	52.98 (0.70)	1.15 (0.03)	16.41 (0.06)	4.11 (0.04)	3.36 (0.03)	10.16 (0.09)	2.51 (0.03)	6.01 (0.09)	1184 (56)	96.82 (0.71)	3.18
		TDI corrected		52.97 (0.77)	1.15 (0.03)	16.42 (0.06)	4.10 (0.07)	3.37 (0.03)	10.16 (0.09)	2.62 (0.08)	6.03 (0.12)	1201 (76)	96.95 (0.79)	3.05
P476-avg	RD4K	uncorrected	4	54.08 (0.43)	1.11 (0.04)	16.30 (0.07)	4.95 (0.15)	3.81 (0.09)	9.88 (0.16)	2.98 (0.02)	4.22 (0.09)	1434 (45)	97.48 (0.51)	2.52
		TDI corrected		53.95 (0.57)	1.11 (0.04)	16.32 (0.07)	4.97 (0.21)	3.81 (0.09)	9.88 (0.16)	3.23 (0.05)	4.23 (0.10)	1451 (80)	97.64 (0.65)	2.36
P478-avg	RD4K*	uncorrected	4	53.42 (0.19)	1.11 (0.05)	17.32 (0.11)	5.08 (0.03)	3.76 (0.06)	10.00 (0.06)	3.17 (0.04)	4.26 (0.07)	1025 (44)	98.22 (0.25)	1.78
		TDI corrected		53.23 (0.47)	1.11 (0.04)	17.33 (0.09)	5.08 (0.17)	3.76 (0.05)	10.01 (0.09)	3.26 (0.05)	4.28 (0.11)	1032 (105)	98.16 (0.54)	1.84

*starting material dehydrated prior to use

Table A-1: Corrected and time dependent intensity-corrected EPMA results from the UA instrument

Table A-2

run	line	spot	distance from wire edge (µm)	Fe (wt.%)
P480	1	1	93	0.02
P480	1	2	80	0.52
P480	1	3	55	1.29
P480	1	4	45	2.92
P480	1	5	33	5.09
P480	1	6	15	6.69
P480	2	1	90	0.00
P480	2	2	70	0.05
P480	2	3	50	0.61
P480	2	4	28	3.22
P480	2	5	8	8.25
P480	2	6	3	9.59
P480	3	1	85	0.05
P480	3	2	65	0.30
P480	3	3	38	2.18
P480	3	4	30	3.33
P480	3	5	18	6.15
P480	3	6	5	8.12
P479	1	1	93	0.16
P479	1	2	63	0.30
P479	1	3	53	1.14
P479	1	4	30	3.68
P479	1	5	18	5.72
P479	1	6	10	6.99
P479	2	1	103	0.14
P479	2	2	75	0.35
P479	2	3	43	2.16
P479	2	4	23	4.48
P479	2	5	13	6.70
P479	2	6	5	8.72
P479	3	1	75	0.17
P479	3	2	60	0.78
P479	3	3	43	2.26
P479	3	4	28	4.47
P479	3	5	5	6.27

Table A-2: EPMA results for Pt and Fe in Pt wires in P479 and P480

Table A-3

i	$\Lambda_{th,\,i}$	source
SiO_2	0.48	Mills (1993)
TiO_2	0.61	Mills (1993)
Al_2O_3	0.60	Mills (1993)
Fe_2O_3	0.75	Mills (1993)
FeO	1.0	Mills (1993)
MnO	1.0	Mills (1993)
MgO	0.78	Mills (1993)
CaO	1.0	Mills (1993)
K_2O	1.4	Mills (1993)
Na_2O	1.15	Mills (1993)
P_2O_5	0.40	Mills (1993)
H_2O	0.40	Duffy (1996)

Table A-3: Coefficients used in calculating optical basicity in equation [3.7]